UNIVERSITÀ DEGLI STUDI DI PADOVA

Sede Amministrativa: Università degli Studi di Padova
Dipartimento di Ingegneria dell'Informazione

SCUOLA DI DOTTORATO DI RICERCA IN INGEGNERIA DELL'INFORMAZIONE

INDIRIZZO: INGEGNERIA ELETTRONICA E DELLE TELECOMUNICAZIONI

CICLO XXI

Development of Reliable RF-MEMS Switches for Antennas and Space Applications

Coordinatore: Prof. Matteo Bertocco
Supervisore: Prof. Gaudenzio Meneghesso

Dottorando: Vanni Peretti

15 Ottobre 2008

UNIVERSITÀ DEGLI STUDI DI PADOVA

DIPARTIMENTO DI INGEGNERIA DELL'INFORMAZIONE

Development of Reliable RF-MEMS Switches for Antennas and Space Applications

Ph.D. THESIS

Author: Vanni Peretti
Coordinator: Prof. Matteo Bertocco
Supervisor: Prof. Gaudenzio Meneghesso

15 October 2008

DEPARTMENT OF INFORMATION ENGINEERING
UNIVERSITY OF PADOVA

SCUOLA DI DOTTORATO DI RICERCA IN INGEGNERIA DELL'INFORMAZIONE – XXI CICLO
Indirizzo: Ingegneria Elettronica e delle Telecomunicazioni

Abstract

Radio Frequency Micro Electro Mechanical (RF-MEMS) components are a contender for future low-power high-frequency wired reconfigurable networks and wireless communication systems. In many RF applications, a single MEM component can replace and outperform an entire solid-state circuit; in other applications, a judicious association of MEMS with active devices will result in smart communicating circuits and systems. These MEM devices have the potential to surpass the limits of today's equivalent implementations that use only traditional solid-state technology. However, the scarce maturity of this technology makes these devices suffering of severe reliability issues. The purpose of this thesis is to investigate the reliability of RF-MEMS switches, starting from common measurements tests, like cycling and DC characterization, to more particular stresses, like Electro Static Discharge (ESD) or Radiations for space applications qualification.

Sommario

Gli switch Micro-Elettro Meccanici per Radio Frequenza (RF-MEMS) sono tra i dispositivi più promettenti per le future generazioni di network riconfigurabili ad alta frequenza e basso consumo di potenza. Vi sono applicazioni RF in cui un singolo dispositivo MEMS può sostituire e migliorare in termini di prestazioni un intero circuito a stato solido; in altri campi invece, un opportuno connubio fra tecnologia MEMS e dispositivi attivi può portare alla nascita di sistemi di comunicazioni estremamente brillanti e performanti. Infatti, i dispositivi MEMS hanno in loro le potenzialità per sorpassare i limiti delle attuali tecnologie impiegate basate su circuiti integrati. Tuttavia, la mancanza di maturità di una tecnologia così innovativa porta con sé inevitabili problemi affidabilistici. L'obbiettivo di questa tesi è di analizzare l'aspetto affidabilistico degli switch RF MEMS, cominciando da metodi comuni di caratterizzazione e stress, come la caratterizzazione DC e il Cycling stress, fino a test più specifici, come la robustezza a scariche elettrostatiche (ESD) o il monitoraggio di danni indotti da radiazione per la qualificazione dei dispositivi per missioni spaziali.

V: *"**V**oilà! In **V**iew, a humble **V**audevillian **V**eteran,*
*cast **V**icariously as both **V**ictim and **V**illian by the **V**icissitudes of Fate.*

*This **V**isage, no mere **V**eneer of **V**anity, is a **V**estige of the **V**ox populi, now **V**acant, **V**anished.*

*However, this **V**alorous **V**isitation of a by-gone **V**exation, stands **V**ivified*
*and has **V**owed to **V**anquish these **V**enal and **V**irulent **V**ermin **V**anguarding **V**ice*
*and **V**ouchsafing the **V**iolently **V**icious and **V**oracious **V**iolation of **V**olition.*

*The only **V**erdict is **V**engeance;*
*a **V**endetta, held as a **V**otive, not in **V**ain, for the **V**alue*
*and **V**eracity of such shall one day **V**indicate the **V**igilant and the **V**irtuous.*

***V**erily, this **V**ichyssoise of **V**erbiage **V**eers most **V**erbose,*
*so let me simply add that it is my **V**ery good honor to meet you*
*and you may call me **V**."*

Evey: *"Are you like a crazy person?"*

V: *"I'm quite sure they will say so."*

Contents

Introduction

Radio frequency (RF) micro-electromechanical system (MEMS) switches are a contender for future low-power high-frequency wired reconfigurable networks and wireless communication systems [1]. In many RF applications, a single MEM component can replace and outperform an entire solid-state circuit; in other applications, a judicious association of MEMS with active devices will result in smart communicating circuits and systems. These MEM devices have the potential to surpass the limits of today's equivalent implementations that use only traditional solid-state technology. In fact, all RF-MEMS devices (not only RF switches) maintain good miniaturization and they can be integrated with solid state circuits (e.g. either placed on the semiconductor wafer back-end-of-line inter-level dielectrics, or wiring levels, or independently, in the semiconductor component package). RF-MEM devices exhibit almost zero power consumption, extremely good RF linearity, and high quality factor (Q) for tuning. Linearity metrics of input intercept second and third order harmonics (IIP2 and IIP3) both can achieve better than $70\ \mathrm{dBm}$. Concerning RF-MEMS switches peculiarities, they achieve very low insertion loss, of lower than $0.1\ \mathrm{dB}$ (up to $100\ \mathrm{GHz}$) while maintaining high isolation $\geq 20\ \mathrm{dB}$). From the technology standpoint, they are a low-cost fabrication process compared to other RF and microwave solid-state integrated circuits (e.g. RF Silicon on insulator (SOI), Gallium Arsenide (GaAs)). In particular, RF-MEMS can be made using standard foundry silicon processes, making them a very promising candidate; Si RF-MEMS are very easy to micro-machine, can be integrated with mature semiconductor technology processes, and has the potential for wide proliferation across the global semiconductor foundry business. Additionally, Si RF-MEM technology is compatible with the integrated circuits for digital, analog and RF mixed signal environments, making it possible to realize high frequency RF modules featuring a high level of integration (e.g. network-on-chip (NOC), and system-on-chip (SOC)). Another very attractive advantage for integration with Si-based technologies relates to its mechanical properties that make it possible to realize mobile regions through electrostatic, magnetic or thermal excitation that will result in devices featuring tunable behavior [2].

Despite these positive aspects, all the above and further benefits go along with a series of present-day shortcomings; these shortcomings are mostly related to the maturity of today's still-evolving design methodologies and semiconductor fabrication processes. The integration dilemma and potential MEM paradigm shift that these new technologies have introduced is also accompanied by a lack of fabrication process standardization, big design flow impact, a limited reliability database, and poor knowledge of aging mechanisms and reliable design practices. In terms of future applicability of these RF-MEMS to high-volume low-cost wired and wireless telecommunications markets, there are a lot of new applications that can realized.

Today, conventional solutions are currently reaching plateau levels of cost reductions through batch processing that could hardly be tackled by emerging technologies. The RF-MEMS technology does not only need to prove as performing and reliable as its established competitors, but it must provide for completely new functionalities and unexplored circuits and systems solutions, to gradually find its way into the commercial RF microwave market. In order for these implementation possibilities to be achieved, the RF-MEMS must overcome these reliability hurdles.

The purpose of this thesis is to investigate the reliability of RF-MEMS switches, starting from common measurements tests, like cycling and DC characterization, to more specific stresses, like Electro Static Discharge (ESD) or Radiations ones. This work does not want to provide a universal methodology to certificate any kind of RF-MEMS device, since the lack of process standardization brings to the market every time new devices with new materials and different reliability issues. Nevertheless, if only the technologies based on Metal-Insulator-Metal (MIM) structure are considered, an almost complete reliability perspective with the main literature topics is presented.

The first chapter describes the different topologies of the tested devices, with a general presentation of the RF-performances and the main switch parameters (actuation voltage, release voltage, insertion losses and isolation).

The second chapter is an overview of the main reliability issues that affect RF-MEMS devices with a particular attention to the less investigated tests (ESD and Radiation) in literature.

The third chapter will be dedicated to the cycling stress test, one of the most common parameter to classify the device robustness.

In the fourth chapter, the behavior of an RF-MEMS device submitted to continuous biasing will be presented, focusing on the release time issues that such stress generates and the release transient in general (bouncing).

The fifth chapter presents the ESD effects on an RF-MEMS switch. The results on RF-MEMS switches submitted to Electro-static discharge in different configurations will be shown and a first study of HBM (Human Body Model) effects on such devices will be discussed.

In the last chapter, after an introduction to the radiation damage mechanisms, the results obtained after the protons and x-rays radiation stress on RF-MEMS devices will be presented.

Chapter 1

Devices and process description

The RF-MEMS switches tested and analyzed in this work have been manufactured by the Bruno Kesler Foundation (FBK) of Trento (Italy). The ohmic switches, both series and shunt, based on meander and straight beams (see par. 1.3), have been produced in the contest of a Project of Relevant National Interest (PRIN) in collaboration with other italian Universities. [1] The other kinds of devices tested, belong to an international project in collaboration with the European Space Agency (ESA)[2]with the target to develop a reliable redundancy switch for space application.

1.1 A mechanical description of anchored beams and cantilever

To physically implement the RF-MEMS switch, a double anchored beams and a cantilever beam solution, based on electrostatic actuation, has been adopted. The principle that rules these devices is quite simple: a voltage is applied between the MEMS suspended membrane and the actuation structure that typically lays beneath the bridge. The electrostatic force generated will bend down the membrane until a physical ohmic contact will be achieved with the transmission line contacts. The actuation structure (in Poly-silicon) is normally coated with Silicon Dioxide to prevent a short circuit with the membrane when it is in the actuated state. The next sections will be dedicated to a summary on the electrostatic actuation principles and to the spring constant k determination and modeling for a generic MEMS switch based on anchored beam or cantilever. A complete description of RF-MEMS mechanical model is given in [3].

Electrostatic actuation

When a voltage is applied between the actuation pad and the suspended membrane, an electrostatic force is induced between the two structures. In first approximation, this force can be compared to the one induced between the plates of a charged capacitor (see figure 1.1). In fact,

[1]Partners are: University of Padova (Italy), FBK (Italy), University of Bologna (Italy), University of Udine (Italy) and Politecnico di Torino (Italy)

[2]Partners are: University of Padova (Italy), FBK (Italy), University of Perugia (Italy), Technische Universität München (TUM)(Germany), Alcatel Alenia Space (Italy) and the National Research Center (CNR) (Italy)

the suspended membrane could be considered as the upper plate of a moving capacitor while the actuation structure would be the fixed one: in this way, an easier model can be used to understand the principle that rules the MEMS mechanical behavior. It is important to underline that the equivalent capacitance of the variable capacitor should be calculated taking into account that the MEMS bridge is a mechanical continuum with a finite length and therefore an appropriate averaging method should be used to compare a 3D structure to a single degree of freedom system. However, due to the almost infinite design possibilities of an RF-MEMS switch, it is no possible to find a optimum averaging method for the capacitance value which is efficient for all the different designs. In fact, the capacitance value depends on the membrane dimensions and shape, and the capacitance variation is correlated to the dynamic response of the used materials.

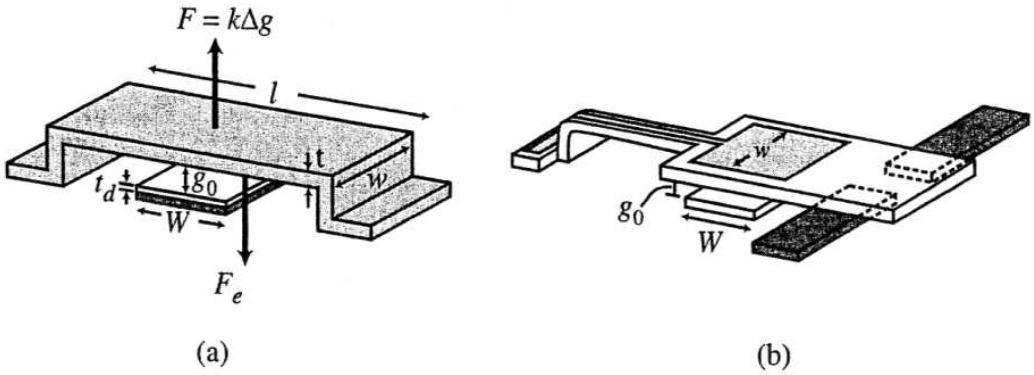

Fig. 1.1: Examples of a anchored beams based MEMS switch (a) and of a cantilever one (b).

If we define w the beam width and W the pull down electrode width, the equivalent capacitance will be

$$C = \frac{\epsilon_0 w W}{g} = \frac{\epsilon_0 A}{g}$$

where A is the area of the capacitor defined by the cantilever and pull down electrode width, and g is the height of the suspended beam. The attractive electrostatic force generated by the applied voltage will be

$$F_e = \frac{1}{2} V^2 \frac{dC(g)}{dg} = \frac{1}{2} \frac{\epsilon_0 W w V^2}{g^2}$$

where $V$is the voltage applied. It is important to underline that the electrostatic force does not depend on the voltage polarity. If we compare the generated force with the spring restoring force ($F = kx$), we obtain

$$\frac{1}{2} \frac{\epsilon_0 W w V^2}{g^2} = k(g - g_0)$$

where g_0 is the bridge height in the rest position. From this we have

$$V = \sqrt{\frac{2k}{\epsilon_0 w W} g^2 (g_0 - g)}.$$

The graph in figure 1.2 shows the beam position versus the applied voltage. As it is possible to

see there are two solutions of the beam height for every applied voltage.

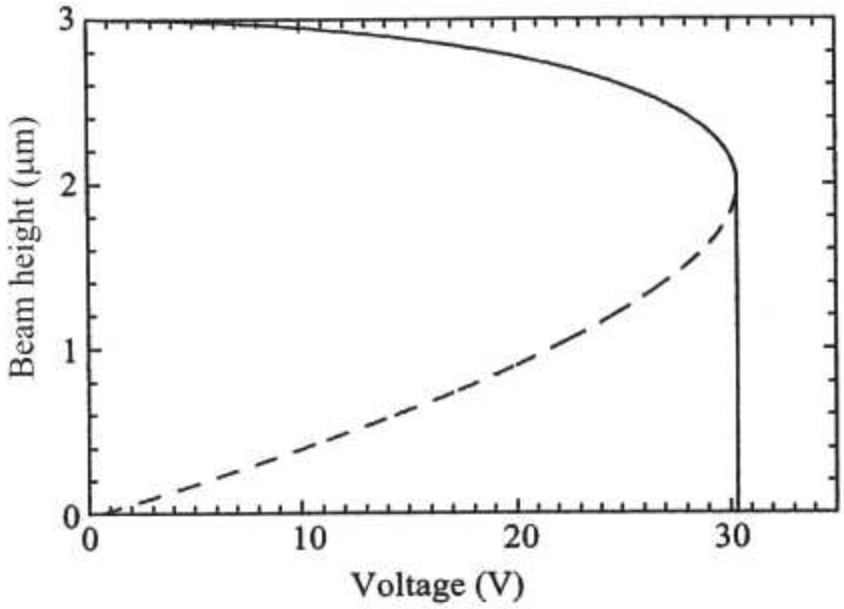

Fig. 1.2: Beam height vs applied voltage: the structure shows an instability at $(2/3)g_0$ *that lead the MEMS bridge to collapse on the bottom electrode for higher voltages.*

This is due to the fact that the beam becomes instable at (2/3)g_0 since the feedback generated by the electrostatic force is positive. This instability can be better understood if the electrical field applied to the beam is considered. In fact we have that

$$F_e = \frac{QE}{2}$$

where Q is the electrical charge on the beam and $E = V/g$ is the electrical field. When we increase the applied voltage, the electrostatic force is increased too for the accumulating charge on the MEMS beam. At the same time the structure capacitance increases for the approaching of the beam to the pull down electrode caused by the attracting force. When the $2/3g_0$ height is reached, the increasing of the electrostatic force overcome the increasing of the spring restoring force leading the beam to collapse on the bottom electrode. From this we can calculate the voltage value needed to bring the beam to the collapse point:

$$V_{Act} = V\left(\frac{2}{3}g_0\right) = \sqrt{\frac{8k}{27\epsilon_0 W w}g_0^3}$$

where V_{Act} is the nominal device actuation voltage. A more detailed analysis is presented in [3].

The spring constant k

As has been demonstrated in the previous section, the actuation voltage is strictly dependent on the spring constant k. There are different parameters that allows to change the spring constant

value, from the material used to build the beam to the shape of the beam itself or of the beam anchors. For an assigned beam material, the stronger spring constant is typically obtained with a double straight anchored beam. On the contrary, if the purpose of the project is to obtain a weaker spring constant, different solutions based on bended anchors can be adopted, depending on the application. In figure 1.3 multiple examples of beam anchors are reported from the more stiff configuration (a) to the weaker one (d). The (b) and (c) solutions are a little variation of the configuration (a) (straight beams) with the aim to just lower a little bit the straight beam spring constant (b) or to improve the beam truss stiffness (c). A complete analysis of the spring constant modeling and derivation is reported in [3].

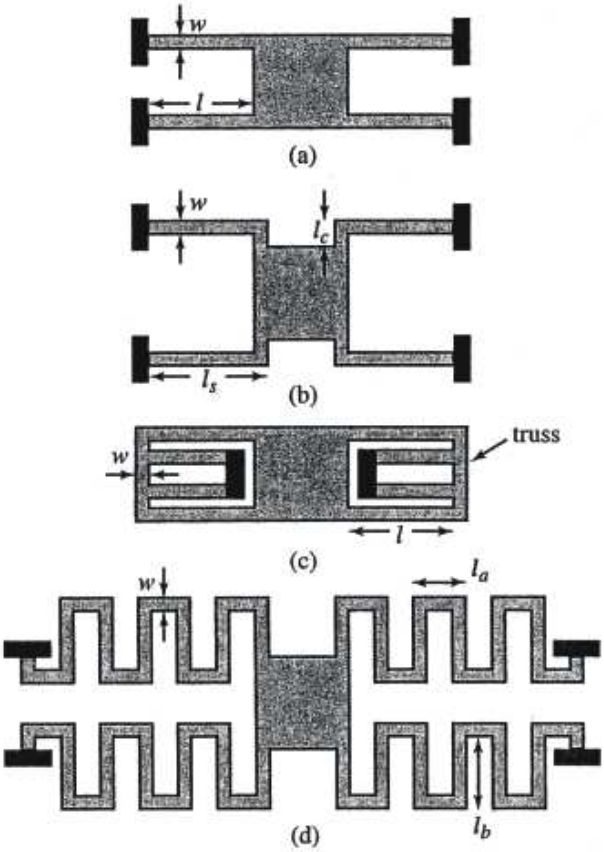

Fig. 1.3: Examples of anchored beams topology: straight beams (a), softer straight beams (b), very stiff truss beams (c) and meander beams based (d).

1.2 FBK process description

FBK developed a process that is optimized for the fabrication of RF-MEMS switches on a high resistivity silicon substrate. A cross section of the process is shown in figure 1.4. The process makes use of a photoresist as a sacrificial layer for the creation of the suspended structures. These are defined using electroplating. A thick field oxide is first deposited on the wafer to isolate the devices and minimize the electric loss toward the substrate. A polysilicon layer allows the creation of integrated resistors and the switch actuation electrodes. A multimetal

layer, which is a sandwich of titanium, titanium nitride, aluminum and titanium nitride, can be used as a contact to the polysilicon or as an underpass. Moreover, it can be used to form an integrated capacitor with the subsequent isolation and gold metal layer. Gold suspended structures can be created with three different thicknesses, resulting from the combination of two electroplating steps. The maximum electroplated gold thickness, which is $5\ \mu\mathrm{m}$, is used also for the definition of the coplanar waveguides. An additional layer of sputtered gold can be used to create floating electrodes. For capacitive switches, a gold layer deposited on top of the dielectric enhances the contact with the armature, when the switch is closed. Moreover, this layer is also required for the realization of gold-gold ohmic contact in metal contact switches. The FBK switch process makes use of 8 masks and a total of 22 main process steps, listed in figure 1.4. The process starts with the growth of the field oxide on the wafer. Then, the polysilicon layer is deposited, doped with Boron and covered with a thin TEOS oxide. After the opening of the vias to the polysilicon, the multimetal layer is deposited and patterned on the wafer. The metal is covered with a thin low temperature oxide (LTO), which is removed, where necessary, for the realization of electrical contacts. The gold floating metal is then deposited and patterned. At this point, a $3\ \mu\mathrm{m}$ thick photoresist is spin-coated on the surface, which serves as a sacrificial layer for the creation of the suspended structures. The photoresist is post-baked at high temperature, in order to round the edges of the photoresist structures and to avoid further deformation of the spacer photoresist during subsequent high temperature steps. The seed layer for the electroplating of the suspended structures and other thick metal parts is then evaporated on the substrate. Evaporation does not guarantee a good coverage of steep edges. This renders the removal of sharp edges from the wafer surface necessary to ensure a complete coverage of the seed layer and thus electrical continuity during the electroplating steps. Afterward, gold is electroplated on the wafer in two steps with different thicknesses: a first layer of $2\ \mu\mathrm{m}$, called BRIDGE layer, and a second layer of around $3\ \mu\mathrm{m}$, called CPW layer. Areas on which the gold has to be electroplated are defined with a photoresist masking layer, with a thickness higher than the one of the layer to grow. After the electrodeposition steps, the wafer undergoes a temperature treatment, which serve to improve the adhesion of the gold to the wafer. This is especially important for wire bonding purposes. The suspended structures are then released by dry etching of the spacer with oxygen plasma. The most critical part of the process is the creation of stress-free suspended structures. When thin films are deposited on a sacrificial layer at a temperature lower than its flow temperature, then intrinsic stresses develop in the film-sacrificial layer sack. Both in-plane stress and stress gradients can arise. These not only modify the mechanical properties of the materials, but can cause out of plane bending of the suspended structures after their release. The entity of the effect depends mainly on the temperature treatment, to which the wafer is subjected and on the materials used [4]. In the presented process, the annealing of the wafer after electroplating leads to in-plane tensile stress in the gold layer.

Moreover, the diffusion of the seed layer into the electroplated membrane led in the past to a stress gradient in the thickness of the suspended gold layer. The thicknesses of the layers used in the seed layer were therefore optimized in order to minimize the effects of this phenomenon. A more detailed process description is given in [5].

The FBK process can be summarized in six phases (figure 1.4):

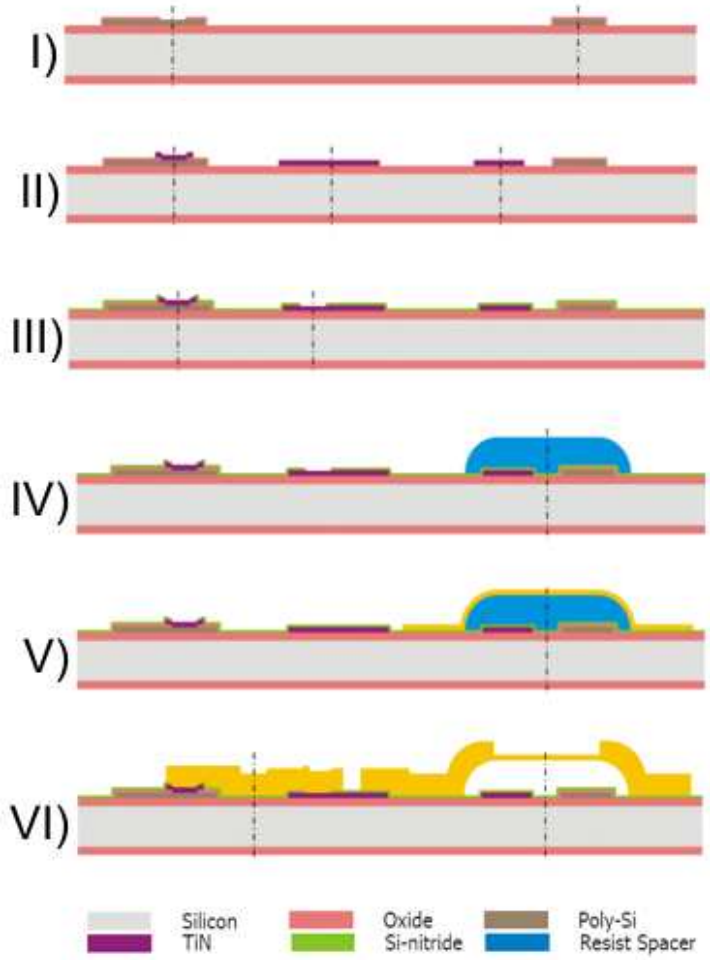

Fig. 1.4: Phases of the physical process (by FBK) to manufacture the RFMEMS devices.

I) growing of $1000\ \mathrm{nm}$ of insulator oxide, deposition of $630\ \mathrm{nm}$ of polysilicon, Boron implantation, definition of polysilicon, Boron diffusion at $925\ ^{\circ}\mathrm{C}$, deposition of $300\ \mathrm{nm}$ of TEOS and opening of the contacts

II) deposition and definition of metal alloy Ti/TiN/Al/Ti/TiN, respectively of $30/50/410/60/80\ \mathrm{nm}$ (underpass)

III) deposition of $100\ \mathrm{nm}$ of LPCVD oxide (or PECVD Nitride) and VIA definition

IV) deposition and definition of the spacer based on $3\ \mu\mathrm{m}$ of resist

V) seed layer of Cr/Au ($10/150\ \mathrm{nm}$ respectively), area definition of the first electro-deposition and first electro-deposition of Au ($1.5\ \mu\mathrm{m}$ for pads and bridges)

VI) second electro-deposition of Au ($3.5\ \mu\mathrm{m}$ for thick bridges and CPW), seedlayer removal.

1.3 The devices designed by University of Bologna

The devices produced in the contest of the PRIN project can be divided in four categories:

- **Ohmic series meander beam based switch** : the device is an open circuit when no actuation voltage is applied and become a transmission line when actuated; the meander beams result in a weaker spring restoring force and in a consequentially lower actuation voltage (typically around $10 - 20$ V) (see figure 1.5a and figure 1.5d)

- **Ohmic shunt meander beam based switch**: the device is a transmission line when no actuation voltage is applied and become a short to ground when actuated; the meander beams result in a weaker spring restoring force and in a consequentially lower actuation voltage (typically around $10 - 20$ V)(see figure 1.5b)

- **Ohmic series straight beam based switch**: the device is an open circuit when no actuation voltage is applied and become a transmission line when actuated; the straight beams result in a strong spring restoring force and in a consequentially high actuation voltage (typically around $40 - 60$ V) (see figure 1.5c)

- **Ohmic shunt straight beam based switch**: the device is a transmission line when no actuation voltage is applied and become a short to ground when actuated; the straight beams result in a strong spring restoring force and in a consequentially high actuation voltage (typically around $40 - 60$ V)

To reduce the oxide charging phenomena (see par. 2.1, page 24), an interdigitated topology is adopted for signal underpass and actuation electrodes [6]. Direct contact is allowed only between the plate and the signal electrodes, by raising the signal underpass metal above the level of the poly electrodes, through the placement of poly dummy rectangular bricks. Therefore, during the actuation, the suspended membrane gets in contact with the signal underpass crating a low resistance path between the input and the output ports (series configuration) or between the input port and the RFground (shunt configuration) blocking the RF signal. In some variation (thick bridge switches) of the four basic devices just presented, a 5 μm thick electroplated gold layer is used for the plate to improve its rigidity, whereas a thinner 1.5 μm gold membrane implements the four suspending beam springs. The electrostatic pull-in voltage is typically around $40 - 60$ V for the straight beams design, reaching below 20 V for the meander-based devices. To guarantee a good release etch step, the suspended structure layout is binded in one dimension to 20 μm. This leads to the perforated plate structure with 20x20 μm holes with 20 μm separation. This characteristic, typical for surface micro machined devices, is a key factor in defining viscous damping phenomena for the dynamic behavior of the device operating in non-vacuum conditions. The RF signal is applied on the left side of the device which can be contacted with microprobe (Ground-Source-Ground probe with 150 μm pitch) and read on the right side (see as example figure 1.5a). Since the device is symmetric from a RF point of view, the input and output port can be switched. The pad in the bottom provides the actuation force through a polysilicon structure that runs from the pad to the suspended bridge.

Contacts with dimples

The devices presented in par. 1.3 typically exhibit a flat surface on the contact blocks under the suspended membrane, as shown in figure 1.6. This wide metal-to-metal contact area

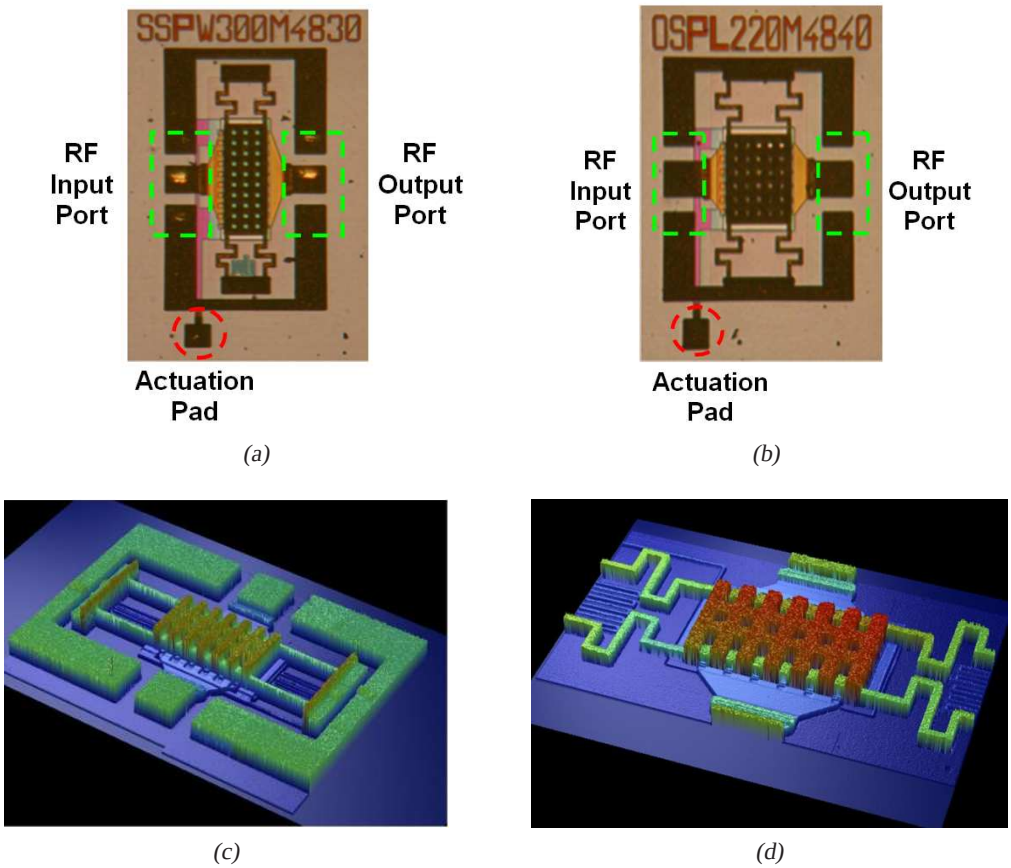

Fig. 1.5: Picture of an ohmic series switch (a) and of an ohmic shunt switch (b) with meander beams. Optical profilometer image of a straight beam series switch (c) and magnification of a meander based switch membrane (d).

should guarantee a lower series resistance between the bridge and the transmission line during the device actuation and, therefore, excellent RF performances. Nevertheless, due to nano irregularities on the gold surface and to hardening or pittening of the contact during multiple actuation [3], it happens that only a small part of this area gets in contact leading to a sensible increase of the series resistance and a degradation of the device RF performance.

A possible way to obviate to this uncontrolled use of the contact surface is to introduce a "dimple" on every single contact. A "dimple" is a small hill over the contact which has the property to locally increase the pressure generated by the suspended membrane during the actuation phase, with a consequentially higher force applied to the metallic contact. In this way, a lower and more repeatable series resistance should be achieved leading to a better RF working device. In figure 1.7a, an optical profilometer image of an ohmic series switch after the membrane removal is presented. Comparing figure 1.7a with figure 1.6 it is immediate to note the presence of dimple over the contacts. A zoom of dimples structure is reported in figure 1.7b.

The main difference between Poly dimples and Conho dimples is the structure height: Poly dimples are about $630\ \mathrm{nm}$ tall, while the Conho structure (which are obtained with the Conho mask that keeps the acid attack from removing the silicon oxide over the Poly-silicon) are

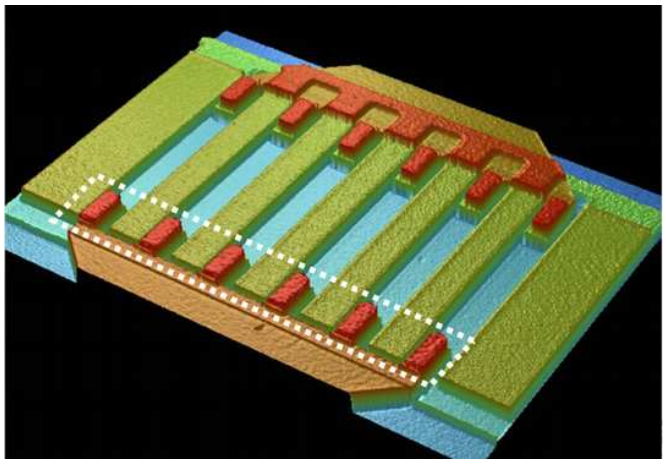

Fig. 1.6: Optical profilometer image of a series ohmic switch after the membrane removal: in the underlined zone it is possible to see the input port flat contacts.

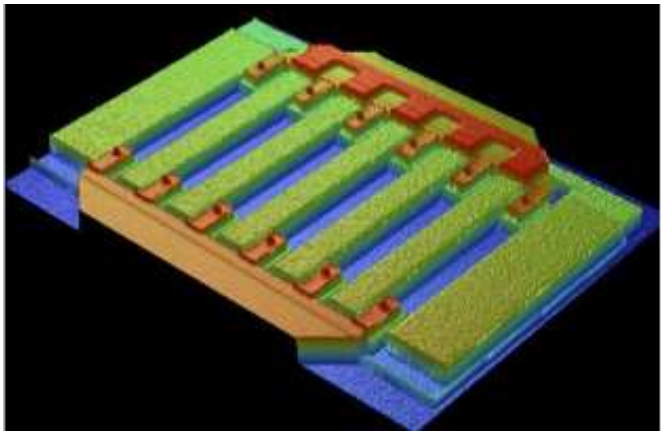

(a)

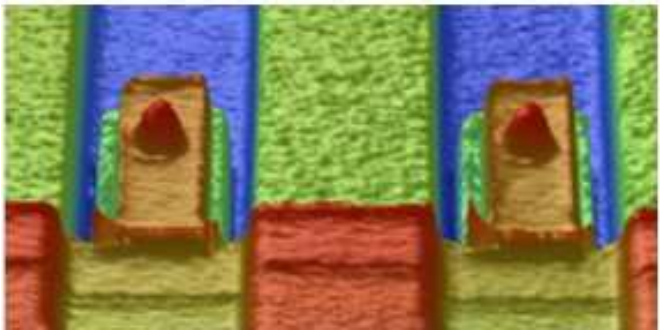

(b)

Fig. 1.7: Optical profilometer image of a series ohmic switch with dimpled contacts after the membrane removal (a) and zoom of the dimpled contacts (b).

400 nm.

1.4 The devices designed by University of Perugia

The devices tested in the contest of the ESA project and presented here, belong to a first prototyping run and not to the last and more advanced technology evolution of the devices. The devices has been designed by the University of Perugia and manufactured by FBK and can be divided in four topologies.

Series ohmic winged switch with stopping pillars (PSX)

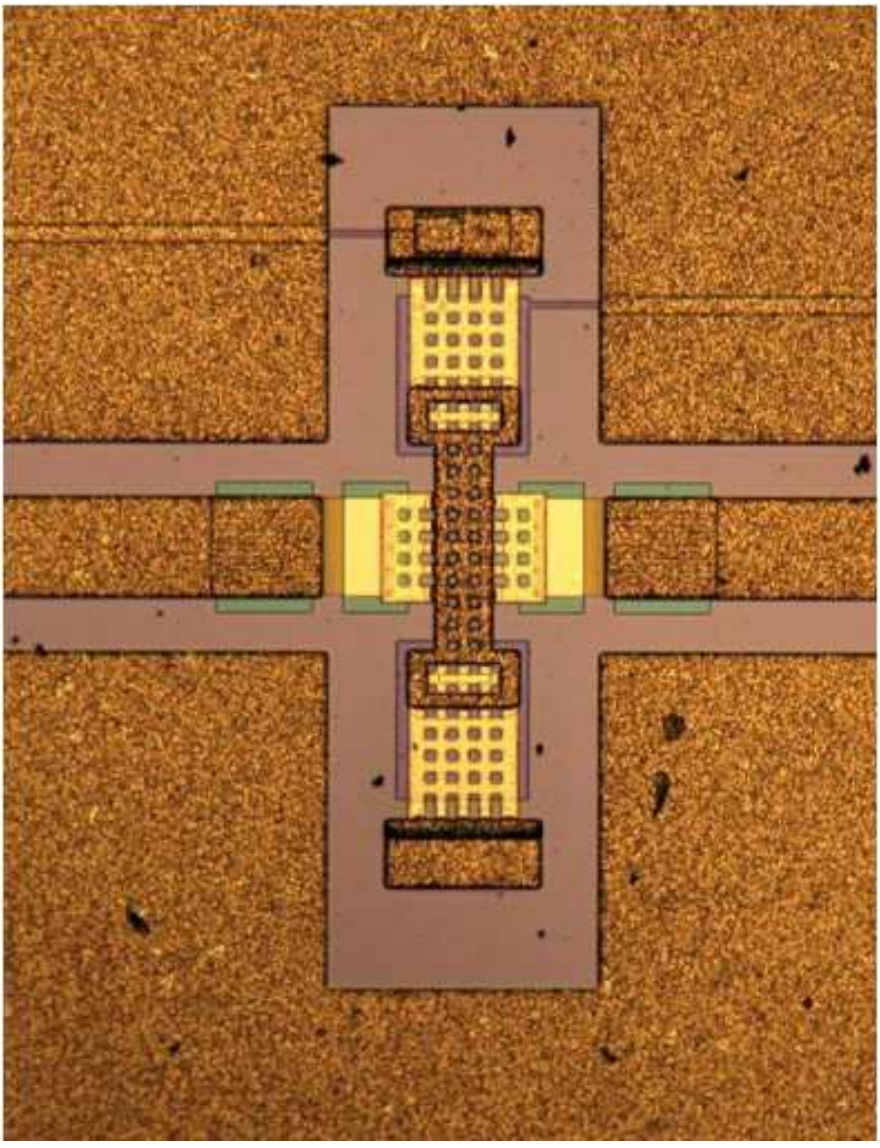

Fig. 1.8: Picture of the series ohmic winged switch stopping pillars (PSX).

The series ohmic winged switch stopping pillars (see figure 1.8) consists of a metallic bridge, isolated from the ground planes of the co-planar waveguide, suspended above an in-

terrupted signal line. In the up state the bridge is suspended above the interrupted signal line providing very high and wideband isolation better than 20 dB from DC up to 30 GHz (see figure 1.9a). On the contrary, in the down state the bridge is lowered by the electrostatic forces applied through the actuation pad in order to contact the two ends of the signal line. The device exhibits very good insertion losses (-0.8 dB at 30 GHz) and excellent return losses on the whole broadband (between -20 dB and -30 dB from DC up to 30 GHz), as shown in figure 1.9b and figure 1.9c respectively. The measured pull-in voltage to actuate the device is about 50 V.

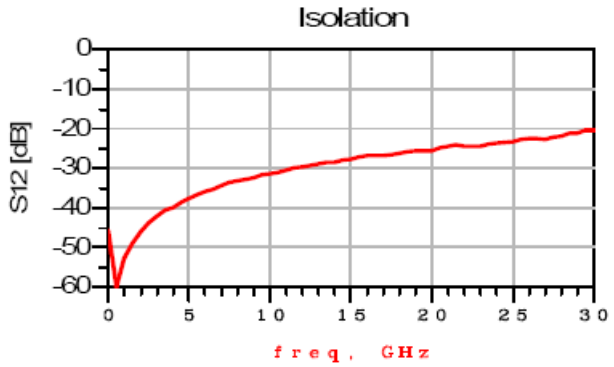

(a)

(b)

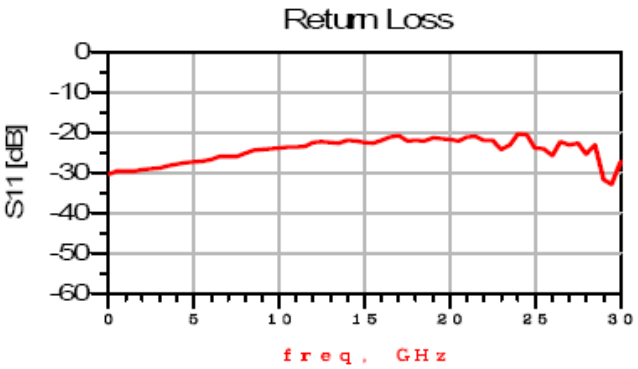

(c)

Fig. 1.9: Isolation vs frequency (a), insertion losses (b) and return losses (c) of a series ohmic winged switch stopping pillars.

Since the dielectric charging phenomenon is one of the most critical issues for an RF-MEMS device reliability, a first solution to overcome this effect is to realize a dielectric-free actuation pads avoiding the contact between the bridge and the pad [7]. This is possible by either realizing mechanical stoppers on the bottom surface of the bridge layer or building stopping pillars on the activation pad. The latter solution has been adopted since it does not require any modification of the FBK MEMS process.

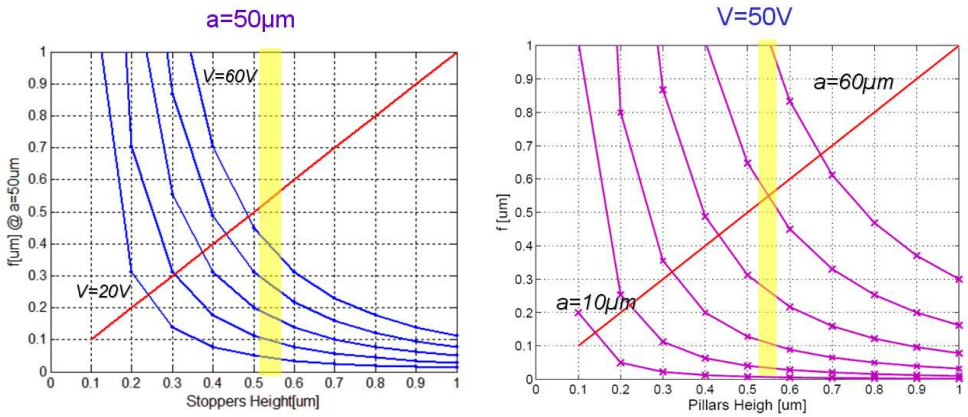

(a) *(b)*

Fig. 1.10: Bridge deformation f as a function of the pillars height. Fixed spacing a= 50 µm and increased voltage V (from 10 V to 60 V, with a 10 V step) (a). Fixed voltage V = 50 V and increased spacing a (from 10 µm to 60 µm, 10 µm step) (b).

Since the actuation structure is not covered with any dielectric, it is extremely important to properly design the mechanical stoppers in order to prevent the bridge from any contact with the bottom electrode. A first estimation of the bridge deformation above the stoppers has been done by assuming the bridge to be like an infinite plate of thickness t supported by dot-like pillars positioned in the vertexes of squares [8]. For such a structure the plate maximum displacement f is given by the following expression:

$$f = 0.063 \left(\frac{p}{E}\right)\left(\frac{a^4}{t^3}\right)$$

Where E is the Young Modulus, t is the plate thickness, a is the length of the square sides, p is the applied load which, in the case of electrostatic actuation, is equal to:

$$p = \frac{F_e}{a^2} = \frac{1}{2}\frac{\epsilon_0 A_{pad}}{a^2 V^2}$$

where F_e is the electrostatic force, ϵ_0 is the vacuum permittivity, V is the voltage applied on the area A_{pad}. Note that such expression provides an overestimation of the bridge deformation since it does not account for the bridge tensile stress and spring constant. In figure 1.10 the bridge deformation as a function of the pillars height with respect to the actuation structure is reported. figure 1.10a presents the bridge deformation when a is set to 40 µm and V is varied from 20 V to 60 V with a step of 10 V. The variation of f as a function of the spacing a for

a fixed applied voltage V of 50 V is shown in figure 1.10b. According to this computation, a 0.55 μm thick and $40 - 50$ μm spaced pillars should ensure the bridge isolation from the bottom electrode.

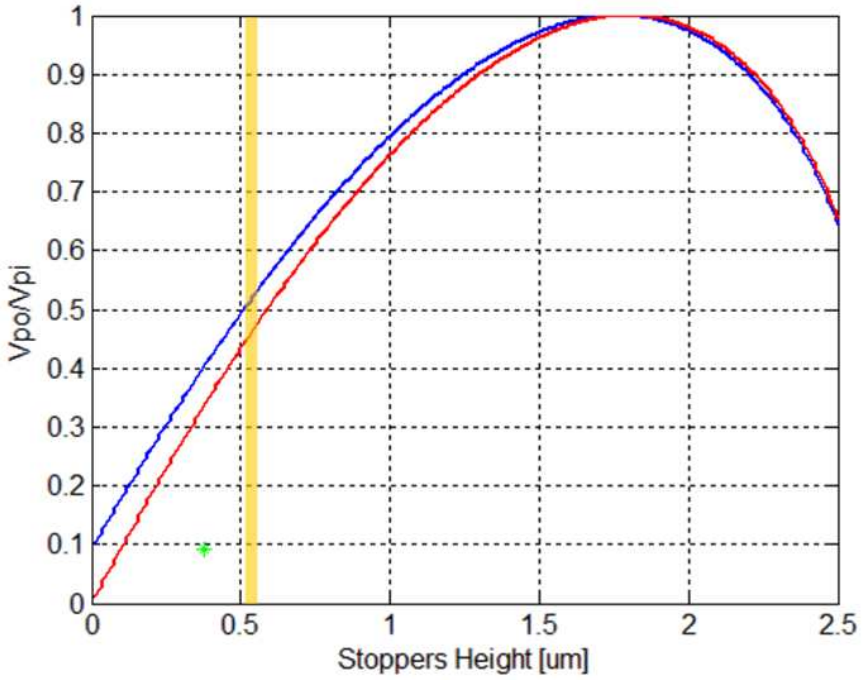

Fig. 1.11: V_{PO}/V_{PI} ratio as a function of the pillars height. The yellow line represent the working points for 0.55 μm stopping pillars.

As well as reducing the dielectric charging phenomena, the stopping pillars lead to an increased pull-out voltage V_{PO} which is in general a desirable effect since indicates an increase of the beam restoring force. The ratio V_{PO} / V_{PI} is given by the following expression which has been derived by the formula for the standard dielectric-covered pads:

$$V_{PO}/V_{PI} = \sqrt{\frac{27}{4}\frac{(d_0 - d_a)\left(d_a + \frac{d_e}{\epsilon_r}\right)^2}{\left(d_0 + \frac{d_e}{\epsilon_r}\right)^3}}$$

where d_0 is the total air gap above the pad, d_a is the pillars height with respect to the pad, d_e is the thickness of the dielectric covering the pad and ϵ_r its dielectric constant. In figure 1.11 is shown the ratio V_{PO}/V_{PI} as a function of the pillars height for the case of dielectric-free electrode (d_e= 0). Note that for a 0.55 μm stoppers the pull-out V_{PO}/V_{PI} ratio is close to 0.5. It is important to consider that in standard dielectric switches the pull-out voltage values are not easily predictable due to the uncertainty in the adhesion forces value between the dielectric covering the pad and the metal bridge. On the contrary in the case of stopping pillars such forces do not act, and a better agreement between the theoretical and the actual value is expected.

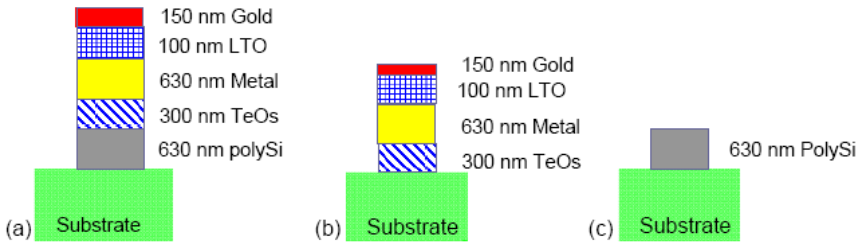

Fig. 1.12: Layers constituting the contact bumps (a), the stoppers (b) and the electrodes (c).

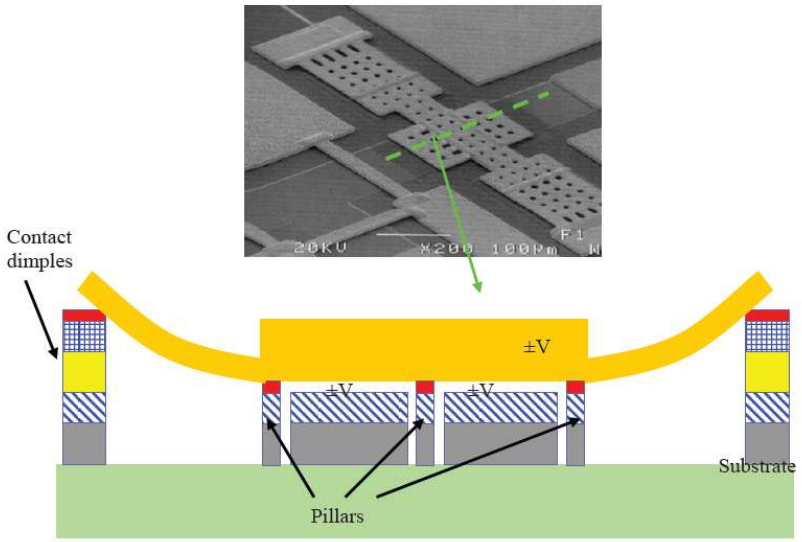

Fig. 1.13: Cross section of the series ohmic switch constituting the switching unit.

New stopping pillars have been designed to be $4\ \mu\mathrm{m}$ x $4\ \mu\mathrm{m}$ large, $1.18\ \mu\mathrm{m}$ thick bumps deposited on the substrate. The pad thickness is $0.63\ \mu\mathrm{m}$ resulting in a stopper elevation of $0.55\ \mu\mathrm{m}$ with respect to the electrode. The thickness of the contact bumps in ohmic switches is $0.63\ \mu\mathrm{m}$ bigger than the stoppers height in order to guarantee low contact resistances. The pillar spacing is about $40 - 50\ \mu\mathrm{m}$. In figure 1.12 is reported the layers that have been patterned for the realization of the contact bumps, the stoppers and the electrodes. As it is possible to see in figure 1.13, the pillars height is larger than the actuation electrode height. In this way when applying the actuation voltage, the suspended membrane will rest on top of the pillars that will prevent it from touching the polarized actuation electrode.

Cantilever switch (CA)

The ohmic contact single pole single throw (SPST) switch consists of a gold membrane suspended above an interrupted micro-strip signal line and anchored at one end.

A photograph of the fabricated cantilever switch is shown in figure 1.14. In order to guarantee a repeatable and low contact resistance seven dimples have been placed in the contact area of the micro-strip line, and the beam central part has been reinforced with thicker gold, thus leading to a lower total contact resistance [9]. The performance of the single MEMS switch

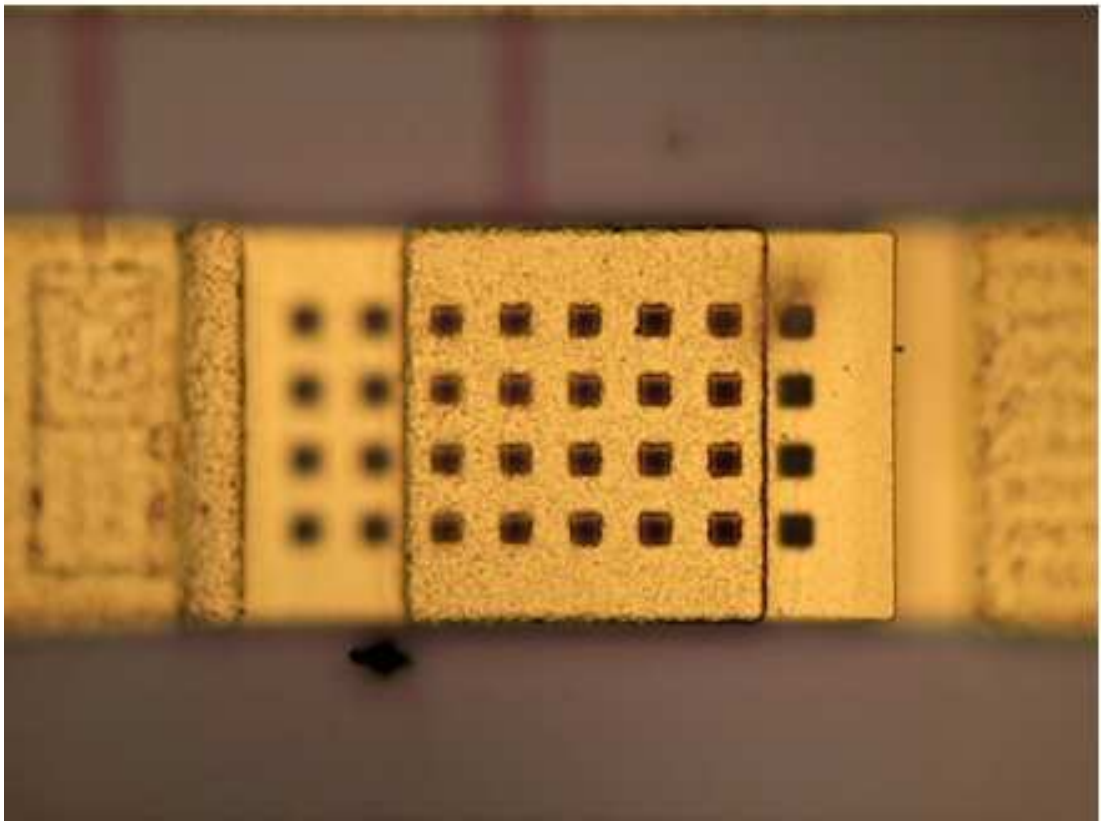

Fig. 1.14: Photo of the series ohmic cantilever MEMS switch.

has been presented in [5, 10]; it shows a contact resistance lower than $1\ \Omega$, an insertion loss better than 0.1 dB and an isolation better than 12 dB up to 15 GHz (see figure 1.15). Actuation voltage of about 50 V and un-actuation voltages (which is the voltage value where the restoring force becomes higher than the electrostatic force bringing the switch in the up-state position) of about 40 V have been recorded.

The cantilever switch can be implemented with stopping pillars and without dielectric as the series ohmic winged switch with stopping pillars (PSX).

Boosted ohmic shunt switch (BO)

The boosted ohmic shunt switch (see figure 1.16) has been designed to have a very high capacitance ratio (C_{up}=21 fF, C_{down}=4.55 pF, $C_{down}/C_{up} > 200$) between the capacitance in the un-actuated state and the capacitance of the actuated one. This high capacitance ratio leads to very good RF-performances in terms of insertion losses (0.6 dB at 30 GHz), return losses (-27 dB at 30 GHz) and isolation (down to -58 dB at 27 GHz), as depicted in figure 1.17a and figure 1.17b respectively. Typical device actuation voltage is around 30 V.

Spring anchor ohmic switch (BAT)

The spring anchor ohmic switch (BAT) has been designed with the aim to obtain a winged stopping pillars switch (like PSX) but with a lower actuation voltage. In figure 1.18, an image

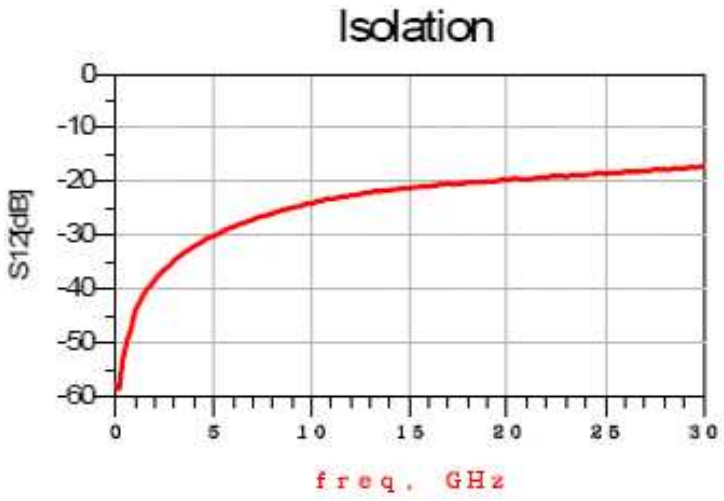

(a)

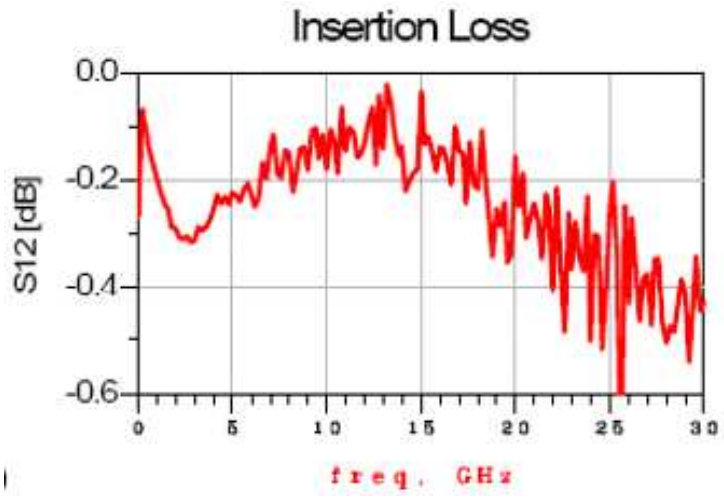

(b)

(c)

Fig. 1.15: Isolation vs frequency (a), insertion losses (b) and return losses (c) of a series ohmic cantilever switch (CA).

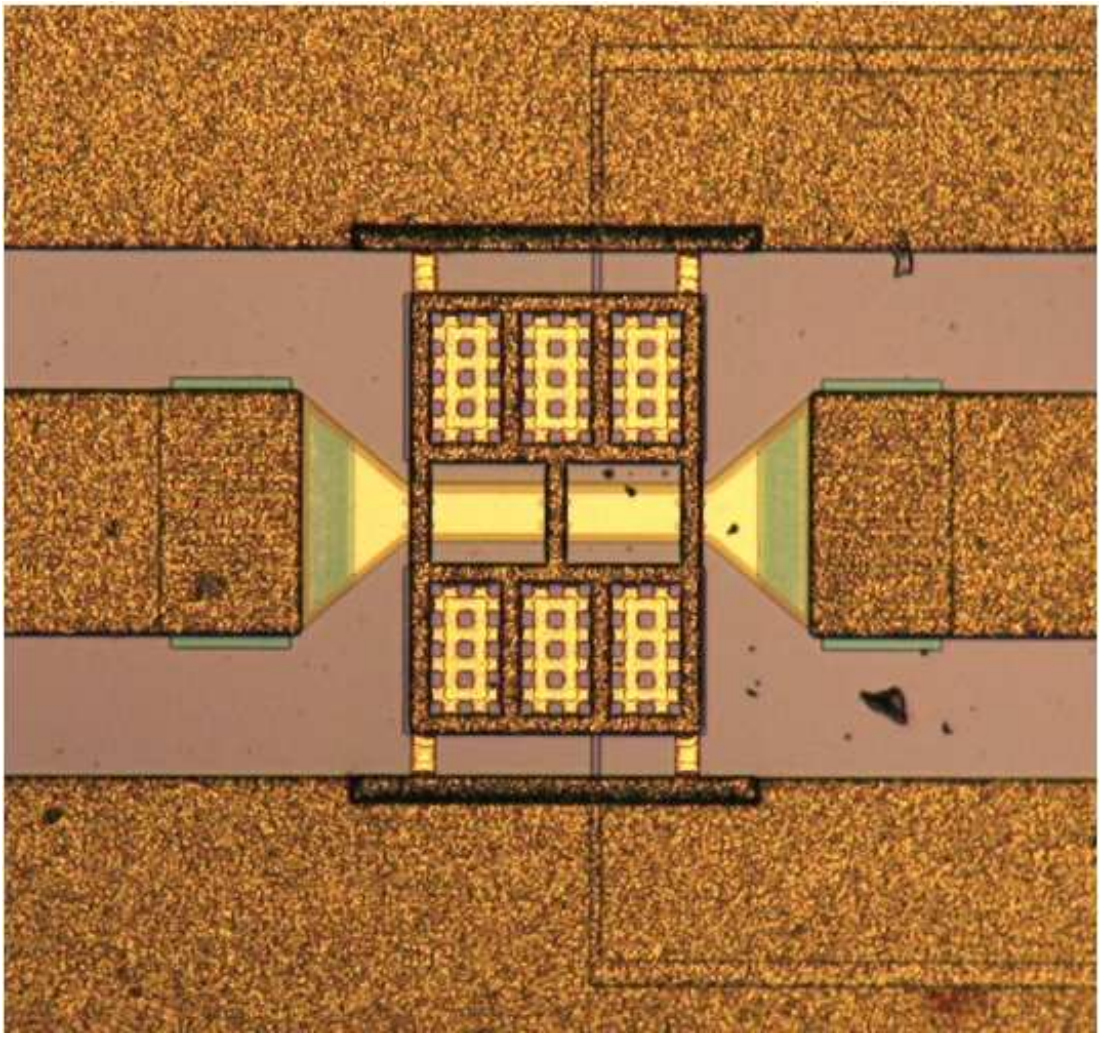

Fig. 1.16: Photo of the boosted ohmic shunt MEMS switch.

of the device is presented where the bended beams design can be appreciated.

As it has been discussed in the par. 1.1, a bended anchoring beam leads to a weaker spring constant for the structure, reducing the actuation voltage which is depending on it. For these devices, low actuation voltages have been measured (between 15 and 30 V). From an RF point of view, the spring anchor ohmic switch has shown a very good behavior in terms of insertion losses (about 0.5 dB on the whole broadband, see figure 1.19a), of return losses (about -25 dB on the whole broadband, see figure 1.19a) and isolation (-20 dB at 30 GHz, see figure 1.19b). Moreover, the measurement results are in good correspondence with the devices simulation as shown in figure 1.19a and figure 1.19b, with an exception for the low frequency range where the probable presence of parasitic oxide on the via contact tends to block the RF signal inverting the RF device expected behavior.

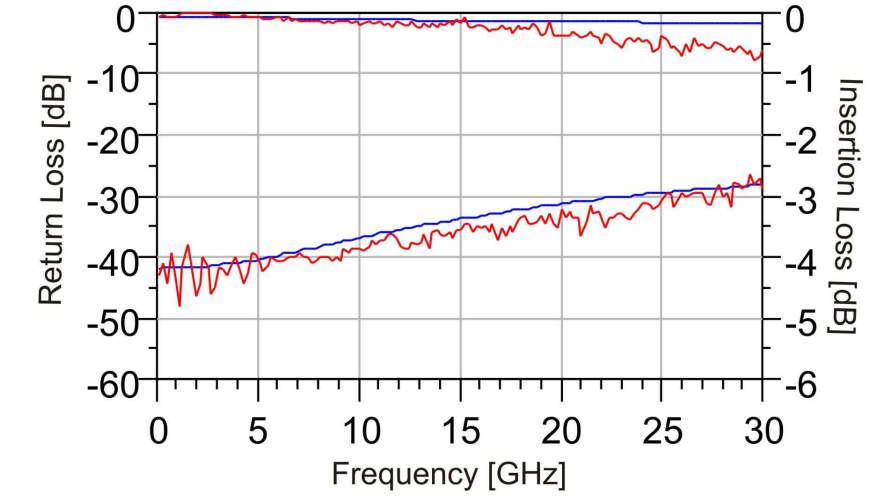

(a)

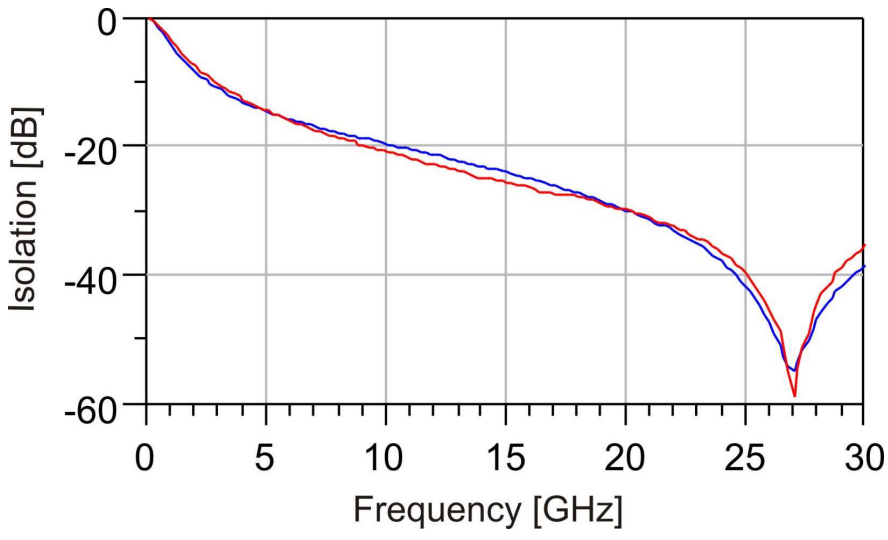

(b)

Fig. 1.17: Simulated (blue line) and measured (red line) insertion losses and return losses of a boosted ohmic shunt switch (a). The device isolation show a negative peak at 27 GHz *in good correspondence with simulations (b).*

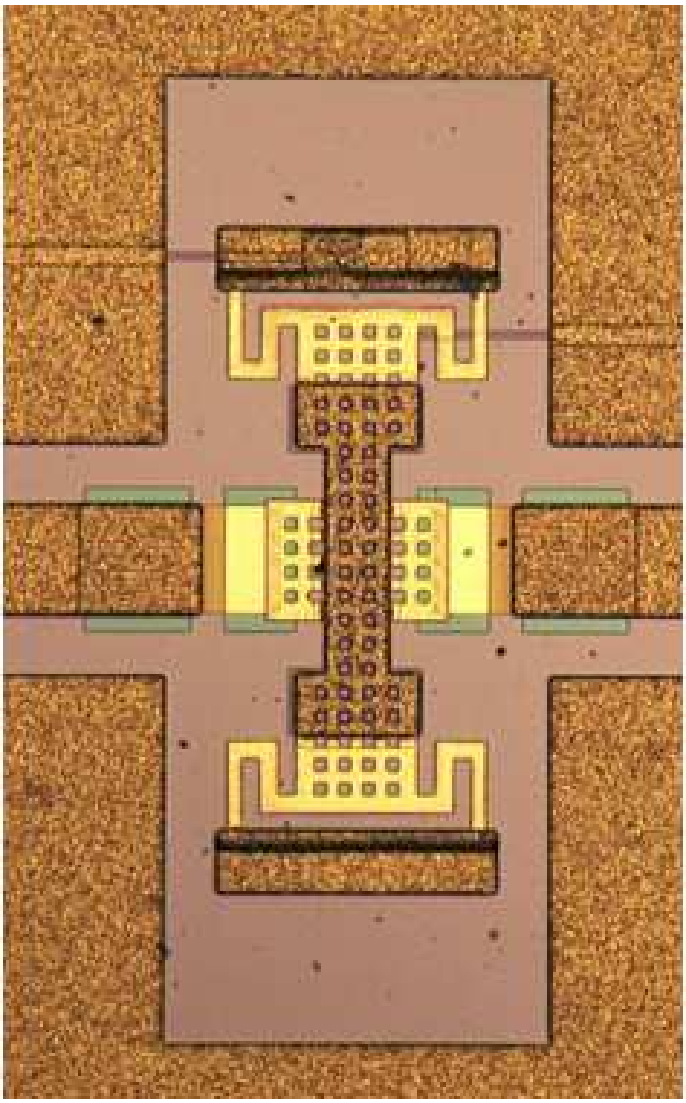

Fig. 1.18: Image of a spring anchor ohmic switch (BAT).

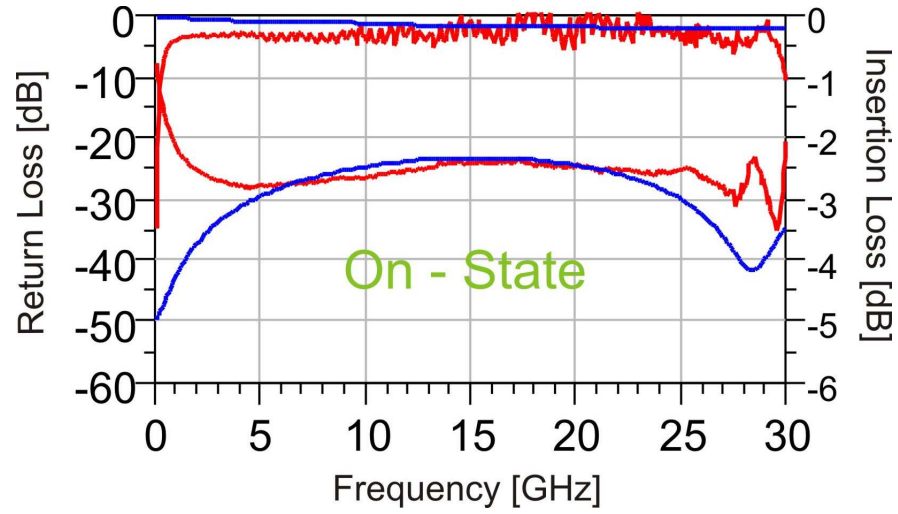

(a)

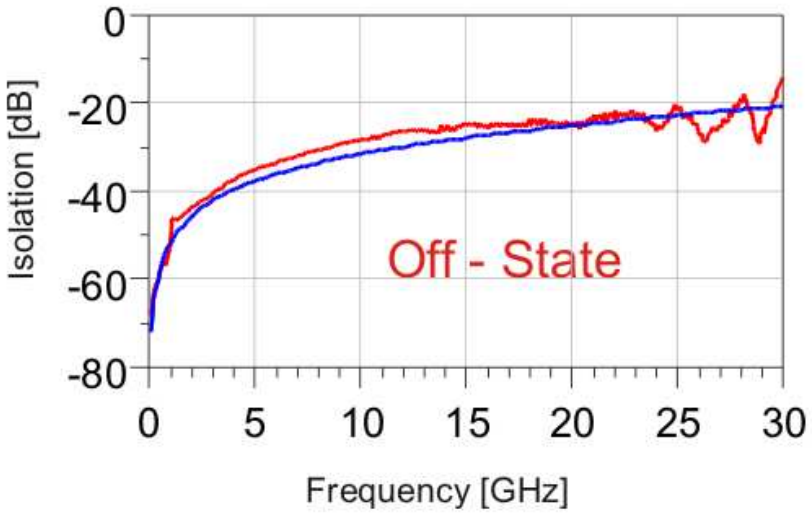

(b)

Fig. 1.19: Simulated (blue line) and measured (red line) insertion losses and return losses of a spring anchor ohmic switch (a). The device isolation show a good behavior up to 30 GHz *with a* -20 dB *value (b).*

Chapter 2

Reliability of RF MEMS switches

Emerging and future autonomous wireless communications systems require highly reliable electronic components with very low power consumption. Micromachined devices present a promising technology to meet this demand. RF-MEMS are specific micromechanical switches designed to operate at RF-to-millimeter-wave frequencies (0.1 to 100 GHz). Such RF switches have been demonstrated with low loss, low power consumption, low distortion, and higher off-state isolation as compared to p-i-n diodes or field effect transistors. However, before such switches can be used in commercial or spatial applications, they must demonstrate the ability to switch reliably over billions of cycles, or, as in the case of a redundancy switch, to maintain their electrical and RF performances for a very long time and guarantee the switch actuation even after years of storage in harsh environment. The presence of mechanical contact introduces a whole new class of reliability issues related to both mechanical and electrical phenomena [11, 12]. Cycled mechanical deformations and steady-state vibrations introduce new stress mechanisms on the structural parts of these devices. Mechanical relaxation of residual material stress, plastic deformations under large signal regime, creep formations and fatigue can all impair the stability of electro-mechanical device behavior and eventually cause device mechanical failure. Finally, other surface effects such as oxidation or absorption can also result in changes of effective mass or stress of a moving or vibrating structure, causing stability issues and device failures. Ohmic contacts occurring between two metallic surfaces can also suffer from stability problems due to cycling, resulting in changes in the ohmic contact resistance. The causes can be diverse, such as surface contaminations, material transfer and erosion, and surface changes due to absorption or oxidation. Furthermore, considering that RF-MEMS will be largely employed in space applications (i.e. satellite communications) several issues concerning the radiation tolerance with respect to both total ionizing dose (TID) and single event effect (SEE) must be assessed before they may be successfully employed in radiation harsh environment. Unfortunately, the available literature data concerning RF-MEMS reliability is very poor and no documentation, procedure, guideline or specification are available today for the evaluation of the RF-MEMS robustness. Typical failure mechanisms of MEMS devices can be divided in three classes regarding the nature or the cause of the problem. Because of the electrical and mechanical nature of these kind of devices, some phenomena are also correlated. In the following sections, a description of the main reliability issues is reported,

dividing the nature of the problem in electrical, environmental, and mechanical causes. This yet non-exhaustive collection of possible reliability and failure mechanisms occurring in RF-MEMS devices depicts a very complex scenario for lifetime testing. For this reason this new class of devices, needs the definition of new methodologies, device degradation models, and accelerated tests criteria, all covering different and cross-coupled physical domains.

2.1 Electrical phenomena

2.1.1 Dielectric charging

Dielectric charging is described in literature as the main failure mode for capacitive switches [13, 14, 15]. It is caused by charges trapping in an insulator. This can be both positive and negative charging and interest both the bulk interface and surface. There can be different reasons that cause dielectric charging. If a large electric field is present over the dielectric, it can cause charge trapping due to Poole Frenkel or Fowler-Nordheim tunneling. The presence of surface states can affect charge trapping. Also radiation can induce electron-hole pairs in an insulator. If an electric field is present, these carriers can become trapped before they recombine. All devices where an insulator is present can suffer from this problem. Charging is accelerated at higher electrical fields. So, tests at higher actuation voltages can accelerate the problem. Humidity can affect charging. Also the environmental gas (ex. N_2 compared to air) has been reported to affect the charging mechanism, N_2 giving a better lifetime. Radiation can also give rise to charging. It can be reduced by applying different actuation schemes to the capacitive switch, such as bipolar actuation and by reducing the actuation voltage as much as possible or removing the charges by other means. The dielectric charging can have two consequences:

- *Screening*: Charge entrapment produces parasitic electric fields that can screen the effect of the applied voltage, see 2.1a. This typically leads to a variation of the actuation voltage needed to properly actuate the device. In the case of a bipolar actuation, charge trapping leads to a not symmetrical actuation characteristic [16].

- *Stiction*: It occurs when the entrapped charge creates an attraction force strong enough to hold the bridge in the down-state position even when the actuation signal is removed, see figure 2.1b [15, 16, 17].

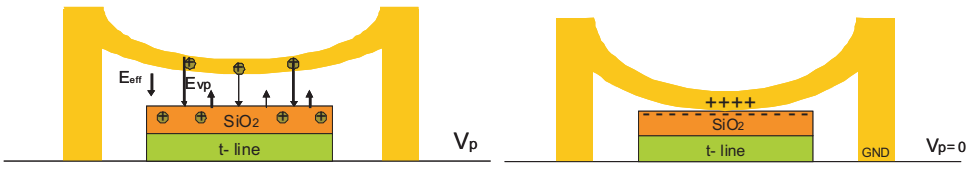

(a) Screening *(b)* Stiction

Fig. 2.1: Schematic of charge distribution causing the partial screening of the actuation voltage (a) and the stiction of the suspended gold membrane (b).

Theoretical analysis

Assuming that the MEMS switch acts as a parallel plane plates capacitor, the switch capacitance for unit area is:

$$C = \frac{\epsilon_0 * \epsilon_1}{\epsilon_0 * h_1 + \epsilon_1 * h_0}$$

where ϵ_0 is the air dielectric constant, ϵ_1 is the material dielectric constant, h_0 is the distance between the suspended bridge and the dielectric, h_1 is the dielectric thickness. If a sheet of charge with charge density ρ_s is inserted inside the dielectric, the electrostatic force for unit area on the suspended bridge due to the actuation voltage V and the sheet charge will be:

$$F = \frac{\epsilon_0}{2}\left\{\frac{V - \frac{(h_1 - \Delta h_1)\rho_s}{\epsilon_1}}{\frac{1}{\epsilon_1}[\epsilon_0 h_1 + \epsilon_1(h_0 - \Delta h_0)]}\right\}^2$$

where Δh_0 is the membrane deflection from the rest position, and Δh_1 is the distance of the charge sheet center from the dielectric upper surface. In fact, the actuation voltage drift due to the charge presence into the dielectric is given by:

$$\Delta V = \frac{(h_1 - \Delta h_1)\rho_s}{\epsilon_1}.$$

This means that a nearer to surface sheet of charge will affect the actuation voltage drift more than a deeper one. Equating the electrostatic force generated by both the biasing voltage and the charge sheet to the membrane restoring force, it is possible to calculate the biasing voltage vs. deflection:

$$V(\Delta h_0) = \frac{1}{\epsilon_1}\sqrt{\frac{1k\Delta h_0}{\epsilon_0 A}}[\epsilon_0 h_1 + \epsilon_1(h_0 - \Delta h_0)] + \frac{(h_1 - \Delta h_1)\rho_s}{\epsilon_1}$$

where k is the membrane spring constant and A is the capacitor area. If we assume now that $\epsilon_1(h_0 - \Delta h_0) >> \epsilon_0 h_1$,$V(\Delta h_0)$ has a maximum at $\Delta h_0 \approx \frac{h_0}{3}$ and $V\left(\frac{h_0}{3}\right) \approx V_{Act}$, where V_{Act} is the device actuation voltage. If we use a linear approximation of the spring restoring force, in the actuated position ($h_0 = 0$) this force will be about three times greater than at $\frac{h_0}{3}$ (where $V(\Delta h_0)$ is maximum). This means that the electrostatic force needed to keep the membrane bended should be three times stronger than the pull-down force. However, the hold-down voltage V_h is typically lower than the pull-down one (V_{Act}) for $\epsilon_1 h_0 >> \epsilon_0 h_1$. If, i.e., the device under test has an actuation voltage of 10 V, the electrostatic force for area unit will be $61\ \mathrm{N/m^2}$. When the membrane is completely actuated, if a charge sheet with charge density $\rho_s = 7.5 * 10^{10}\ \mathrm{cm^{-2}}$ is present into the center of dielectric, an attraction force of $200\ \mathrm{N/m^2}$ is generated. Such a force should be enough to maintain the membrane in the actuated position. However, such a charge sheet would reduce the actuation voltage of a 5% only underlining how the dielectric charging is more critical for the hold down voltage than the actuation one.

2.1.2 Dielectric breakdown

Dielectric breakdown happens if a conduction path grows through an insulator making it conductive [18]. The conduction path is created either through an increasing number of traps, or through damage of the dielectric causing a short. It is not always visible. It can cause local stiction of one part to another. If a high current come together with the event, then burned spots can sometimes be seen, or local damage (holes). In some cases where the MEMS is moving vertically, such as a capacitive switch, the bridge might have to be removed to see the failure. Eventually a FIB cross-section has to be made to show the local stiction point. Dielectric breakdown can in some cases also be observed optically, through photon emission microscopy. Source of the breakdown can be:

- High electrical field across an insulator during a long time causing trap generation and eventually breakdown
- Electrical overstress
- Electro-static discharge
- Sparking
- Air-gap breakdown

It results in a shorted and thus in a non-functional device.

2.1.3 Power handling

The RF signal power flowing through the switch (with a micro-metric dimension of the structure) can bring to either logical or physical reliability issues. Logical issues are related to some malfunction of the device that can be auto-actuated even if the actuation signal is not applied. These events are named:

- *Self-actuation*: a strong enough energetic RF signal can have a DC component sufficient to accidentally actuate the device.
- *Latching*: a strong enough energetic RF signal can have a DC component equal to the hold-down voltage. In this case the bridge will be no more released [19].

Physical issues are typically related to electromigration phenomena [20]. It deals with the high current that propagates within the transmission lines and within the upper membrane. It is well known that high current can generate electromigration effect that degrades the conductivity of the metallization leading to an increase of the temperature through a rise of ohmic losses. Furthermore, in RF regime the electromigration impact is not similar to the impact in DC one. Due to skin effect, in fact, when the operating frequency is increasing, this leads to a higher concentration of the current lines. This current concentration can easily cause line melting due to the material removal and the subsequent high temperature that it can reach. In figure 2.2 it is possible to see how an high current flow can damage the switch membrane generating bubbles caused by local heating.

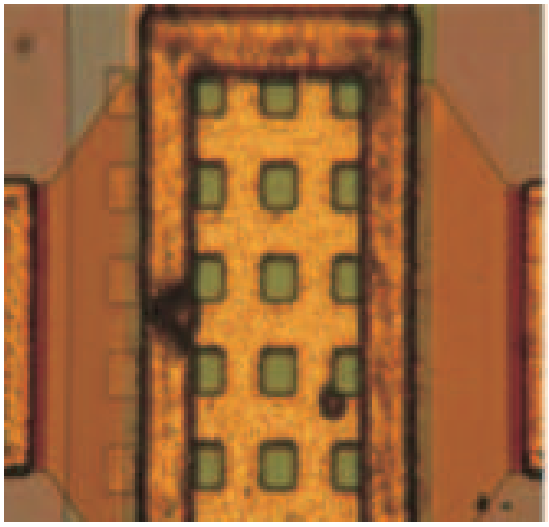

Fig. 2.2: Bubbles due to high current inducing membrane fusion.

Theoretical analysis

It is well known from the theory [3] that the actuation voltage of a suspended membrane can be approximated with:

$$V_{Act} = \sqrt{\frac{8kg_0^3}{27\epsilon_0 A}}$$

where k is the spring constant, g_0 the gap between the bridge and the dielectric beneath it, A is the actuation area and ϵ_0 is the vacuum dielectric constant. If an RF signal with V_0 amplitude is applied to the switch membrane, a DC component will be generated. This will be equal to:

$$V_{DC} = \frac{V_0}{\sqrt{2}}$$

and the equivalent power at the switch input port will be:

$$P_{IN} = \frac{V_0^2}{2Z_0}$$

If the actuation voltage V_{Act} is lower that the DC component generated by the RF signal, the switch will suddenly actuate itself. Typically the necessary power to actuate a capacitive switch is about 4 W[19]. On the contrary, for the latching phenomena, the RF power to keep a device actuated is lower (about 510 mW). It is important to observe that every RF signal that will pass through the device will generate a DC components that will further the switch actuation, and this is a parameter to take into account during the project phase. However, the maximum current density (J_{Max}) tolerable in RF mode is about forty times larger than the DC mode. In table 2.1 is reported the current density that generates electro-migration in both RF and DC mode for different RF power signals. Typically the tested devices have been measured with a 0 dBm RF signal (1 mW), a power that should not generates electromigration or self actuation

Power Max @ 18 GHz	J_{Max} (GA/m^2)	J_{MaxRF}/J_{MaxDC}
17.8 W	185	37
20 W	196	39
22.4 W	207	41

Table 2.1

phenomena.

2.1.4 Contact resistance variation

This reliability issue is typically related to resistive switches. The aging of the switch can bring to an increase of the contact resistance. This can then lead to an increase of the temperature at the contact point and finally to a failure of the switch. Furthermore, the increased resistance in the closed state can become comparable to the resistance exhibited in the open state, impairing the function of the switch. In figure 2.3 it is possible to see the comparison between apparent contact area and the real contact area in a gold-gold metal contact. The reduced size of the contact point increases the series resistance of the device degrading its electrical performances [21, 22].

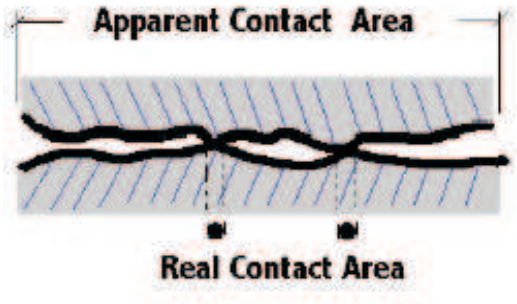

Fig. 2.3: Comparison between apparent contact area and real contact area in a gold-gold metal contact.

Theoretical analysis

The contact resistance is generated by the roughness of two surfaces that get in contact. In fact, when two surfaces adhere, only a finite number of points really get in contact. This leads to a reduction of the effective surface for the current flowing which increases the resistance of the electrical path. Moreover, for a contact with a radius similar to the electron mean free path (10 nm) or smaller, the current flowing is constricted also by the scattering around the contact (boundary scattering). Taking into account these phenomena, the contact resistance can be approximated with:

$$R_s = \frac{1 + 0.83(l/a)}{1 + 1.33(l/a)} \frac{\rho}{2a} + \frac{4\rho l}{3\pi a^2}$$

where R_s is the contact resistance, l is the mean free path, a is the contact radius and ρ is the electrical resistivity. The typical radius for two adhering materials is:

$$a = \sqrt{\frac{F_c}{\pi H}}$$

where F_c is the contact force and H [Pa] is the material hardness which can be obtained with standard tests, e.g. the Knoop method [23]. Due to the Joule law, a current flowing through a contact tends to heat it up to a technical temperature called "supertemperature". This temperature can be hundreds of degrees higher than the surrounding material one. If we assume that the Weidemann-Franz law is valid for metals and that the current and the thermal flow have the same direction, the supertemperature is given by:

$$T_s^2 = \frac{V^2}{4L} + \frac{L(\mathrm{T_b^2} - \mathrm{T_0^2})^2}{4V^2} + \frac{T_b^2 + T_0^2}{2}$$

where T_s is the supertemperature, V the voltage drop on the contact, L is the Lorentz constant ($2.47 * 10^{-8}\ \mathrm{V^2/K^2}$), T_b is the membrane temperature near to the contact zone, and T_0 is the substrate temperature. Tests carry out on macro-scale have shown that the contact resistance grows with the supertemperature [22]. However, after the overcoming of the supertemperature, a softening of the contact happens with a consequentially increase of the contact radius and a reduction of the electrical path resistance. The contact area variation is approximated by:

$$\frac{A}{A_0} = \frac{R_0^2}{R^2}\left[1 + \frac{2\,\mathrm{L}}{3\,\mathrm{k}}(\mathrm{T_s} - \mathrm{T_o})\right]^2$$

where A is the softened contact area, A_0 is the contact area before the softening, R is the softened contact resistance, and R_0 is the contact resistance before the softening.

2.1.5 Metal - metal welding

Metal-metal welding is the joining of materials, usually metals, by coalescence. It happens if soft metals come into contact with high forces, at local high temperature, and/or high current (ESD, spikes, dielectric or airgap breakdown), causing stiction and/or damage at the contact point [18, 21, 22]. As a material transfer can happen, the contact area may be reduced by increasing the roughness of the contact, even if the switch will not stick. In this case, an increase in contact resistance in an ohmic switch or anomalous switching behaviour is observed. Ohmic switches are mostly concerned. Several studies have been performed by Radant MEMS to improve contact reliability. The use of refractory metals like Tungsten could help to increase the contact lifetime. Aluminum is there the worst case of study since its welding temperature and adherence voltage are very low. It results in degradation and eventually failure of the device, or direct failure in case of sticking.

2.2 Environmental phenomena

2.2.1 Capillarity stiction - Humidity effects

Surface micromachined devices, for reasons related to processing, are extremely hydrophilic. An hydrophilic surface in a humid atmosphere will experience both condensation, which will create bending moment in structures, and capillary forces, which will create stronger adhesive bonds than Van der Waals forces alone [13, 24, 25, 26]. Water or fluid that is present in a small cavity between two moving parts or a moving and a fixed part can keep them together due to its liquid surface tension [18, 24, 25, 26]. The stiction force depends on the roughness of the surfaces (the rougher the smaller the force), on the temperature, and on the pressure of the environment. Stiction can be best observed using a optical microscope, motion analysis instrumentation (the stuck part will of course not move), or a profilometer. Stiction can also be observed in a SEM but best in a low-vacuum instrument at low voltage (the vacuum can remove the fluid and SEM can induce charging which might also result in stiction). The main occurrence of capillary stiction is after the release etch, i.e. during the drying of the MEMS (due to the water left under the structure pulling it down). Using an appropriate release method can prevent this problem. However, it might also occur during use of the MEMS device in a humid environment. This can be prevented by protecting the MEMS using a hermetic package with a low internal humidity. But also the following factors should be taken into account:

1. MEMS with a large restoring mechanical force (stiff structure) will be less sensitive to capillary stiction than a sloppy MEMS

2. a smoother surface can be more easily affected by stiction.

It usually will occur in an environment with a high humidity or after etch of the sacrificial layer of the MEMS using wet etch methods. Capillary stiction can occur in all MEMS. This is a failure that in general can be avoided by good processing (take care during etch of the sacrificial layer), optimal design (stiff moving parts) and/or protection of the MEMS against high humidity (packaging). In Oya et al.[26], capacitive switches were reported that kept functioning even at humidity levels as high as 95% RH. This indicates that if the restoring forces of the switches are large enough (stiff bridge), capillary stiction will not probably be an issue. Anti-stiction coatings can be used to produce hydrophobic surfaces, although those currently under investigation are only applicable to certain types of devices, and not yet "industry-ready".

2.2.2 Temperature Changes

Internal stresses in devices are extremely temperature dependent. This is due to their inherent mechanical design which allows the substrate to induce changes in the stress state of the mechanical membrane over temperature [27]. The sparse data that have been published on this topic demonstrates variations in the range of 0.3-0.5 V/C° [28, 29]. Over a broad temperature range, this can lead to excessively large supply voltage variations. Additionally, operation at high voltages (necessary for low temperatures) can also adversely impact device longevity [30]. On the contrary, low temperatures can increase dielectric charging effects (especially holes based). Thermal effects can also cause problems in metal packaging.

Temperature induced elastic deformation

Differences in the coefficient of thermal expansion (CTE) between two connected materials can lead to temperature induced elastic deformation or non-uniform temperature differences within the bridge of a switch or within a beam. This will cause anomalous buckling of a bridge (or membrane or beam) with temperature changes or during functioning. It is mainly found when materials with large differences in CTE are used, if inhomogeneous heating of a device during functioning occurs, or in designs that do not take expansion into account. Observed are changes in the pull-in/pull-out voltage of switches or changes of the resonance frequency and Q factor in resonators.

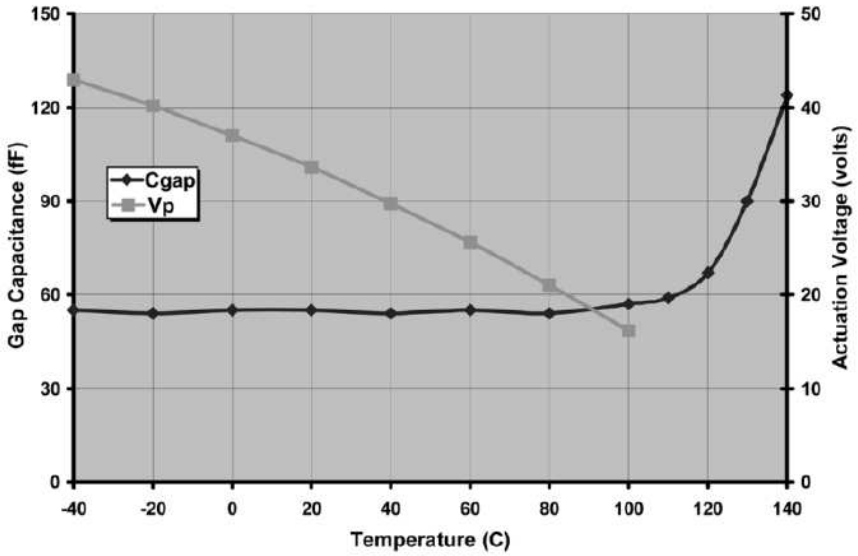

Fig. 2.4: Measurement of gap capacitance (black curve) and actuation voltage as a function of temperature (grey curve).

As example, in figure 2.4 is reported the measurement performed by Glodsmith ([27]) on the variation of the gap capacitance and the subsequent variation of the actuation voltage as a function of the temperature for capacitive RF MEMS switches fabricated on Pyrex glass substrates (Corning 7740) with copper posts, gold electrodes, and aluminum alloy membranes. The actuation voltage has been measured only up to 100 C° since this was the heating limit of the used thermal chuck. Most RF-MEMS will suffer from this problem. It strongly depends on the design, the used materials, the RF-power and frequency, whether the effect can be neglected or very severe. RF-resonators are very sensitive and might require a temperature-controlled environment. It is not a permanent failure mode: when the temperature is reduced, the effect reduces. In case of effects due to a uniform increase of the external temperature, temperature compensation should be built in or the MEMS should function only in an environment with a controlled temperature [25, 27].

Temperature induced plastic deformation

Temperature-induced changes in a material (annealing) may cause plastic deformation. These changes might be a stresses alteration, a softness, a ductility, a toughness, a electrical or magnetic or other physical properties change. It goes together with changes in crystallinity and micro-structure. All materials have a critical temperature above which the material properties change (grain growth, dislocation motion, etc.). If this temperature is exceeded during functioning or processing or packaging, the device will deform in a irreversible way, like anomalous and irreversible deformation of a bridge or membrane or beam when submitted to a high temperature step. More danger of plastic deformation exists if materials with a low melting temperature such as for example Al or most Al-alloys are used. Material and shape changes will result in changes of the stiffness of the beam or bridge which will affect several electrical parameters: changes in the pull-in/pull-out voltage of switches can occur. Mostly MEMS with metal parts (e.g. Al bridges) are affected. The damage is irreversible. Even if the device is not dead, it will certainly have different electrical parameters and a different reliability.

2.2.3 Space Environment - Radiation Effects

It has long been known that electrical systems are susceptible to radiation and recent research has raised the possibility that mechanical devices may also be prone to radiation-induced damage. Especially sensitive to radiation could be devices that have mechanical motion governed by electric fields across insulators, such as electrostatically actuated cantilever beams. Radiation can cause bulk lattice damage and make materials more susceptible to fracture. High Z radiation can lead to fracturing by creating massive disorder within the crystal lattice. It is also possible that dielectric layers will trap charged particles, creating a permanent electric field, that could interfere with the nominal behavior of the switch. Furthermore, some radiations can have an impact on the Young module, changing the actuation voltage and the spring constant. In table 2.2 a list of space environmental hazards in different regions of space is reported. The notes to follow focus on the columns labeled single event effects and total dose, but it lists other hazards for reference. The column of regions roughly progresses in increasing distance from the Earth, beginning from the ionosphere and moving out to the solar wind (or interplanetary space). The columns of effects are ordered roughly by the energy of the particles responsible for the hazards, decreasing in energy from left to right. The color-coding and numbering are approximate measures of the importance of a particular phenomenon in a particular region. Note that this table does not address the hazards of satellite drag, impacts from meteoroids or space debris, or satellite collisions. The drag is most important in low Earth orbit, while meteoroid impacts and satellite collisions can happen anywhere [31].

In figure 2.5 is shown the distribution of the 299 anomaly records versus the anomaly type. The "other" category included plasma, micrometeoroid impacts, and uncategorized solar energetic particle effects. Effects from electrostatic discharge had the largest number of records, while single event effects and radiation damage together accounted for 33% of the cases [32].

In figure 2.6 is shown the Single Event Up-set (SEU) and radiation damage records broken into several subcategories. The largest subcategory (41%) was the uncategorized SEU: their origin may have been galactic cosmic rays or solar energetic particle events for which there

Region	Single Event Effects			Total Dose		Charging		Plasma Effects			
	Galactic cosmic rays	Trapped heavy ions	Solar energetic particles	Trapped radiation	Solar energetic particles	Surface charging	Internal charging	Ion sputtering	Scintilla-tion	Plasma wave refraction	Surface erosion from O^+
Ionosphere	1	0	0	0	0	0	0	1	2	2	2
South Atlantic Anomaly	1	2	0	2	0	0	0	1	0	0	0
Inner radiation belt	1	2	0	2	0	0	0	0	0	0	0
Auroral zone	2	0	2	0	2	1	0	1	0	0	0
Polar cap	2	0	2	0	2	0	0	1	0	0	0
Plasmas-phere	2	0	0	0	2	0	0	1	0	1	0
Plasma sheet	2	0	0	0	2	2	0	1	0	0	0
Outer radiation belt	2	1	2	2	2	2	2	1	0	0	0
Outer magneto-sphere	2	0	2	0	2	1	2	1	0	0	0
Geomag-netic tail	2	0	2	0	2	0	0	1	0	0	0
Solar wind	2	0	2	0	2	0	0	1	0	0	0

Table 2.2: List of space environmental hazards in different regions of space: 0 - Unimportant, 1 - Relevant, 2 - Important.

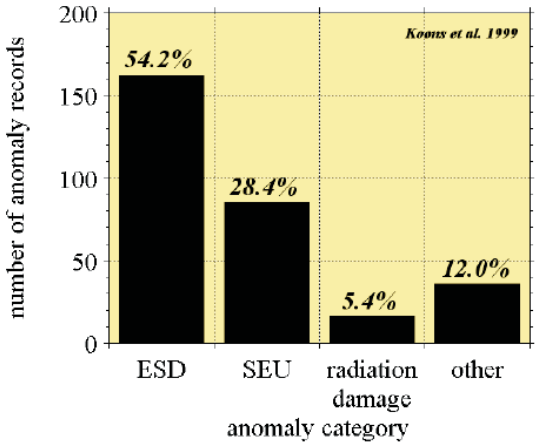

Fig. 2.5: Breakdown of Single Event Up-set (SEU) and radiation damage anomaly records (data from Koons-99).

was no detailed correlation done with the environment. Radiation damage anomalies were infrequent compared to the other effects. Within the radiation damage category, there were only 3 records (1%) corresponding to total radiation dose. Such a low frequency might therefore reflect conservative limits in radiation modeling and conservative shielding. The anomaly records did not quantify impacts such as cost or delays in launches of similar, follow-on spacecraft. The most visible impact is mission loss or termination, and Koons et al. listed 11 such cases [33]. For reference, 3 of these losses were diagnosed as SEU effects, 1 as total radiation dose. The only other impact that could be easily quantified in the Koons et al. survey was the time it took the spacecraft operators to recover from the anomaly. To focus on the impacts of single event effects and radiation damage (roughly one third of the anomaly cases), in the case of SEU events, automatic recovery using on-board correction algorithms probably accounted for the events of minimal duration [32].

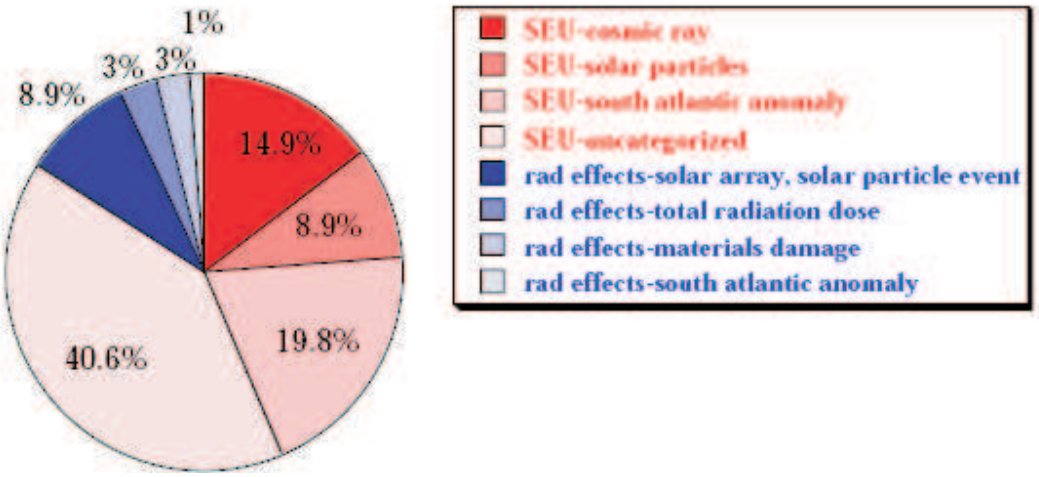

Fig. 2.6: Breakdown of SEU and radiation damage anomaly records (data from Koon-99).

Finally, in the table 2.3 it is possible to see missions lost or terminated due to the space environment as of early 1999 [32, 33].

Diagnosis	Vehicle	Orbit	Date
Single Event Effect	Feng Yun 1	LEO	Jun-98
	MSTI	LEO	Jan-93
	IRON 9906	LEO	1997
Total Radiation Dose	Hipparcos [1]	GTO	Aug 1993
Surface ESD	DSCS II	GEO	Feb-73
	GOES 4	GEO	Nov-82
	MARECS A	GEO	Mar-91
	INSAT 2D	GEO	Oct-97
Micrometeoroid impact	Olympus	GEO	Aug-93
	SEDS 2 [1]	LEO	Mar-94
	MSTI 2	LEO	Mar-94

Table 2.3: Missions lost or terminated due to the space environment as of early 1999.

2.2.4 Vibration

Due to the sensitivity and fragile nature of many MEMS, external vibrations can have disastrous implications. Either through inducing surface adhesion or through fracturing device support structures, external vibration can cause failure because of either resonance and dynamic instability. Long-term vibration will also contribute to fatigue even due to thermal stress. For space applications, vibration considerations are important, as devices are subjected to large amplitude vibrations in the launch process [18]. In figure 2.7 it is possible to see an example of cracks in a MEMS support beam caused by vibrations from a launch test performed by the Jet Propulsion Laboratory (the report does not specify if the crack has been due to cyclic loads or to impulsive load).

2.2.5 Shock

It differs from vibration in such a way that shock is a single mechanical impact instead of a rhythmic event. Shock creates a direct transfer of mechanical energy across the device. Shock can lead to both adhesion and fracture. Shock can also cause wire bond shearing, a failure mode common to all semiconductor devices. It is also called Pyrotechnic Shock when it is associated with the firing of an explosive device, usually for the purpose of initiating or performing a mechanical action. Spacecraft separation events or the release of propulsion system saving devices are typical such mechanical actions [18].

2.2.6 Particulates

They are fine particles, that are prevalent in the atmosphere. These particles have been known to electrically short out MEMS and can also induce stiction. An hermetically sealed package is then required if particular precautions are not undertaken in the design phase [18].

[1] Missions completed prior to termination.

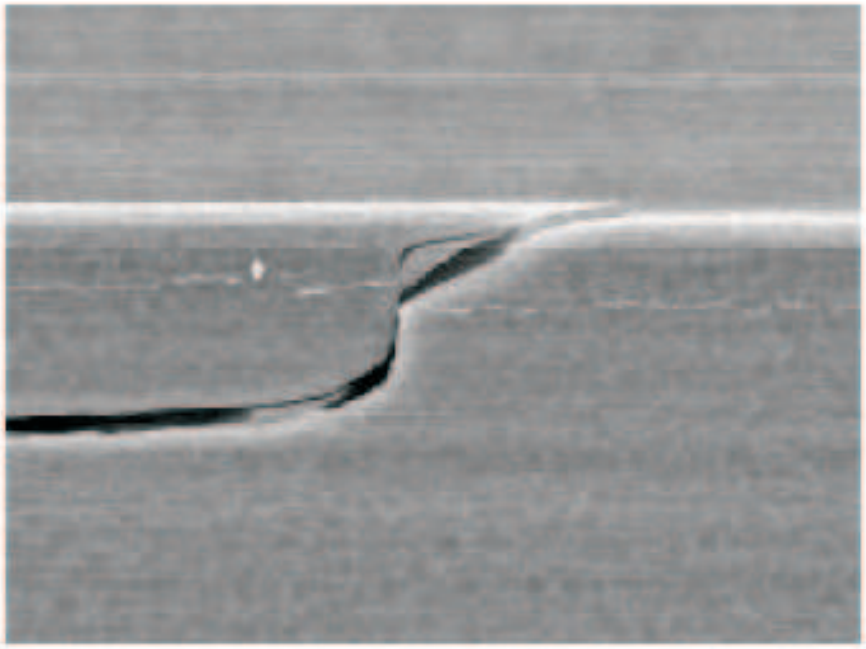

Fig. 2.7: Cracks in single crystal silicon support beams caused by vibrations from a launch test.

2.2.7 Electro-static discharge and electrical over-stress

Electrical over-stress (EOS) is a common term referring to voltage / current beyond the nominal values of the device. ESD typical occurs when a device is improperly handled or gets in contact with a charged body. These effects are known to have catastrophic effects in traditional solid state circuits and also in MEMS [34, 35]. Despite for traditional solid state circuits a lot of in-circuit protection structures have been presented, MEMS technology typically does not exhibit the ability to implement similar protection schemes. For this reason, the reliability to ESD of such devices must be thought starting from the design phase. In figure 2.8a it is possible to see the I-V characteristic of a shunt MEMS switch stressed between the actuation and the RF ground plate. In figure 2.8b it is possible to notice a photo of fatal damages of the actuation fingers and transmission line ones caused by ESD-like events. The ESD effects on RF-MEMS switches will be deeply discussed in chapter 5.

2.3 Mechanical phenomena

2.3.1 Fracture

Mechanical fracture is defined as the breaking of a uniform material into two separate sections [18]. In MEMS it will always lead to the catastrophic failure of a device. There are three types of fractures: ductile, brittle, and intercrystalline fracture.

- Ductile fracture: it is characterized by an almost uninterrupted plastic deformation of a material. It is usually signified by the necking, or extreme thinning, of a material at one

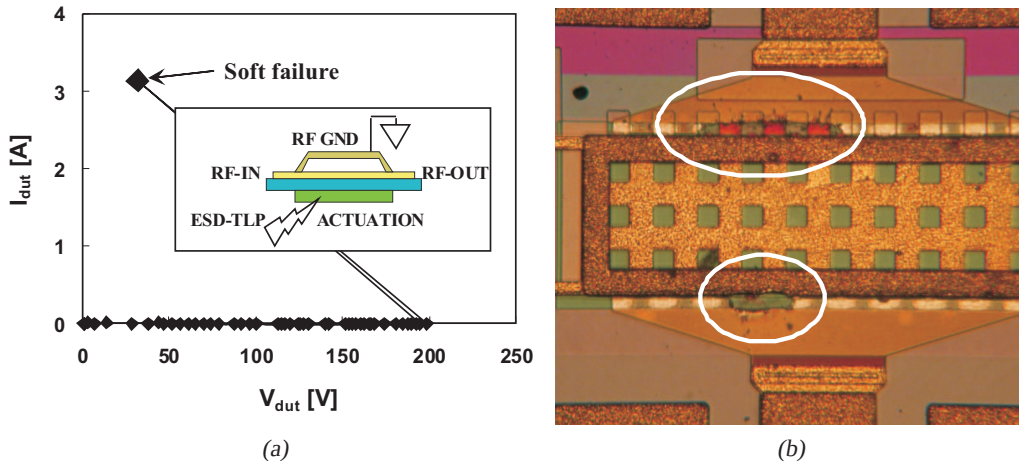

(a) *(b)*

Fig. 2.8: I-V characteristic of a resistive shunt MEMS ESD-like stressed between the (electrically not connected) actuation and RF-ground plate pads (a) and an example of fatal damage induced by ESD-like stress. (b).

specific point;

- Brittle fracture: it occurs along crystal planes and develops rapidly with little deformation;

- Intercrystalline fracture: it is a brittle fracture that occurs along grain boundaries in polycrystalline materials, often beginning at a point where impurities or precipitates accumulate.

For MEMS the latter two types of fracture are more common. These kind of fracture can be caused by different mechanisms of fatigue.

2.3.2 Fatigue

Fatigue is a failure mechanism consisting of a decreasing of material strength due to cyclic loads. After a nucleation of damage, crack initiation occurs then propagates through the structure up to a final collapse caused by brittle rupture. It is a time dependent phenomenon affecting mechanical behaviour of MEMS devices. The crack can start at the surface (local high stress location points at for example rough surfaces) or in the bulk (defects growing). It can grow because of the stress changes at the crack tip (where high local stress is present) during cyclic loading, or due to stress corrosion cracking (in crystalline Si: the crack grows because of faster oxide growth at high tensile stress regions near the crack tip). The reason is a large motion inducing changing stresses near stress concentration points. Such points may be at sharp edges, rough surfaces or inside non-uniform material. Therefore it is mainly seen in fracture of beams or hinges, cracks at places where motion takes place and high stress is present (e.g. sharp edges of moving hinges). Observed can be a shift of electrical parameters (pull-in voltage, resonance frequency...). Fatigue can occur in all MEMS device. The cyclic loading leads to the formation of surface micro-cracks that cause the slow weakening of the material over time and create

localized plastic deformations. Fatigue also causes a gradual change in the properties of a material. MEMS devices where a lot of cyclic motion is present may be more susceptible. It is a non-reversible process, resulting in permanent damage [18].

2.3.3 Creep

When a load is applied to a material, its strain response consists of a rapid elastic elongation related to the Young modulus and a time dependent term. The latter is due to creep. The classical definition of creep is "a time-dependent deformation of a sample caused by external mechanical loads, even constant over time". A possible way to observe creep generation is by looking at the time depending stress relaxation. Most metals exhibit creep at temperatures higher than 2/3 of its melting point. Creep can be observed as in the slow deformation of movable metal parts. Regarding the package, it is seen in the fracture of solder joint (can sometimes be seen by scanning acoustic microscopy, or microscopy or SEM on a cross-section). Creep is caused by high stress or stress gradients in metals that are creep sensitive (e.g. Al and solder alloys) combined with high temperatures (ex. at high RF power and large CTE difference of materials. Creep can be detected in the shift of electrical parameters (pull-in voltage, capacitance swing, resonance frequency,...). It is evident only in devices and packages with metal parts (such as Al bridges, solder joints) that are creep sensitive and especially in devices working at high power and high frequency, resulting in high local T in the metal parts combined with mechanical stress in these parts or devices working in an environment with high temperature. It is a non-reversible process, resulting in permanent damage [18].

2.3.4 Wear

It is an event caused by the motion of one surface over another. It is defined as the removal of material from a solid surface as the result of mechanical action. Causes of wearing are: adhesion, abrasion, corrosion, and surface fatigue. Due to the polishing of the contact surfaces caused by wear, the adhesive forces increase [18].

2.3.5 Delamination

It is a condition that occurs when a materials interface loses its adhesive bond. It can be induced by a number of means, from mask misalignments to particulates on the wafer during processing [18].

2.3.6 Stray stresses

They are failure mechanisms that are endemic to thin film structures. Stray stresses are defined as stresses in films that are present in the absence of external forces. In MEMS small stresses cause noise in sensor outputs and large stresses will lead to mechanical deformation. This mechanical deformation can impair the device functionality changing the nominal condition of working [18].

Chapter 3

RF MEMS switches basic characterization and cycling

RF-MEMS switches, as their traditional counterpart, can be realized as either normally open or normally close switches. Both topology can be realized with resistive-based (ohmic) or capacitive-based devices, depending on whether the device exhibits a metal-metal contact, rather than a Metal-Insulator-Metal (MIM) structure. An ideal series switch acts as an open circuit when it is in its rest position (no actuation voltage applied), or it acts as a low impedance path for the RF signal when a proper actuation voltage is applied, as sketched in figure 3.1a (S_{11} and S_{21} are respectively the reflected and the transmitted power coefficients).

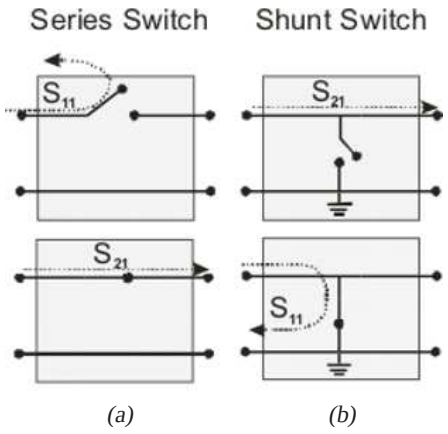

Fig. 3.1: Schematic representation of ideal series (a) and shunt (b) switches, in the un-actuated (top), and actuated (bottom) states. S_{11} represents the reflected power at the input, while S_{21} represents the transmitted power from input to output.

On the contrary, a shunt device exhibits a low impedance path for the RF signal when not-actuated, or a high impedance path for the RF signal from the input port versus the output one (a low-impedance path to ground) when actuated, see figure 3.1b. Capacitive switches have a thin dielectric layer deposited on the transmission line avoiding the metal-to-metal contact, and the short-to-ground effects is obtained with the increasing of the MEMS capacitance, acting as a low impedance path for high frequency signals.

The mechanical system implemented to obtain the change of state is quite simple: a suspended gold membrane over the transmission line, when electrostatically bended, connects the input with the output ports in the series configuration, or the input port to ground in the shunt topology. Figures 3.2a and 3.2b show that, in order to bend the MEMS membrane down until the contact is achieved, it is sufficient to apply an actuation voltage between the suspended membrane and the actuation structure.

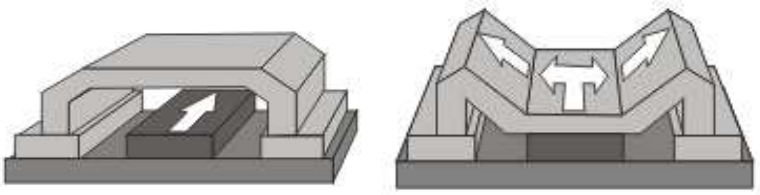

(a) *(b)*

Fig. 3.2: Mechanical actuation of the MEMS membrane in a shunt topology: the suspended bridge (in its rest position see (a) is electrostatically bended (b)) changing the relative impedance of the input path versus the output one.

3.1 Device basic electrical characterization

The first step to perform approaching a MEMS device is to study the effect of the actuation voltage on both the RF performances and the electrical characteristics of RF-MEMS switches. During measurements it has been observed how the actuation delay time of resistive shunt MEMS decreases on increasing the actuation voltage. As it is possible to see in figure 3.3, the increase of the actuation voltage makes the device actuate faster, reducing the actuation time from $42\ \mu\mathrm{s}$ at $25\ \mathrm{V}$, down to $22\ \mu\mathrm{s}$ at $40\ \mathrm{V}$.

In figure 3.4 the actuation delay as a function of the actuation voltage is reported.

The increase of the actuation voltage gives great benefits also to the RF performances (S-parameters) of the DUT. In fact, as it is possible to see in figure 3.5, the S_{21} parameter gains around $8\ \mathrm{dB}$ from the measurement performed at $25\ \mathrm{V}$ ($-21\ \mathrm{dB}$) to the measurement at $40\ \mathrm{V}$ ($-29\ \mathrm{dB}$), going to exhibit a larger variation from the un-actuated state. Up to now it could be noticed that the increase of the actuation voltage leads only to a better working RF-MEMS switch.

Unfortunately, it has been discovered that large actuation voltages produces unexpected bouncing of the MEMS bridge that can compromise the logical function of the switch. In order to measure the device RF response, being the Vector Network Analyzer (VNA) too slow, a Digital Signal Oscilloscope (DSO) in envelope acquisition mode has been used to extract a value related to the power of the output signal. As it is possible to see in figure 3.6, even if the device has been un-actuated (see the light gray line), some peaks on the output signal appear (black line), indicating that the MEMS bridge tends to actuate again even if there is no more actuation signal. This issue clearly indicates that a trade-off procedure is required in order to choose the optimum actuation voltage necessary for adequate stability and RF-performances. The presence of bouncing in the release phase will be further investigated in the chapter 4 .

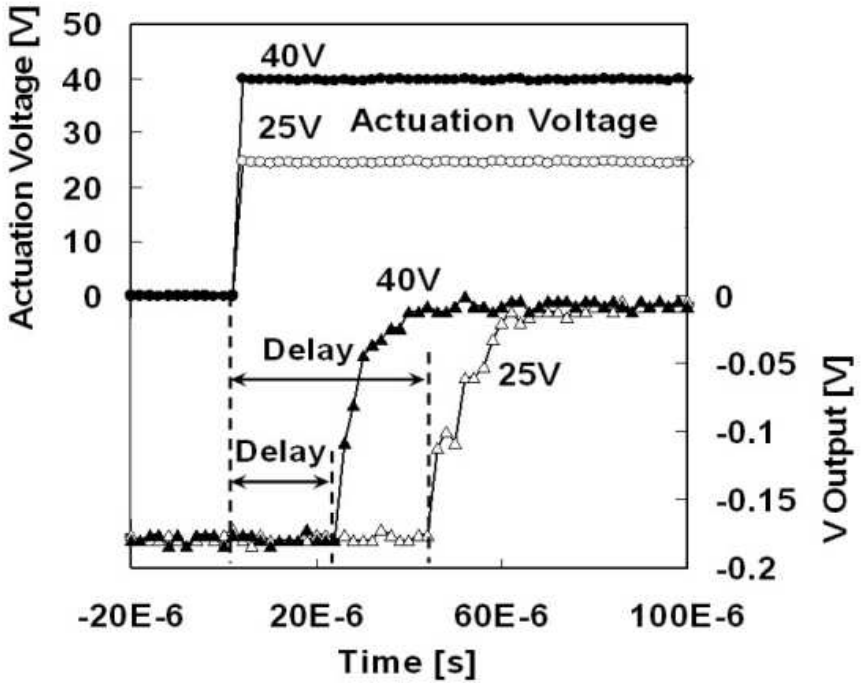

Fig. 3.3: Switch time response of a resistive shunt MEMS for two different actuation voltages of 25 V *and* 40 V.

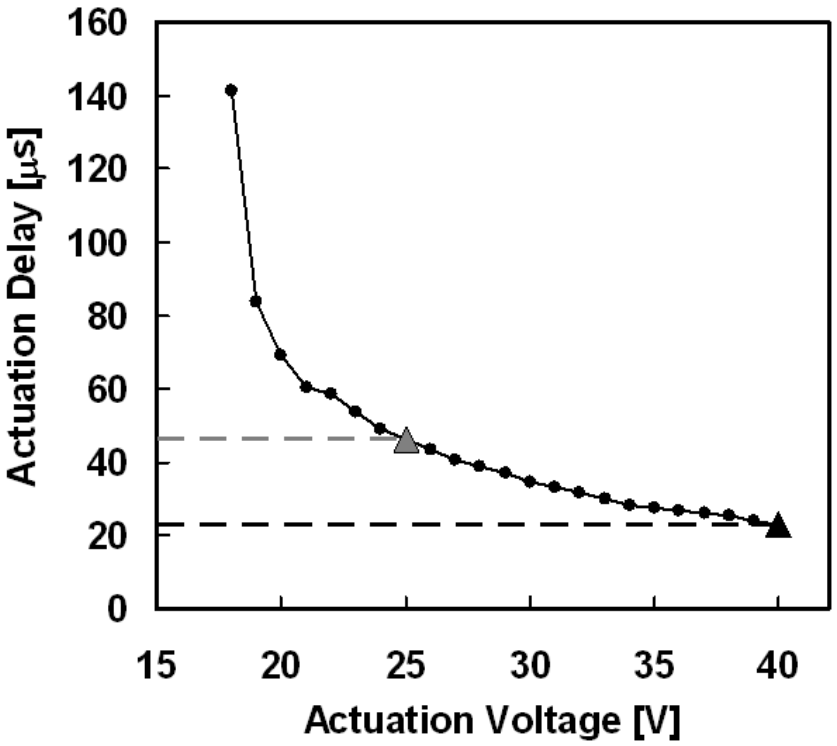

Fig. 3.4: Actuation delay as a function of the polarization voltage.

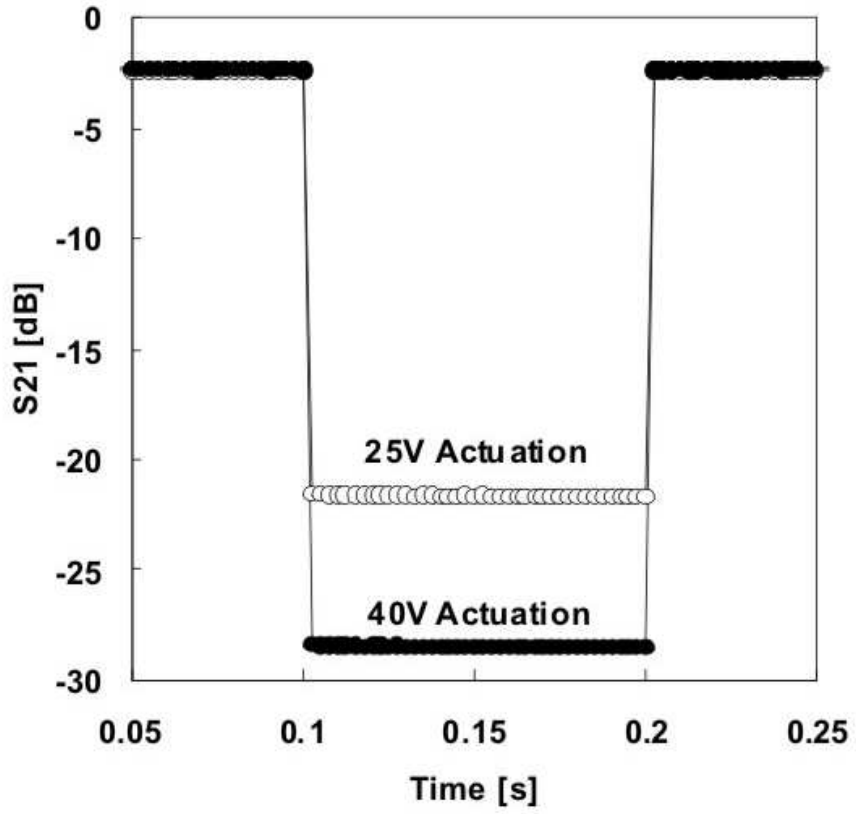

Fig. 3.5: S_{21} Scattering parameter of a resistive shunt MEMS for two different actuation voltages: 25 V *and* 40 V.

3.2 The DC Sweep

The electrical characterization of a RF switch begins with the so called DC-sweep. A typical graph of this measurement is shown in figure 3.7, and consists in biasing the actuation structure of the device with different voltage steps and measuring the corresponding scattering parameters at each step. As indicated in figure 3.7, the measurement starts from 0 V up to the maximum selected voltage (V_{Max}, arrow 1 in figure 3.7), then goes back to 0 V (step 2), then decrease down to $-V_{Max}$ (step 3), and finally comes back to 0 V (step 4).

This way leads to the traditional hysteresis-like diagram reported in figure 3.8. With this measurement it is possible to extract the actuation voltage (V_{Act}) of the device under test, the release voltage (V_{Rel}), the RF performances (S-parameters), and to study the presence of charge trapping or redistribution phenomena.

Although this first analysis is quite common and very powerful, the stress of the device during the DC polarization could be significant, and for this reason, great cure must be taken to avoid misleading results from the electrical and mechanical stress induced by the same measurement process. In particular, the time spent during each step, and the instant in which the S-parameters measurements are performed could affect the measurement results.

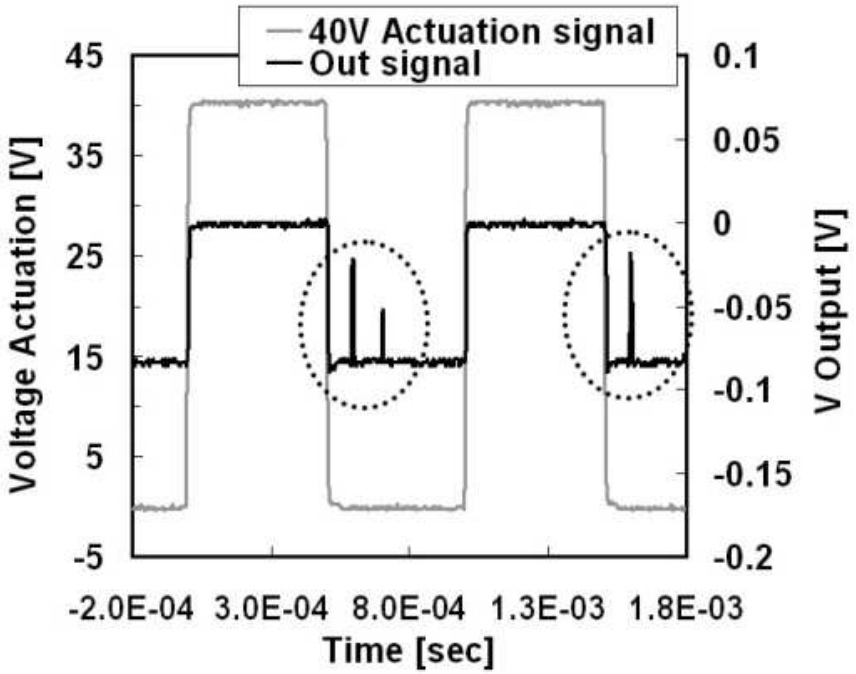

Fig. 3.6: Unexpected bouncing observed when a 40 V *actuation voltage is applied.*

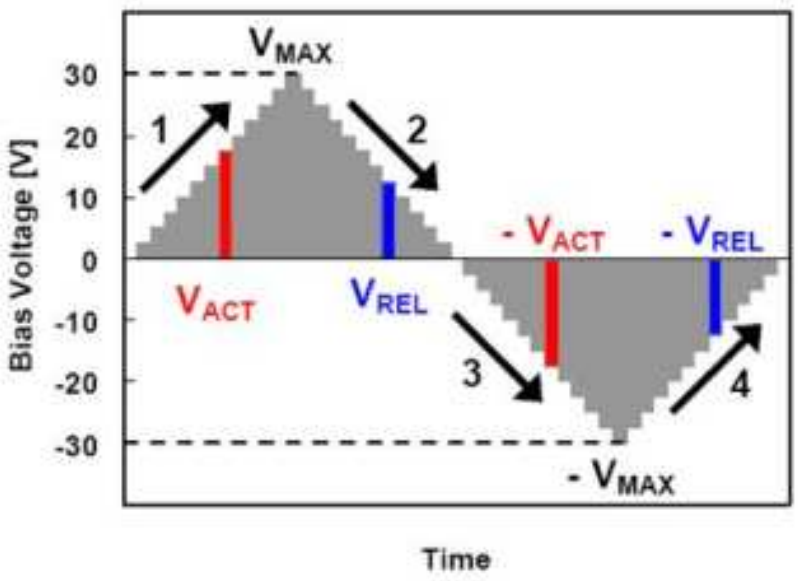

Fig. 3.7: Actuation voltage behavior during a DC sweep characterization.

3.3 The cycling stress

One of the most important factors to evaluate the RF-MEMS switch robustness is the cycling stress. In this test procedure the device is submitted to a series of pulses that actuates and un-actuates the device monitoring the S-Parameter changing. With this reliability procedure it is

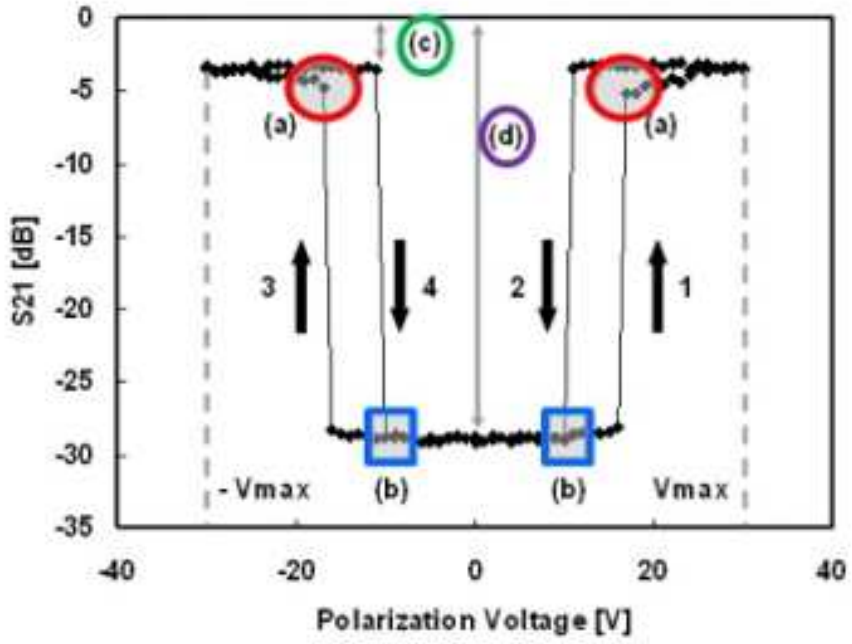

Fig. 3.8: Typical DC-Sweep characteristic that furnishes the fundamental RF-MEMS parameters of a series switch: a) actuation voltage, b) release voltage, c) insertion loss, d) isolation.

also possible to obtain information on charge trapping phenomena and contacts degradation.

To perform the cycling stress two instruments are required: a solid state pulser (HP 8114) and a vector network analyzer (VNA Agilent 8753E). The most accurate way to monitor the device state during the cycling stress would be sampling the S-Parameter during every pulse that bias the device. However this is no possible since the VNA sweep time is too long (in the order of milliseconds) to allow a reasonable high frequency cycling stress. In fact, to have such a detailed stress, a pulse frequency of 10 Hz or less would be the proper choice. A so low frequency would have the effect to extend the time spent for a device stress by a factor 100. To obviate this, we decided to sample the device S-Parameter only after a series of unmonitored cycles. In this way we will have a 1 s VNA sweep that will show in detail the device life state, then a series of unmonitored cycles (10, 100, 1000, 10000 and 50000 which is the limit of the programmable pulses of the HP 8114) and then another slow VNA sweep to appreciate the device S-Parameter changing and so on.

Since the microelectronic devices typically show the highest performance degradation rate in the first life period more than after a long use, a particular attention has been paid to the first part of MEMS devices cycling stress. For this reason the series of unmonitored cycles have been chosen with a kind of logarithmic step:

- 10 series of 10 pulses each one (100 cycles)
- 10 series of 100 pulses each one (1000 cycles)
- 10 series of 1000 pulses each one (10000 cycles)
- 10 series of 10000 pulses each one (100000 cycles)

- 20 series of 50000 pulses each one (1000000 cycles)

for a total of 1111100 cycles. After each series, a device S-Parameters sampling is performed as previously stated. In this way it is easy to observe the device degradation in the first cycles of stress and at the same time have a quick stress when the device is stabilized. In fact, after this logarithmic part, the stress can be carried out with series of 50000 pulses at $1\ \mathrm{kHz}$ very quickly, reaching the desired number of cycles.

3.3.1 The problem of the pulse width

Due to the possible use of the RF-MEMS switches as in switch applications in satellites or, simpler, in mobile phone, a high number of cycles in the device lifetime (at least 10^9 cycles) is strictly required. Such a high number of cycles can require a long time to the instruments to test the device: if the stress is performed with a duty cycle of 25%, and a pulse frequency of $1\ \mathrm{kHz}$ (which means a pulse of $250\ \mu\mathrm{s}$), to perform 1 billion cycles we need 1 million of seconds that would be almost 12 days of continous measuring. If an higher number of cycles has to be reached (10^{10} cycles) for reliability certification, the measurement time will increase dramatically up to 4 months. The obvious solution to this long measurement time is to increase the frequency of the pulses to speed up the stress and rapidly reach the desired number of cycles, but it is necessary to pay attention to the pulse width used to bias the device. In fact, the devices tested have shown actuation time of decades of microseconds (typically $60\ \mu\mathrm{s}$) plus a settling time that can be very different from device to device and that can sensibly improve the RF performances of the switch. As shown in the example reported in figure 3.9, the switch under test shows an improvement in its S_{21} parameter of almost $1.4\ \mathrm{dB}$ in $580\ \mathrm{ms}$ of polarization.

This means that even faster switch could need a longer polarization time than the actuation time only to reach the required S-parameter value. After this consideration, choose to speed up the stress by increasing only the pulses frequency, it could lead to an unrealistic reproduction of the working condition of the device impairing the cycling stress results. For this reason, and also due to the great number of switches tested, all the cycling stress in this work have been performed with a cycling frequency of $1\ \mathrm{kHz}$ and a duty cycle of 25% (pulse width = $250\ \mu\mathrm{s}$).

3.3.2 Choosing the appropriate actuation voltage

Some of the tested devices have shown cycling stress with a fast degradation in the first hundreds of cycles. This fast degradation could be due to a weak actuation force that can pit and hard the metal to metal contact instead of perform a good metallic contact and rapidly increase the contact resistance leading to a no more working device [3]. To avoid this degeneration a solution could be to increase the actuation voltage during the stress. In fact, as has been shown in 3.1 (page 40), the increase of the actuation voltage generally leads to an improvement of the device S-parameters that can guarantee a better cycling stress increasing the switch lifetime at least up to 1 million cycles. An example of such stress behavior is reported in figure 3.10a and figure 3.10b. After a DC sweep characterization, that provides the proper actuation voltage of the device ($12\ \mathrm{V}$, figure 3.10a), the switch has been submitted to a cycling stress with two different actuation voltages: $20\ \mathrm{V}$ and $30\ \mathrm{V}$. As it is possible to see in figure 3.10b, the first

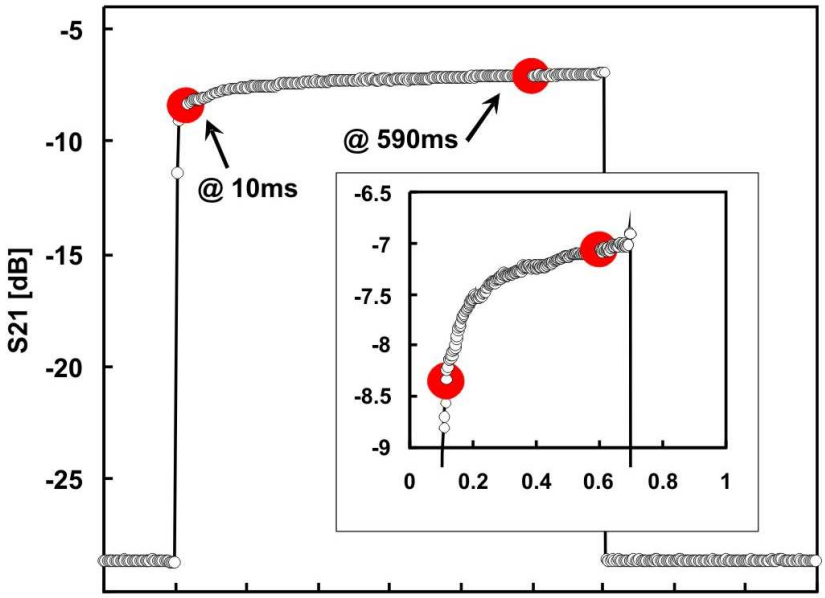

Fig. 3.9: Improving of the switch S-parameter during a $600\ \mathrm{ms}$ *wide pulse.*

stress (@ $20\ \mathrm{V}$) shows a rapid degradation of the S_{21} parameter that leads to an unacceptable switch transmission ratio value after only 300 cycles. On the contrary, the same device stressed with an higher actuation voltage (at $30\ \mathrm{V}$) easily reaches the 1,000,000 cycles milestone and can be driven, with some negative spikes, up to 12,000,000 cycles before it starts to show a critical degradation of the S_{21} parameter.

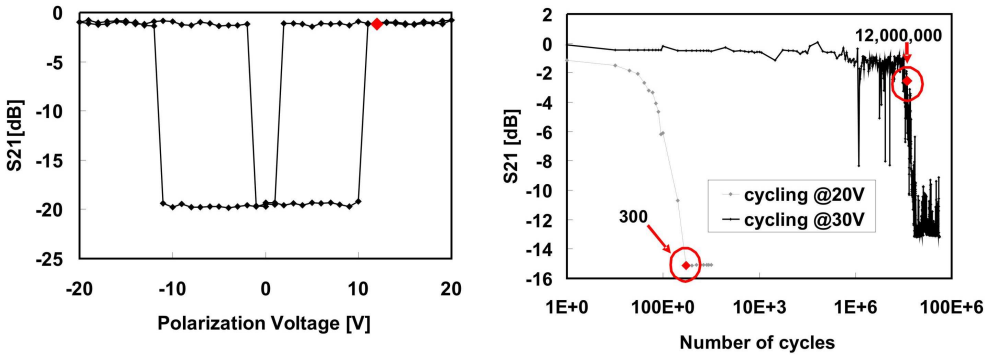

(a) *(b)*

Fig. 3.10: DC sweep and cycling stress of a meander based switch: the red dot in (b) indicates the actuation voltage of the switch ($12\ \mathrm{V}$*), while in (a) it is possible to see the improvement of the* S_{21} *parameter cycling stress due to an higher actuation voltage.*

After this results, a question raises immediately: how can we be sure that this S-parameter degradation is due to the metal-to-metal contact more than a dielectric charging into the oxide under the suspended membrane? To answer this question, a DC sweep measurement has been performed between the different sequences of cycling stress on the same device. In fact, if there will be charge trapped into the oxide under the suspended membrane due to the strong electrical field applied to the device, the DC sweep will show a shifting or a contraction of the switch behavior depending on the charge sign and position into the oxide [17]. In figure 3.11 it is possible to see a device submitted to eight sessions of cycling stress (1, 10, 100, 1000, 10^4, 10^5, 10^6, 10^7 cycles respectively) and tested after every session with a DC sweep.

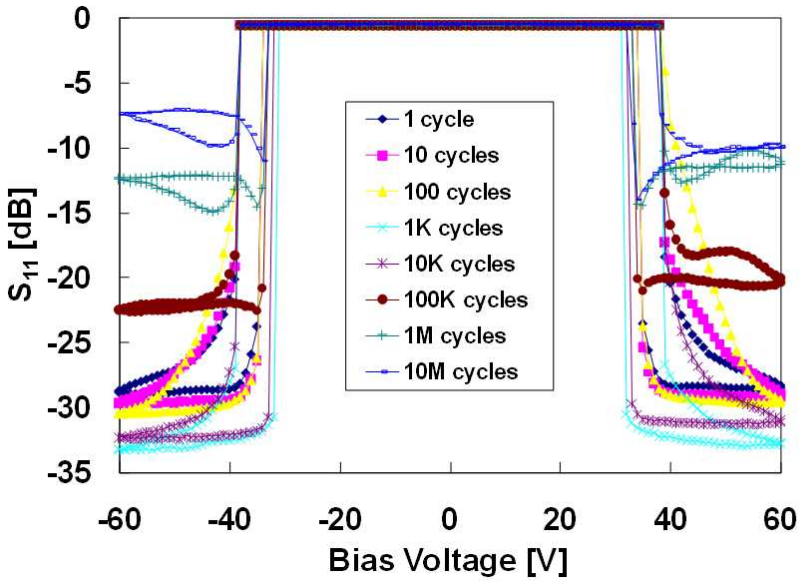

Fig. 3.11: DC sweeps measurements of series switch after every session of cycling stress.

It is easy to note that the device degradation concerns almost only the S-parameter actuated value more than actuation or release voltage (there is only a negligible variation in such parameters). Therefore, only a small amount of charge is trapped into the oxide, while the contact degradation seems to be the main reliability problem of these devices. This confirm that the improving of cycling stress for higher actuation voltage is due to the stronger actuation force which leads to a better adhesion between the metallic surfaces.

Even if the increase of the actuation voltage seems to be the remedy to the contact degradation, it is important to observe that the biasing voltage cannot be increased indefinitely. In fact, a too strong electrical field applied can accelerate in a sensible way the dielectric charging and the mechanical fatigue of the beams leading to a lower robustness to cycling stress. Moreover, bounces have been observed in the switch release transient for higher than nominal actuation voltages. As for the device actuation time (par. 3.1), a trade-off between the nominal actuation voltage and the breakdown one has to be found to guarantee a reliable cycling stress.

3.4 Cycling stress main results

In this section will be presented the main results obtained during the cycling stresses performed on both the PRIN and ESA devices.

3.4.1 Meander beams vs Straight beams MEMS switches

The meander based RF-MEMS switches are characterized by a weak spring restoring force. The multiples bending of the beams that anchor the suspended membrane has the property to reduce the actuation voltage to values down to $10 - 20$ V, which is about two or three time less than the voltage required by the straight beams to actuate. If a weak beam spring constant can bring the benefit of a low actuation voltage that can be easily found in common system application allowing an easy interface of the MEMS device with the commercial electronic, on the other side it leads to a not very efficient device in terms of DC characterization and cycling stress. Moreover, the benefit of a low actuation voltage can be compromised by the cycling that clearly shows how an higher than expected voltage is required to proper actuate the device. As examples, a series of DC sweep characterization with the related cycling stress of meander based switches is reported in figure 3.12.

The first switch presented (with Conho dimples contacts, see par. 1.3 page 9) shows a quite good DC sweep characterization (figure 3.12a) with a regular behavior and a clear actuation at 11 V. The insertion losses (the S_{21} parameter of the actuated device) are about -2 dB due to unwanted oxide grown over vias, a process problem now solved. The cycling stress, presented at three different voltages (figure 3.12b), shows a rapid degeneration if performed at 20 V (some hundreds of cycles for a -3 dB loss), whereas can reach more than 10^6 cycles if performed at 30 V. The cycling at 40 V last for only 10^3 cycles before the device stiction, according to what stated before.

The second switch (with Poly dimples contacts, see par. 1.3 page 9) has the same topology of the previous one, but a different type of dimples. The DC characterization is quite irregular and stair like (figure 3.12c), showing a first actuation at 10 V, a second one at 16 V and the last one at 24 V. The cycling stress, presented at three different voltages, shows a rapid degeneration if performed at the first actuation voltage, 10 V (some hundreds of cycles for a -3 dB loss), a better behavior if performed at 20 V and a short and fatal stress for an actuation of 30 V(figure 3.12d). Even if this device respects the paradigm of "higher the actuation, better the stress", the results obtained are totally unsatisfying in terms of number of cycles performed. Since the only different between these two switch is the dimple height and robustness, this could be a first guideline for the design of a better layout to use to manufacture the dimples. In fact, it seems that the Conho dimples are more resistant to cycling stress and also provide a more regular and repeatable DC characterization, which is one of the most important factor, for almost every kind of stresses use such characterization to compare the device behavior changing before and after the stress.

The third switch is again a Poly dimple contact device but with a different meander topology. The DC characterization is more smoothed than the previous device (figure 3.12e), but it is still possible to see at least two different actuation steps (at 10 V and 20 V). Moreover, the S_{21}

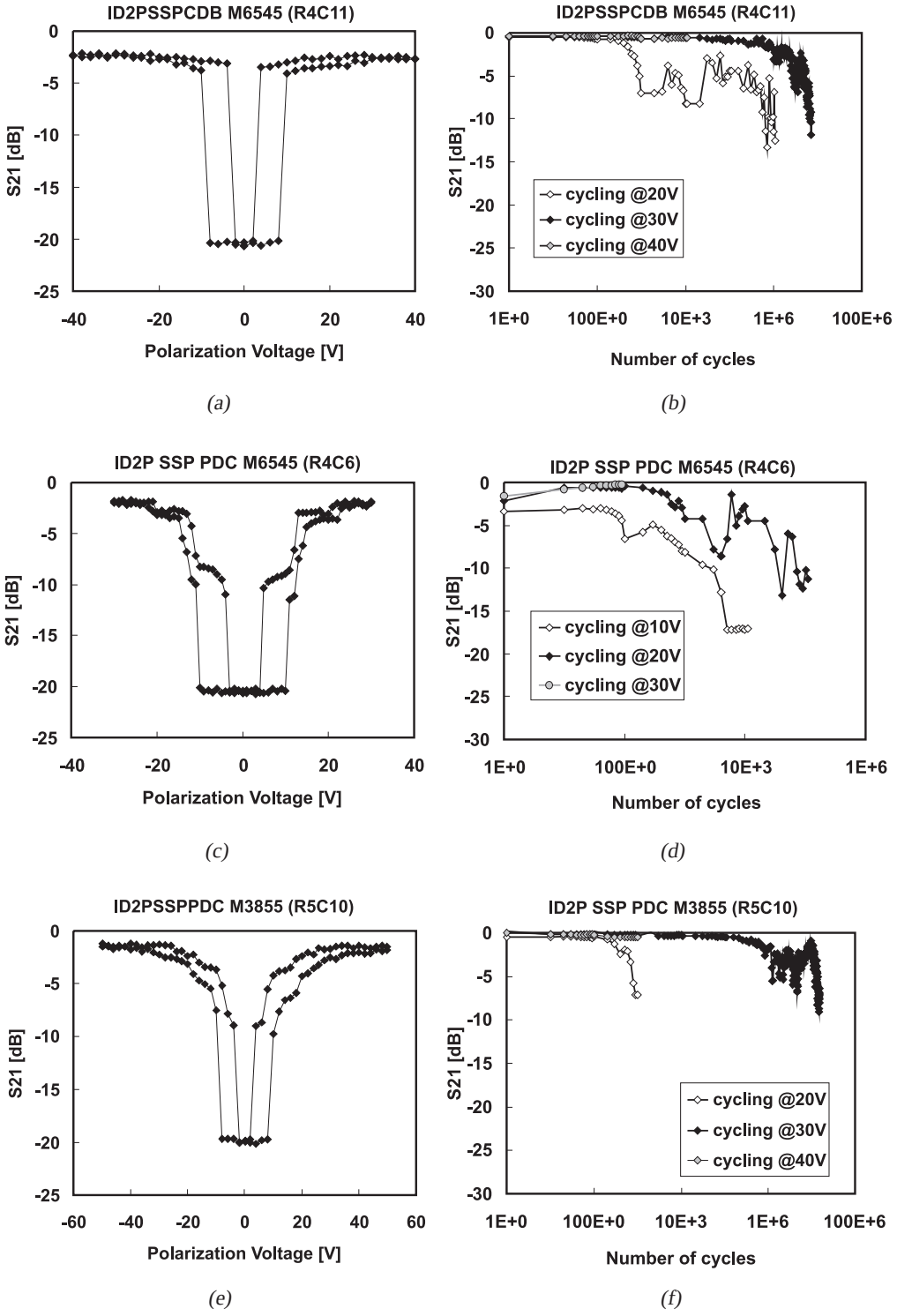

Fig. 3.12: DC characterization and cycling stress of three different meander based ohmic switches.

value continuously improves up to -1.5 dB at 50 V, indicating that a strong force is required to achieve a good metal-to-metal contact. The cycling stress, presented at three different voltages (figure 3.12f), shows a rapid degeneration if performed at 20 V (some hundreds of cycles

for a -3 dB loss), while can reach more than 10^6 cycles if performed at 30 V. The cycling at 40 V last for only some hundreds of cycles before the device stiction. On the contrary of the previous switch based on Poly dimples, this device has shown a very good and lasting cycling stress if actuated with the proper voltage (30 V). This could suggest that a different topology of the device can partially compensate the contact force problem.

It is interesting to note that there is a quite good correspondence between the switch cycling stress behavior and the so called Wöhler curve, which has the property to statistically describe the number of load cycles that a mechanical device can tolerate before breaking. This should not surprise since the device under test is, in the end, a suspended metallic beam with the purpose to cycling around the rest position. However, it is important to underline how a classical macro-scale test measurement can be valid and usable also on micro-scale devices.

The straight beams switches are characterized by a strong spring constant and required quite high bias voltages to actuate ($30 - 50$ V). These switches typically exhibit a clear actuation (one step only) and a good robustness to cycling stress. In figure 3.13 is reported a series of DC sweep characterization of straight beam based switches with the related cycling stress.

The first switch (figure 3.13a) is a Conho dimple contact ohmic series switch. It presents an excellent DC characterization with a clear actuation at 32 V, -0.8 dB of insertion losses and an acceptable isolation (-19 dB at 6 GHz). Even the cycling stress (figure 3.13b), performed at 40 V, shows a stable behavior that easily reaches the million cycles milestone and can be driven up to dozens of millions of cycles before to show a sensible contact degradation. It is important to note that, for straight beam devices, usually there is no necessity to sensibly increase the actuation voltage to obtain a more lasting cycling stress.

The second switch presented is topologically the same of the previous one but, instead of Conho dimples, it has been manufactured with Poly dimples contacts. The DC characterization (figure 3.13c) is quite good and very similar to the Conho switch one, but the cycling stress (figure 3.13d) present an incredible weakness, with a stuck device after only 10^3 cycles. Even if this is a particularly negative example of Poly dimple switch cycling stress and of course there have been similar devices that have shown better cycling performances, nevertheless this is a result that draws another point in that tendency line which seems to indicate the Poly dimples contacts as a less efficient solution compared to the Conho dimples contacts.

The last presented switch, is a straight beam device with normal flat contact. The meander topology is the same for the three presented switches, only the contacts types change. This device has shown a good DC characterization (figure 3.13e) with a clear actuation and stable S-parameters during the actuation. The RF performances are a little worst compared to the ones of the dimpled switches (-1.6 dB of insertion loss and -15 dB of isolation) but the cycling stress (figure 3.13f) is quite good almost up to 1 million cycles, which is definitely better of the cycling stress exhibited by the Poly dimple device. After these considerations on meander and straight beams based switches, it seems to be clear that the most promising devices, from a reliability point of view, are the straight beams switches with Conho dimples. The necessity to use an higher of expected voltage during the cycling stress to obtain a more reliable device, can be explained considering the DC sweep of the two typologies of devices. The pressure of the suspended membrane on the metallic contacts, when the switch is actuated, is generated by the electrical field between the actuation structure under the bridge and the bridge itself.

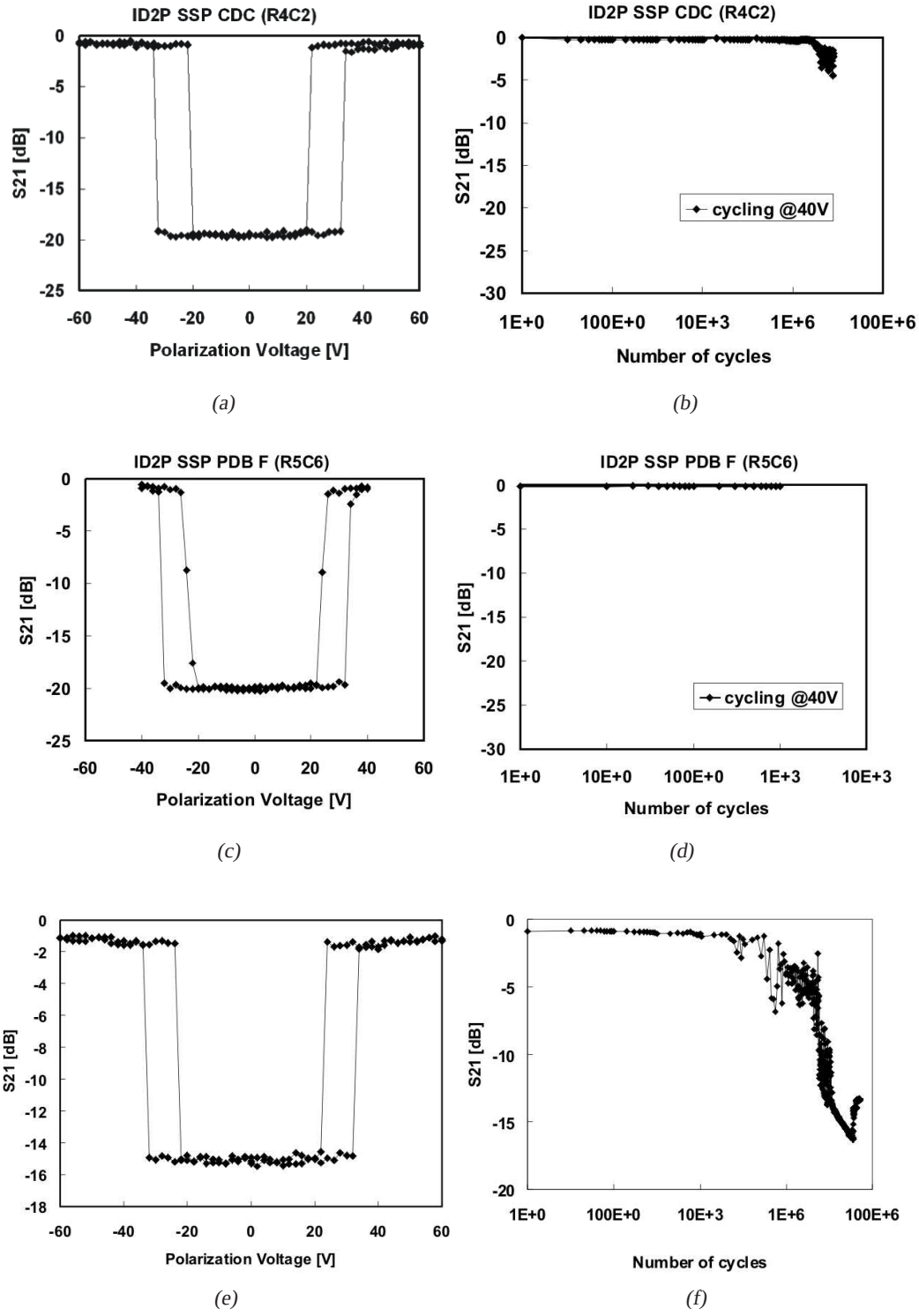

Fig. 3.13: DC characterization and cycling stress of three different straight beams based ohmic switches.

Due to the mechanical law that rules the MEMS actuation (par. 1.1, page 3), a part of this force is used to compensate the spring restoring force and maintain the bridge down while the remaining force is balanced by the metal contacts. Therefore, since the release voltage (V_{Rel})

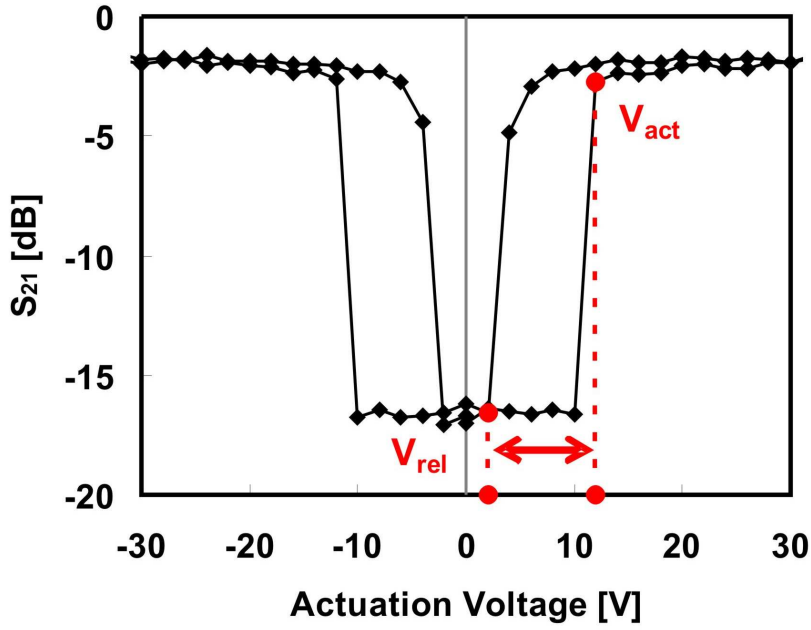

(a)

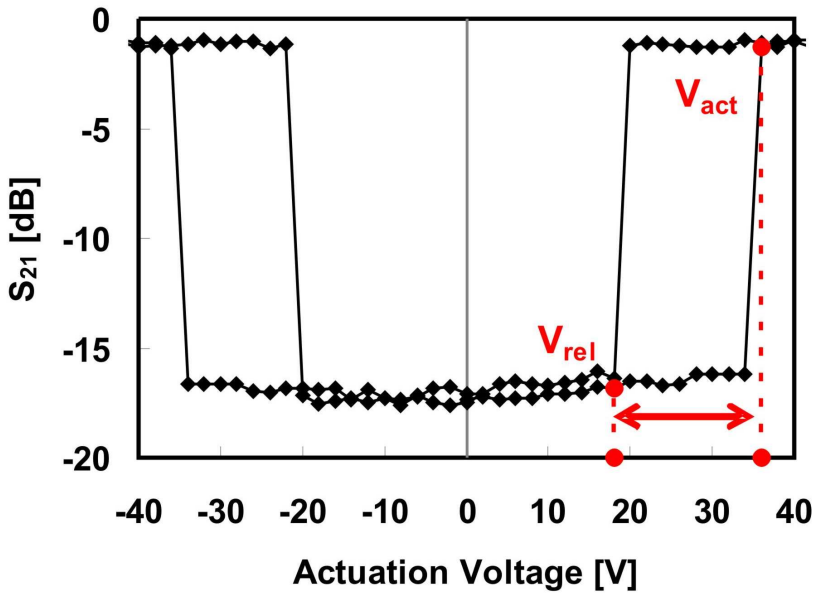

(b)

Fig. 3.14: Compare between the hysteresis of a meander and a straight beams based switches.

is a physical device parameter that cannot be influenced during measurements, the increasing of the actuation voltage (V_{Act}) will directly increase the contact force. If the actuation voltage used to test the device is the nominal one, i.e. the lower tension necessary to bend down the bridge and achieved a contact with the transmission line, the pressure on the contact depends directly on the width of the device DC sweep hysteresis: a thin hysteresis will lead to a small difference between V_{Act} and V_{Rel} and to a consequentially low contact force, while a wide hysteresis will indicate a strong contact force. The trivial solution to obviate a thin DC sweep hysteresis is to work at higher than the nominal actuation voltage.

In figure 3.14 are presented the DC sweeps of a meander (figure 3.14a) and a straight beams (figure 3.14b) device. For the meander switch, V_{Act} is 12 V and V_{Rel} is 2 V which results in 10 V of electrostatic force on the contacts. The straight beam switch on the contrary, shows a 36 V V_{Act} and a 18 V V_{Rel}, with 18 V of electrostatic force distributed on the contacts. It is almost the double of the meander switch. This explain why a straight beam switch can be cycled at an actuation voltage near the nominal one (cycling stress at 40 V, V_{Act} + 10%), whereas a meander based switch require an higher than the nominal tension (cycling stress at 30 V, V_{Act} + 150%) to show an acceptable cycling stress. Even if the devices have been stressed at two different voltages (30 and 40 V), the difference between the stress voltage and the release voltage is the same (18 V).

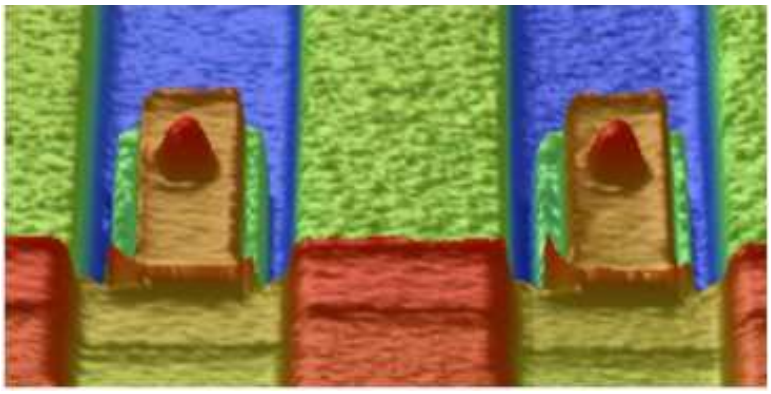

(a)

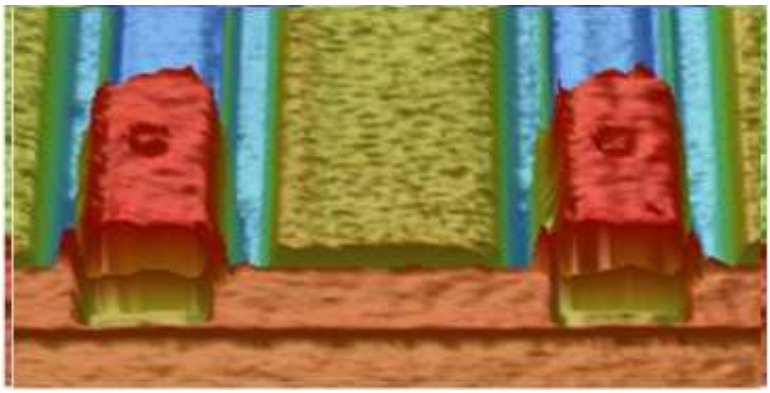

(b)

Fig. 3.15: Dimple structures before (a) and after (b) cycling stress: the impact of the suspended membrane has pushed the dimple inside the contact probably vanishing its beneficial properties for the device series resistance.

Regarding the dimples technology, it is not yet well understood if this solution leads to a real improvement in the cycling stress, since, due to a large number of different devices tested, the statistic correlation between switches with or without dimples is quite poor. An investigation, conducted by means of an optical profilometer, has underlined how the dimple structure can be damaged by the cycling stress. In figure 3.15 it is shown a comparison between a dimpled switch before and after a cycling stress. It seems that the repeated impacts of the suspended membrane due to cycling stress have yield the dimple, compressing the polisilicon (Poly dimple) or the oxide (Conho dimple) structure that is inside the metallic cone. It is questionable if after such a damage the dimple structure is still working in some way or if the contact is now equivalent to a flat one. On the contrary, a flat contact, submitted to a severe stress (50 * 10^6 cycles) has shown no sign of degradation during the optical profilometer analysis which suggests that the main failure mechanism for long lasting cycling stress is dielectric charging (typically stiction or, in some cases, screening and a consequentially missed actuation).

3.4.2 Series ohmic winged switch stopping pillars (PSX)

Three different kinds of stopping pillars series ohmic winged switch have been submitted to cycling stress: PSX1, PSX2, PSX5 (par. 1.4, page 12). In figure 3.16 are reported the DC characterizations and the cycling stresses of the three switch topologies.

All the PSX devices have shown a very good DC behavior with a clear actuation and stable S-parameter during the actuation and an actuation voltage of $46\ \mathrm{V}$. Also the cycling stress has been carried out up to 10^6 cycles by all the devices without relevant problems. However the PSX5 devices have shown a better stability in the S-parameter during the stress becoming more suitable than the other two variations from the reliability point of view. The PSX5 device is characterized, like the PSX2, by $1180\ \mathrm{nm}$ tall stopping pillars divided in multiple-block, while the PSX1 has the stopping pillars of the same height, but divided in thicker blocks.

3.4.3 Boosted ohmic shunt switch (BO)

Only one variation of the boosted ohmic shunt switch (the BO5) has been tested. The cycling stress has typically induced an heavy contact degradation, mixed with dielectric charging issues, leading to an increase of the switch actuation voltage. The switch has shown good RF-performances up to 300,000 cycles, followed by a quick degradation of S-Parameters leading to a no more working device.

As shown in figure 3.17 (DC characterizations before and after the cycling stress), the S-Parameter degradation is due to the increase of the bias voltage needed to obtain good S-parameters values, probably due to a degradation of the metal-to-metal contact, but also to some charge trapping phenomena (asymmetric DC measurement, figure 3.17b). The repetition of the DC characterization after the cycling stress has improved the switch performances and has also partially regenerated the device (figure 3.17b), whereas, after the second repetition, the S_{21} value change from $-1.54\ \mathrm{dB}$ to $-9.21\ \mathrm{dB}$ at $50\ \mathrm{V}$. As already found in other RF-switches, we have seen that higher bias voltages during the cycling stress can improve the device robustness to cycling. This behavior is reported in figure 3.18, where the same device,

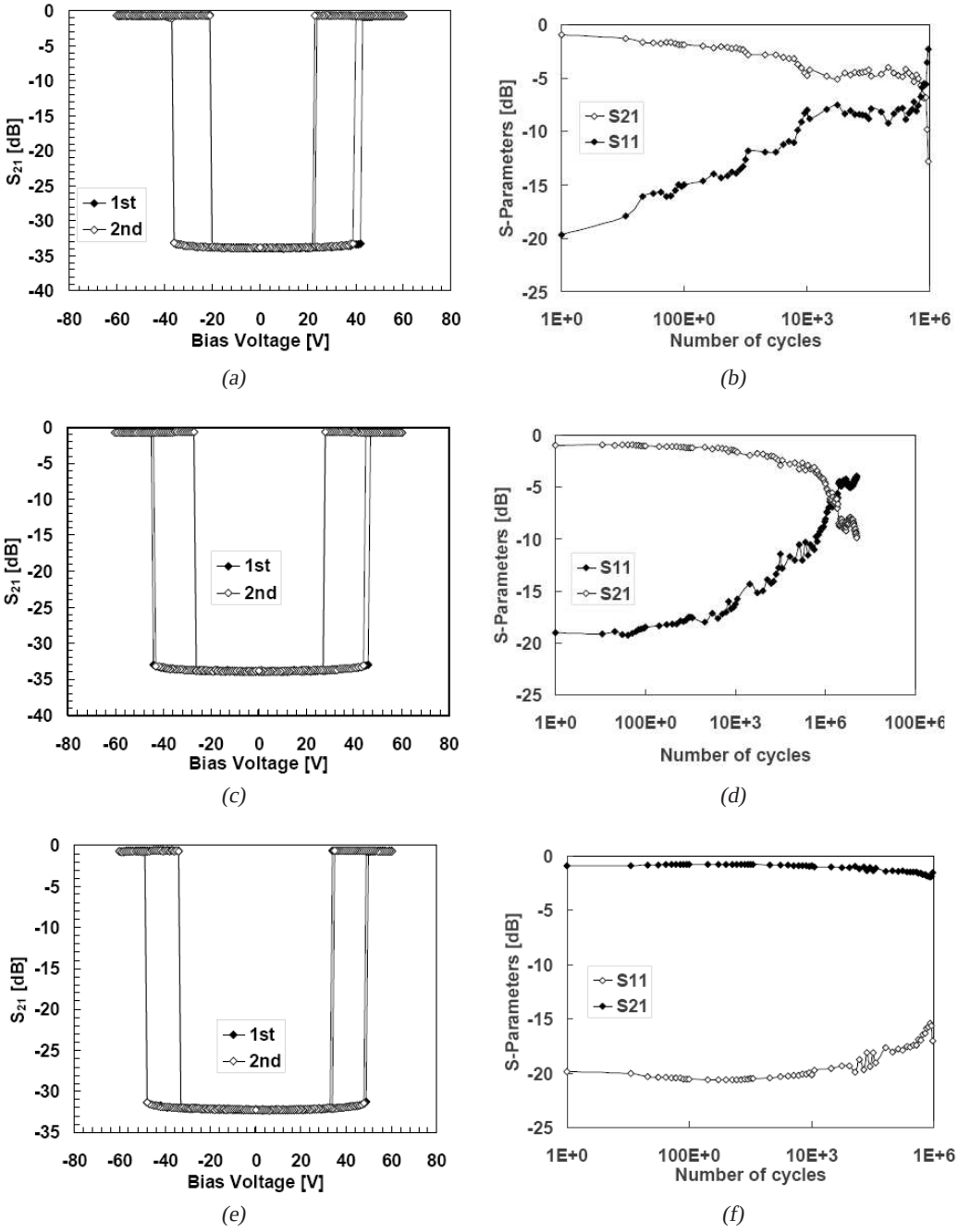

*Fig. 3.16: DC characterization and cycling stress of three kind of series ohmic winged switch stopping pillars (PSX): PSX1 (a) (*1180 nm *stopping pillar mono-block), PSX2 (c) (*1180 nm *stopping pillar multiple-block), PSX5 (*1180 nm *stopping pillar multiple-block) (e)*

actuated at 40 V reaches around 10^3 cycles, at 50 V reaches almost 10^6 cycles, and actuated at 60 V overcomes the million cycles without any sensible S-parameters degradation.

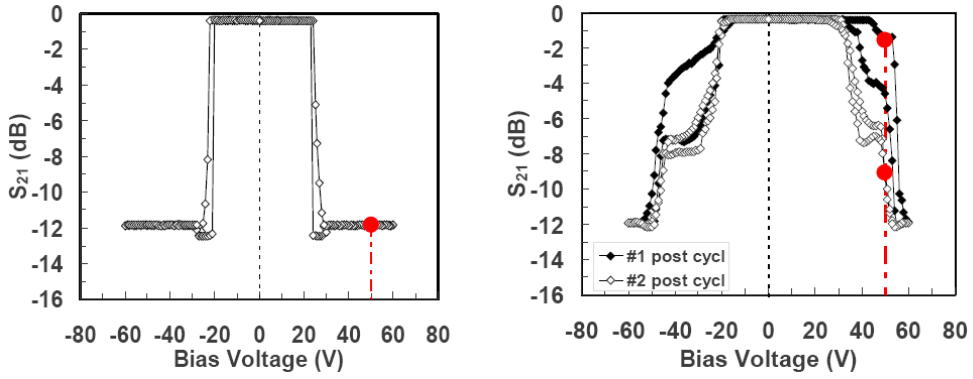

(a) *(b)*

Fig. 3.17: DC characterization of a boosted ohmic shunt switch of a fresh device (a) and after the cycling stress conducted at 40 V *(b). The repetition of the DC sweep seems to regenerate the contacts and to help the charge de-trapping from oxide.*

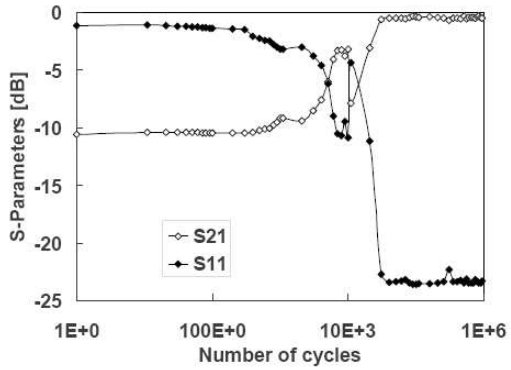

(a)

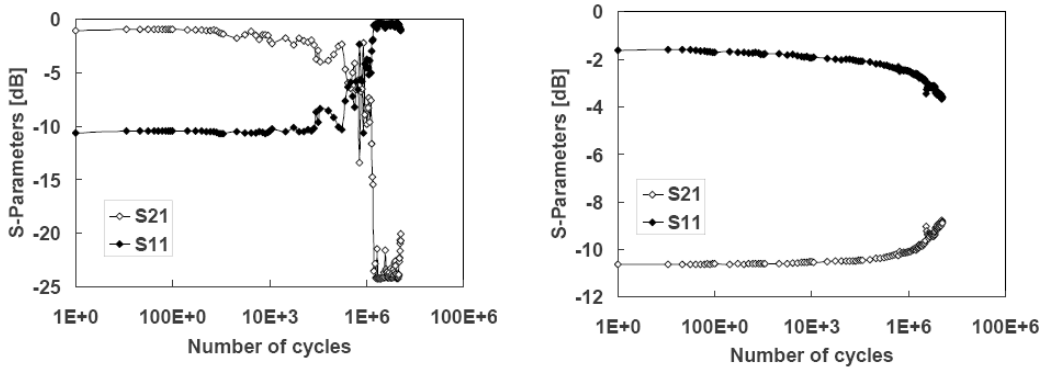

(b) *(c)*

Fig. 3.18: Boosted ohmic shunt switch (BO) cycling stress at different biasing condition: at 40 V *(a), at* 50 V *(b) and at* 60 V *(c)*

3.4.4 Spring anchor ohmic switch (BAT)

The spring anchor ohmic switch (BAT) tested has shown a two steps actuation DC sweep (figure 3.19a) and a very poor cycling stress (figure 3.19b) that lead to the S-parameters values

crossing after few hundreds of cycles. This is probably due to the weak restoring force of the anchored beams which makes this kind of switch very similar to the meander based devices designed by the University of Bologna. In fact, as the meander devices, it exhibits a small hysteresis in the DC characterization that is symptom of weak metal to metal contact. Cycling stress conducted at higher voltage have lead to the device stiction.

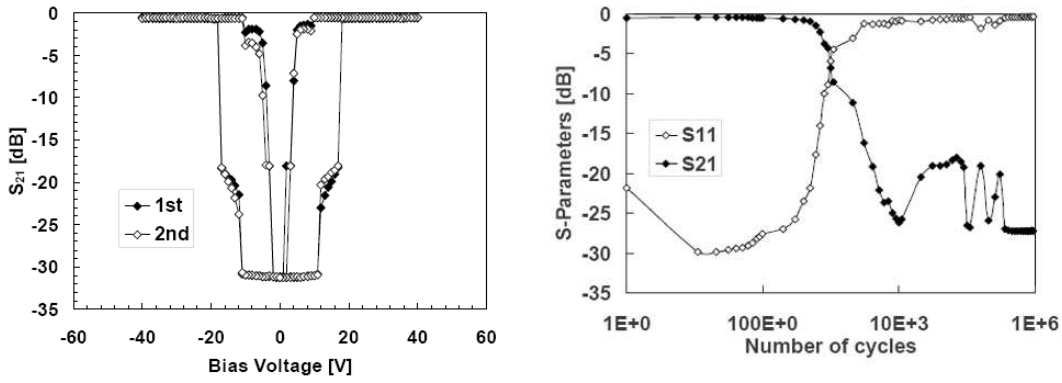

(a) *(b)*

Fig. 3.19: Spring anchor ohmic switch (BAT) DC characterization (a) and cycling stress (b)

3.4.5 Cantilever switch (CA)

The cantilever switches tested (the CA2 variation), has shown a very good dc sweep (figure 3.20a) and an excellent cycling stress (figure 3.20b) making it one of the most promising switches from the reliability point of view. Again, the strong restoring force and a wide difference between the actuation and the release voltage has lead to a more reliable device, that can reach millions of cycles without a sensible degradation in the S-parameters values. The possibility to manufacture the cantilever switch without any dielectric beneath the bridge and with the stopping pillars technology could lead to very interesting device from the reliability point of view.

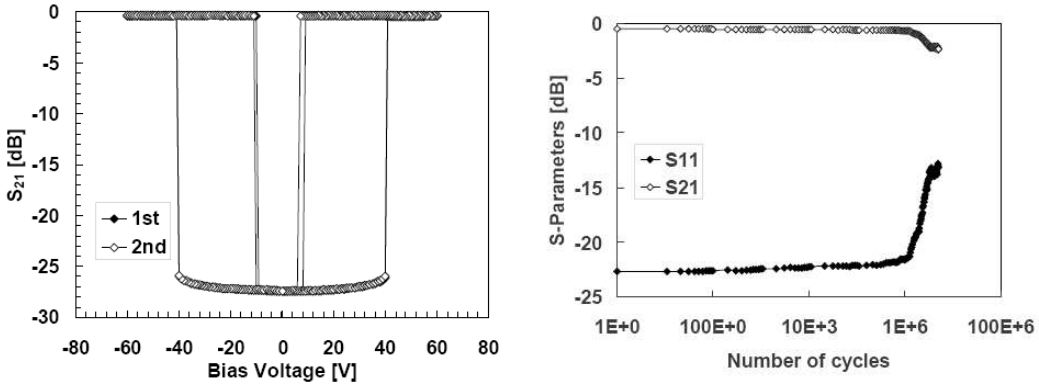

(a) *(b)*

Fig. 3.20: Cantilever switch (CA2) DC characterization (a) and cycling stress (b) at 60 V.

Chapter 4

The long term actuation stress

Although micro-machined RF-switches are attracting acceptance throughout the world, the reliability of such devices is typically studied only in terms of RF performances and cycling, overlooking other reliability problems. Even if lifetimes of the order of billions cycles have been achieved for metal-to-metal contact switches, long-term reliability of these devices is still an open question, since stable performance under a range of operational and environmental stresses has not been demonstrated yet.

Furthermore, research efforts are mainly dedicated to capacitive switches, neglecting the study of the reliability of ohmic switches necessary to build efficient wide-band systems for lower frequency applications. Ohmic switches, characterized by the electrical contact of two metallic surfaces, can also be impaired by stability problems due to changes in ohmic contact resistance (par. 3.4, page 48). The causes can be diverse, such as surface contamination, material transfer and erosion, and surface changes due to absorption or oxidation. Other contact issues such as micro-welding, caused by excessive contact heating, could heavily impact the ability of the switch to return in its rest position (deactivation). Besides defining the electrical characteristic of the device (actuation voltage), the mechanical properties (spring constant) of the suspensions could also play an important role on the reliability of the device if the springs are not able to pull up the membrane in its rest position.

4.1 The Long Term Actuation stress (LTA)

The reliability of micro-machined RF-switches is analyzed in literature mainly in terms of the robustness to cycling stress [30, 36]. Most of the devices studied are capacitive RF-MEMS devices used for systems with a high switching rate (rx/tx antenna switches). Moreover, state of the art capacitive switches do not suffer from contact degradation issues. The most impairing reliability issues in capacitive RF-MEMS switches are due to dielectric charging leading to stiction or screening effect problems. However, there are other applications based on the certainty of actuation / de-actuation, more than the total number of actuations required, in which MEMS devices are being considered as potential candidates to substitute traditional solid state / mechanical devices. Researchers attention is currently moving to the possibility of using RF-MEMS devices as light and small redundancy switches in satellite applications. In such

circuits, when a failure occurs in the main section, the redundancy switch must be able to disconnect it and connect the redundant circuit in a short time, and in some applications the switching time requirement could be low as one second even after several years of working. It is straightforward that for such devices, cycling stress studies become less important whereas other reliability issues must be analyzed. The Long Term Actuation stress (LTA) has the aim to investigate the behavior of RF-switches under continuous polarization, focusing on the S-parameters evolution during both actuation and release phases, and, in particular, on the time the switch spends to return to the up-state position [37]. An ad-hoc semi-automatic measurement and stress setup has been developed, with selectable values of RF power, applied voltage during the stress (V_{Bias}), and time spent in the actuated state.

4.1.1 Release evolution of meander-based switches

Meander based switches (designed by University od Bologna) have been submitted to several sessions of continuous polarization stress to monitor the release phase transient. Typically, these devices have exhibited consistent delays respect to the nominal time that this kind of switches need to return in the rest position. The un-actuation time of a meander based device is meanly similar to the actuation time (50 to 100 μs, depending on the meander shape). The measured delays for these devices can be of some minutes (after few hours of continuous polarization, i.e. 2 or 3 hours) or hours for longer stress. In figure 4.1 it is shown the S_{21} parameter evolution of a series meander based switch submitted to a four hour stress at V_{BIas} = 40 V. During the first hour of actuation the insertion losses slightly decreases (from 1.6 dB up to 0.5 dB), probably due to the metal-to-metal contact improvement described in chapter 3. However, the extended intimate contact could be the origin of the release delay problem: the switches take around 1 h to completely release itself since V_{Bias} = 0 V.

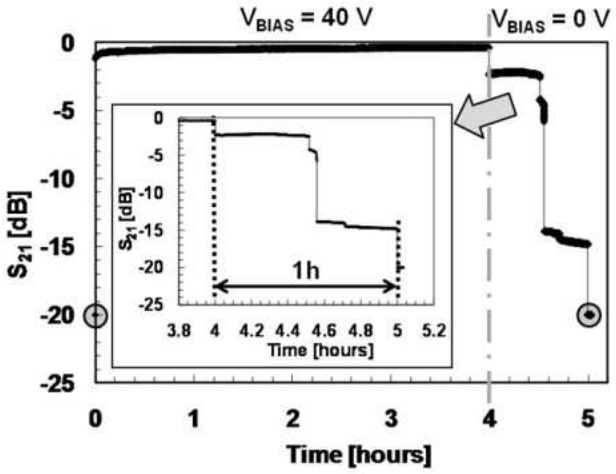

Fig. 4.1: Meander based series switch. The device takes around 1 h *to release itself.* T_{Act} = 4 h, V_{Bias} = 40 V, P_{RF} = 0 dB. *The inset shows a magnification of the release phase. The un-actuation starting point and the final one are highlighted.*

Analyzing the release phase, the S_{21} parameter does not show a sudden release, but a step-like evolution. This non-uniform pull-up of the suspended bridge during the release transient

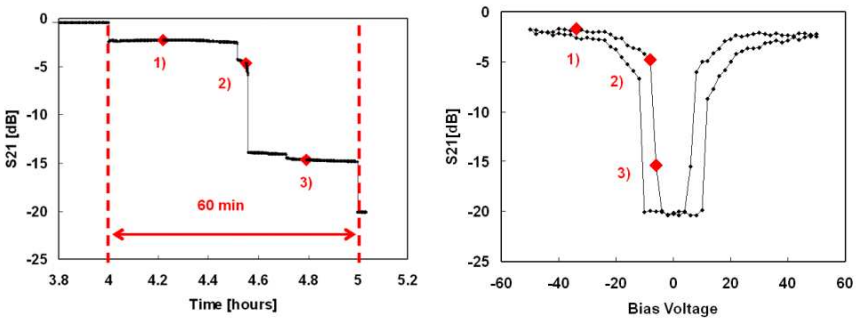

(a) *(b)*

Fig. 4.2: Comparison between release transient (a) and DC characterization (b) of an ohmic series meander based switch.

could indicate a progressive detachment of different sectors of the bridge from the bottom contact points.

Comparing the release transient with the DC characterization (figure 4.2) it is possible to note a good correspondence with the long term stress release step and the DC releasing behavior. The device retraces the DC sweep releasing path, step by step. This phenomenon could be explained by micro-welding and dielectric charging issues generated during the long actuation period with RF signal applied. A detailed description of the behavior of metal-to-metal contact and micro-welding is reported in [38]. Furthermore, meander shaped suspensions, characterized by a low restoring force, are not able to detach the stuck membrane and bring the bridge back in its rest position. In order to better characterize the release time, the same stress has been performed varying actuation periods and applied RF power level. In figure 4.3 the release time is reported as a function of the actuation period. It is clear that long actuation periods lead to long release times, reaching around 110 minutes after 60 hours of continuous polarization. Such behavior makes this family of devices (low spring constant) not suitable for the development of a reliable redundancy switch.

The graph in figure 4.4 shows the evolution of the release time of a meander based shunt switch stressed for 4 hours at different power levels of -10 dBm, 0 dBm, and 10 dBm (V_{Bias} = 40 V). It is interesting to note that, as the RF power increases, the release time decreases. This behavior could be explained with a local temperature increase of the device (just upon the SiO_2 dielectric layer between the actuation layer and the metal-metal contact), that can make charge recombination mechanisms faster, leading to a reduction of charge trapping phenomena. This change could also make the switch less sensitive to capillary effects, and micro-welding problems.

4.1.2 Release evolution of straight beams based switches

Also straight beams switches have been subjected to a long term actuation stress (72 h long actuation stress (P_{RF} = 0 dBm)). Compared to meander based devices, the stronger spring constant of the straight beam based switches, results in devices suddenly releasing themselves (after 72 h long actuation stress), as depicted in figure 4.5.

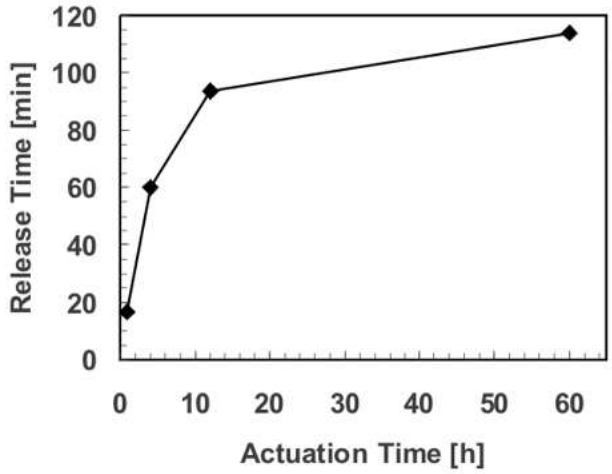

*Fig. 4.3: Release time evolution as a function of the actuation time stress (V_{Bias} = 40 V, P_{RF} = 0 dB*m*).*

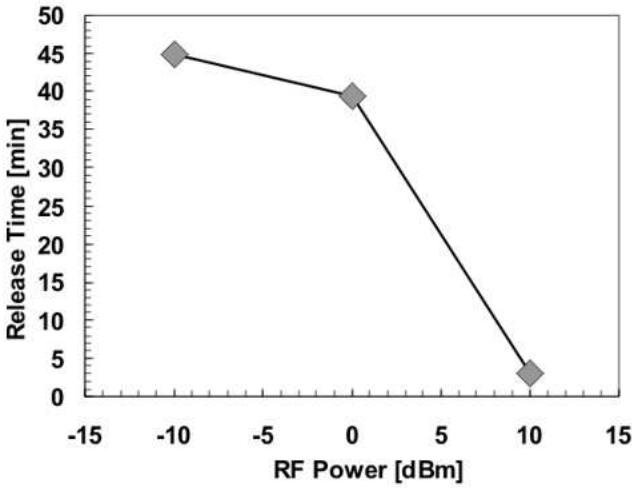

Fig. 4.4: Release time evolution of a meander based device as a function of the applied RF power. T_{Act} = 4 h, V_{Bias} = 40 V

Concerning environment issues, we have found that high percent relative humidity (%RH) can change the release time of the same device under the same stress condition, dramatically increasing from around $2\ \mathrm{min}$ to beyond $80\ \mathrm{min}$. An excessive increase in local environment temperature can equally influence the reliability of these devices. Temperatures high enough to induce spring softening, will make the release time of RF-MEMS switches longer than at ambient temperature. The environmental impact on the release phase of RF-switches is currently under investigation.

4.2 Bounces

As previously reported in [35], electrostatically actuated RF-MEMS switches could suffer from unexpected bounces, hundreds of microseconds after the bias voltage has been turned off. In

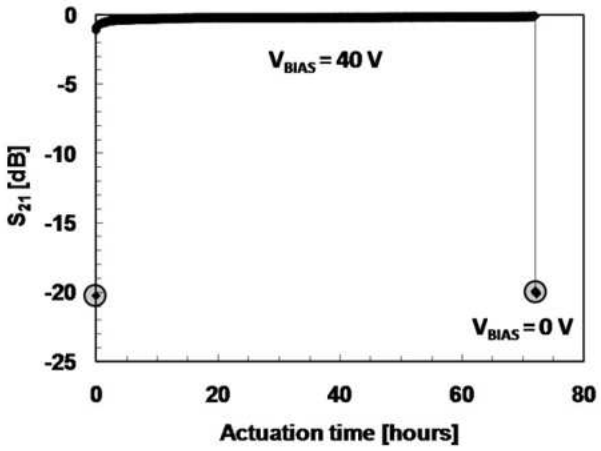

Fig. 4.5: The straight beams device submitted to the LTA stress suddenly release itself when bias with 0 V *after* 72 h *at* 40 V*.*

order to better characterize this behavior, we have repeated the experiment using RF-switches with meander and straight beams suspensions and two different thickness of the suspended membrane (1 μm, and 3 μm). Results confirm previous data and a relationship between the bounces delay and the mechanical geometry of the movable structure has been observed.

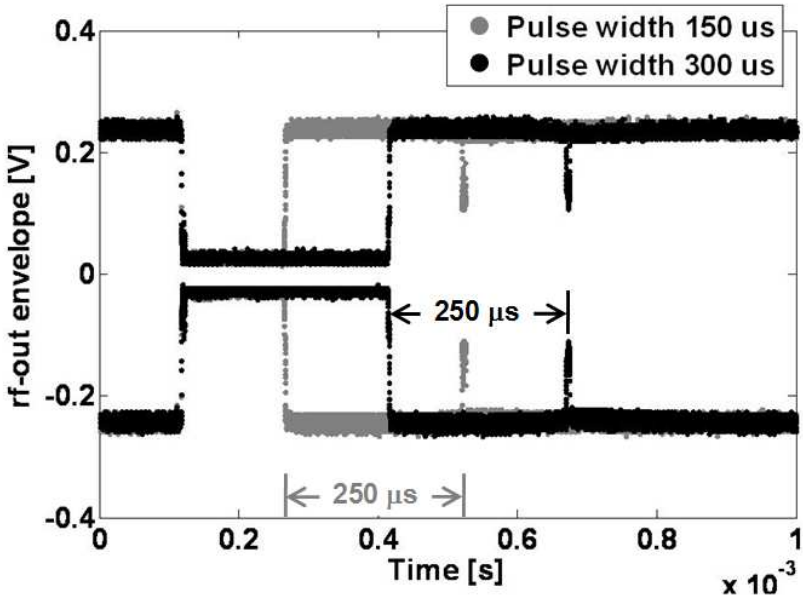

Fig. 4.6: Bounce on meander based shunt switch with 3 μm *thick suspended membrane. The bounce delay (*250 μm*) is not pulse width dependent.*

The measurement setup is based on an RF-signal generator (Agilent 8753E VNA internal RF generator), a solid state pulser HP 8114A for device biasing, and a Tektronix TDS6804B DSO to measure the envelope of the output signal. The bounces characterization of meander based shunt ohmic switch with 3 μm thick membrane is shown in figure 4.6. One bounce appears 250 μm after the bias voltage has been turned off.

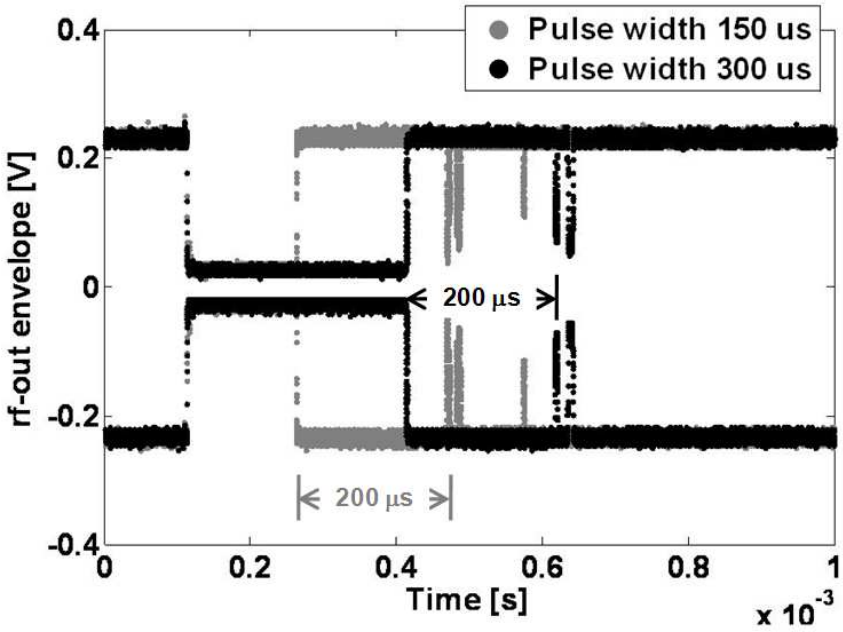

Fig. 4.7: Bounce on meander based shunt switch with $1\ \mu\mathrm{m}$ *thick suspended membrane. The bounce delay (*$250\ \mu\mathrm{m}$*) is not pulse width dependent.*

The bounce presence and delay is not bias pulse width dependent as shown in figure 4.6, for two bias pulse widths of $150\ \mu\mathrm{s}$ and $300\ \mu\mathrm{s}$. A similar behavior has been shown by thin membrane devices, as reported in figure 4.7. In this case, more bounces appear after the bias voltage has been turned off, with the first appearing after $200\ \mu\mathrm{s}$. Results also show that bounce delay for thick and thin membranes is not related to the bias pulse width.

In order to understand if the measurement setup could introduce artifacts in the bounces characterization, a new measurement setup based on a crystal detector diode HP 423B, a Tektronix TDS680B, and a different probe station has been developed. The same results were obtained. The bounce characterization of a straight beams based shunt ohmic switch with $3\ \mu\mathrm{m}$ thick membrane is shown in figure 4.8.

Straight beams devices have exhibited the appearance of one bounce, closer to the instant the switch is turned off (around $55\ \mu\mathrm{s}$). This phenomenon is still under investigation, but from this first analysis it seems that the bounces presence is strictly related to the mechanical properties of the suspended membrane, and in particular to the spring constant of the suspensions. In table 4.1 it is reported a summary with the average of the bounce delays exhibited by the different typologies of tested devices.

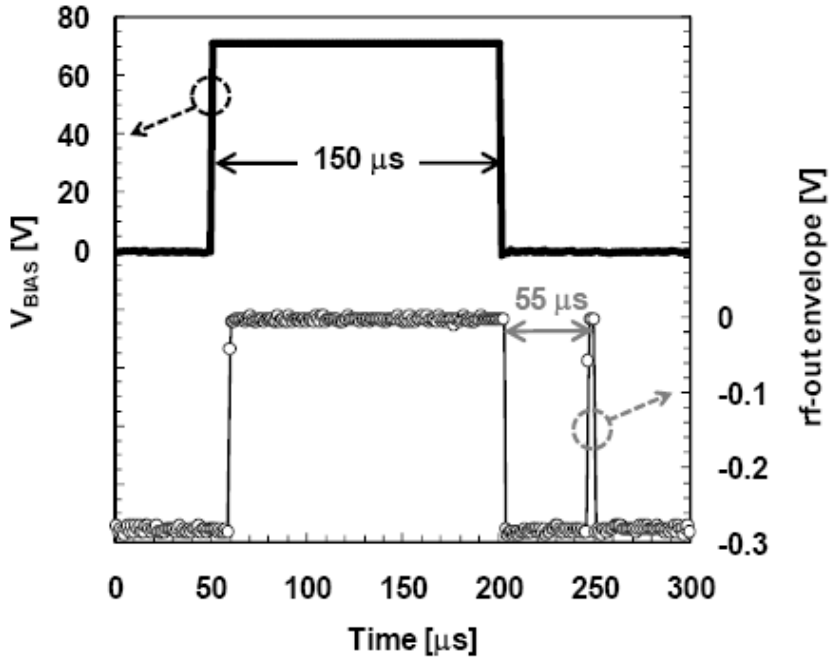

Fig. 4.8: Bounce on straight beams based switch with $3\ \mu\mathrm{m}$ *thick suspended membrane. The bounce delay (*$55\ \mu\mathrm{m}$*) is not pulse width dependent.*

Device Topology	**Suspension Type**	**Bounce Delay [**$\mu\mathrm{s}$ **]**
Series Thick	Meanders	250
Shunt Thick	Meanders	250
Series Thin	Meanders	170
Shunt Thin	Meanders	200
Series Thick	Straight beams	56
Shunt Thick	Straight beams	55

Table 4.1: Bounce delays for the different kinds of tested switches. The delay seems to be dependent on meanders shape and bridge thickness.

Chapter 5

Electro Static Discharge effects on MEMS

The wide variety of wireless standards in telecommunication is leading the market in the reconfigurable network systems direction for multiple standards handling. In this market, RF-MEMS offers an excellent solution in terms of high frequency, and low power consumption. Examples of applications for RF-MEMS can be actually found as tx/rx antenna switch in mobile phone, or in many spatial applications, thanks to the size and weight reduction in comparison to traditional mechanical coaxial switches.

In fact, MEMS is one of the most promising technologies in the development of nanosatellites (satellites that weight less than $10\ \mathrm{kg}$) which should be the upcoming solution for space net telecommunications and Earth monitoring. The possible combination of MEMS inertial sensors for space-position tracing, and high frequency MEMS switches for multi-standard RFnet developing, is expected to save weight and volume issues in space applications (actually a mechanical reconfigurable switch net can weight several kilograms) opening the road to the next generation satellites.

Unfortunately, still open reliability issues (electrical, mechanical, and environmental driven) can hamper the market entrance of RF-MEMS devices. The presence of continuous thermal cycling, shocks and vibrations (during take-off and solar panels opening), and last, but not least, Electro Static Discharge (ESD) and radiation phenomena, requires a severe certification of the devices reliability, since once the spacecraft has been launched, maintenance activity is almost unpractical. Considering MEMS in general, sensors and actuators have been introduced in the market for several years, and have achieved great success. MEMS have shown excellent robustness in terms of life-time as well as excellent performances. RF devices, on the contrary, are just becoming ripe for large scale production and sales, but are still suffering from reliability issues. Among these, one of the least investigated, while at the same time is one of the more critical issues, is the EOS/ESD phenomena. In fact, in terms of space applications, ESD phenomena are quite common on satellites due to the high intensity of electromagnetic fields that envelop the Earth.

As reported in literature by Koons et al. [33], ESD is the main cause of electrical equipment failure in space missions. With this said, it is clear that ESD phenomena must be fully

investigated for the promising technology of RF MEMS devices.

The main difference between RF-switches and other micro-machined devices is the greater probability to encounter EOS/ESD events. In fact, while sensors and actuators are typically packaged without any direct connection to pins exposed to the external world, a RF-switch could, for example, be exposed to EOS/ESD phenomena coming from the antenna connection. Furthermore, whereas sensors and actuators typically work in the kHz regime, RF input and output pins of RF switches must be able to work up to GHz signals. This high frequency operating regime makes very critical the protection of RF pins against EOS/ESD events, since any structure that is inserted to prevent damage will eventually add parasitic capacitance to the transmission line affecting the signal bandwidth. For such reasons, it is really difficult to protect RF-MEMS from EOS/ESD events, and we think that such devices should probably be treated and handled like class 0 ($0\ \mathrm{V} < 250\ \mathrm{V}$) or class 1A ($250\ \mathrm{V} < 500\ \mathrm{V}$) devices.

Interesting studies about the EOS/ESD sensitivity of MEMS have been presented in literature regarding sensors and actuators [39], while some efforts to study the robustness to EOS/ESD phenomena of RF-switches have been shown only in recent years, regarding capacitive devices [40, 41], and ohmic and capacitive switches [42]. These previous works however are limited to the analysis of not working conditions (up-state membrane position). However, the device in the actuated state is as statistically probable as is in the un-actuated one. In fact, when actuated, the stability of the metal-to-metal contact, peculiar of an ohmic switch, can be impaired by EOS/ESD phenomena: currents as high as several amperes can occur, which could result in the melting of metals (leading to stiction) or electro-migration phenomena.

5.1 The Transmission Line Pulser (TLP)

The common method used to generate square pulses of selectable duration and amplitude is based on the charging and discharging of the distributed capacitance of a transmission line (TL). High voltages are necessary in order to generate current pulses of several Amperes. A transmission line is a waveguide with a characteristic impedance Z_0 that only depends on the material and the geometry of the conductors and the dielectric isolating them. The distributed capacitance and inductance are expressed in $\mathrm{F/m}$ and $\mathrm{H/m}$ For negligible losses the electric and the magnetic field can be considered transversal to the direction of propagation. If a pulse travels along a transmission line, any discontinuity of the impedance $Z(x) \neq Z_0$ causes a partial reflection of the energy of the incident pulse. The reflection is of the same polarity as the incident pulse if the impedance difference $Z(x) - Z(x-1)$ is positive and of opposite polarity else. This effect is used for the characterization of unknown devices in the time domain reflectometer but must be minimized in the rest of the system.

For TLP-testing of integrated structures a high-voltage source is used to charge the distributed capacitance of the transmission line TL1 via a high-ohmic resistor, while the coaxial switch S1 is its open state. After the switch closes, the discharge of such a transmission line (TL1) into a resistive load or into TL2 produces a square pulse. The duration of the square pulse is equal to the length of the charged line divided by the velocity the signal propagates from the switch to the high-ohmic end of this line and back to the switch. As an example,

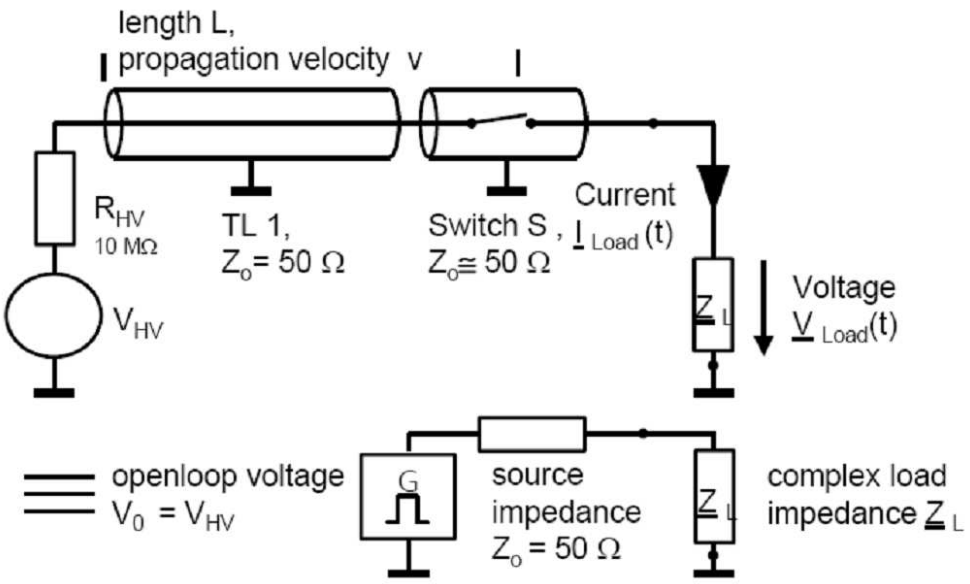

Fig. 5.1: Schematic of the TLP pulse generation section and its equivalent electrical model.

$10\ \mathrm{m}$ of the typical RG58 transmission line with a propagation velocity of $20\ \mathrm{cm/ns}$ generate a $100\ \mathrm{ns}$ wide pulse. The amplitude of the voltage pulse V is determined by the pre-charge voltage V_0 and the impedances of the source Z_s and the load Z_L:

$$V = V_0 \cdot \frac{Z_L}{Z_L + Z_S} \tag{5.1}$$

For a matched impedance in the switch and the load, the amplitude of the voltage pulse would be half of the pre-charge voltage.

In Figure 5.1 a schematic of the pulse generation section and its equivalent electrical model are reported.

Deviations from the ideal square shape of the pulse result from resistive and dielectric losses that are frequency-dependant as well as from variations in the impedance along the line through the whole system. For these reasons, it is mandatory to employ cables and components that are well matched, as short as necessary, and with low losses throughout the whole system. However, a dedicated long transmission line may be employed to tailor the rise time in order to comply with HBM or MM.

Software controls the equipment and extracts the actual current through a device $I_{DUT}(t)$ and the voltage across the device $V_{DUT}(t)$ and derives the various data from these measured data. Necessary equipment are the controller, the high voltage source, the oscilloscope and a source measuring unit for leakage measurement and for optional additional voltage bias of the DUT.

Looking at the HBM qualification test of the product, correlation between TLP and the standard test methods employed for qualification became a concern for the worth of the TLP method. With the extended application of the TLP methods also the results obtained with different TLP testers should be comparable. The TLP standard, which is currently developed by

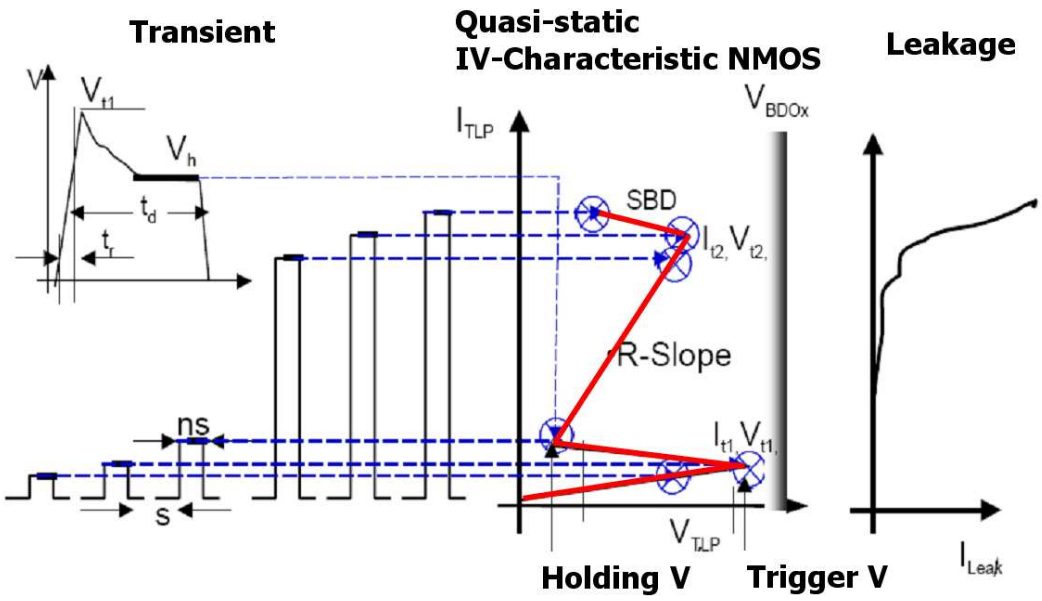

Fig. 5.2: Principle of the pulsed characterization with a series of increasing magnitude square pulses. I-V values at every pulse are obtained by means of averaging a certain region in the second half of the transient waveform.

the ESD Association, will significantly contribute to this comparability. In view of equivalent turn-on characteristics and energy-related failure mechanisms, TLP-pulse with a rise time in the order of $5\ \mathrm{ns}$ and a pulse duration of $100\ \mathrm{ns}$ are typically used. They translate $1\ \mathrm{A}$ into almost $1.5\ \mathrm{kV}$ HBM. Depending on the device and its electrical and physical failure signature, a more detailed analysis may be necessary.

Rise-time filters may be inserted into the transmission line behind the TLP pulse source in order to study rise-time effects. Ideally, the rising edge has a Gaussian shape. As a low-cost alternative, long transmission lines may be sufficient. Depending on the setup and the device to be stresses, electromagnetic interference between the stress terminals and control terminals, as an example the gate terminal, of the DUT can become an issue.

Just before the fundamentals and different setups for the generation and measurement of the square pulses are compared, the principle and terminology of the *quasi-static* pulsed device characterization is explained in figure 5.2 for the example of an nMOS transistor as a snapback protection element.

5.1.1 Time Domain Reflectometer TDR-TLP

The *Time Domain Reflectometer* TLP is based on the fact that if an incident square pulse reaches the DUT at the end of a transmission line, it will be reflected depending on the impedance $Z_{DUT}(t)$ of the DUT relative to the impedance Z_0 of the transmission line:

$$V_{reflected}(t) = \frac{Z_{DUT}(t - t_{delay}) - Z_0}{Z_{DUT}(t - t_{delay}) + Z_0} \cdot V_{incident}(t - t_{delay}) \tag{5.2}$$

This setup can maintain the $50\ \Omega$-impedance from the generator to the device with min-

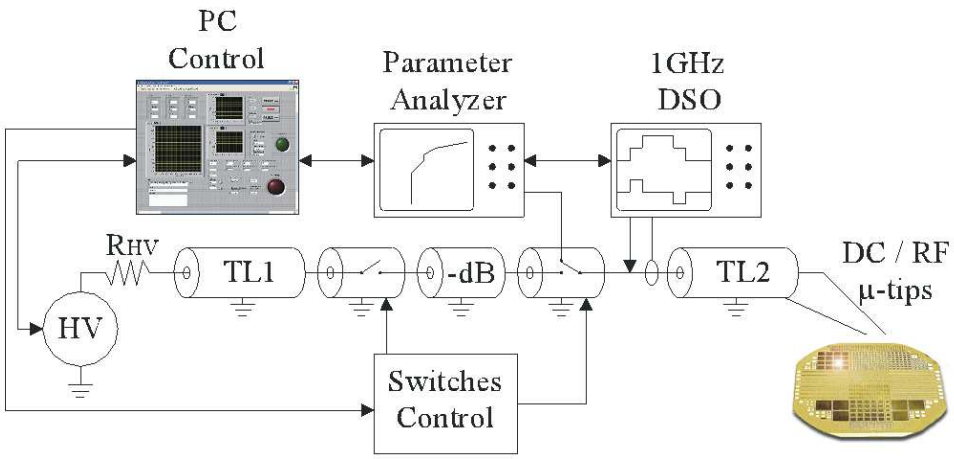

Fig. 5.3: Schematic of the Time Domain Transmission TLP.

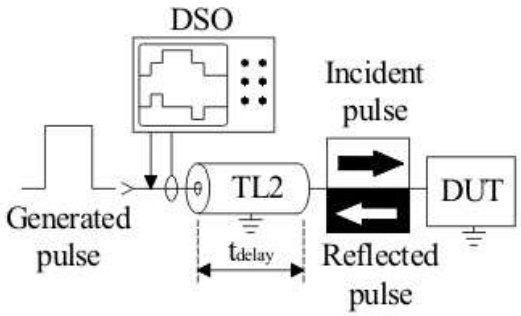

Fig. 5.4: Detail of the behavior of the waveforms incident to and reflected from the DUT.

imum parasitic elements and pulse distortion. In figure 5.3 is shown the schematic of the TDR-TLP, and in figure 5.4 a detail of the behavior of the waveforms incident to and reflected from the DUT is depicted.

This kind of TLP can be realized in two different configurations, with and without a current transformer CT in the signal path. The system with the current transformer uses an oscilloscope with two channels and measures voltage and current reflected from the DUT independently with the accuracy provided by the probes and the oscilloscope after a calibration of the attenuation factors of the system. Alternatively, for a known impedance Z_0, the current I(t) can be calculated from the relation

$$I(t) = \frac{V_{incident}(t)}{Z_0} \tag{5.3}$$

for the incident pulse, and

$$I(t) = -\frac{V_{reflected}(t)}{Z_0} \tag{5.4}$$

for the reflected pulse.

The transmission line TL3 between the resistive pick-off and the DUT delays the reflected pulse with respect to the incident pulse. Voltage $V_{DUT}(t)$ and current $I_{DUT}(t)$ at the DUT are calculated from the measured incident and reflected voltage pulses after a shift of the reflected pulse to the left by twice the one-way delay time t_{delay} and a correction for the attenuation of the resistive voltage pick-off and transmission lines, using the following equations:

$$V_{DUT}(t) = V_{incident}(t) + V_{reflected}(t - 2 \cdot t_{delay}) \tag{5.5}$$

$$I_{DUT}(t) = \frac{V_{incident}(t) - V_{reflected}(t - 2 \cdot t_{delay})}{Z_0} \tag{5.6}$$

Some uncertainty results from numerical effects for DUT impedances close to open and short and from distortion on the delay line TL3 in the phase of transition. Calibration to $0\ \Omega$ and a resistor together with correction improves the accuracy. If the reflected pulse is not completely separated from the incident pulse, the incident pulse must be very repeatable and flat. An attenuator between the pulse generator and the DUT is recommended in order to reduce multiple stress caused by multiple reflections that depend on the DUT impedance. Other concepts employ a diode in series with a termination resistor in order to reduce reflections from low-impedance DUTs ($Z_{DUT} \leq Z_0$) at the open end of the transmission line. This termination, that may even be switched in order to generate bipolar pulses, depends on polarity and should not be used for the characterization of oxides. A coaxial relay in the delay line allows to connect a DC-parameter analyzer to the DUT.

An overlapping Time Domain Reflectometer TLP has been implemented because it is seemed to be the most suitable solution to make square pulses with fast slopes and high values of voltage and current. Furthermore, thanks to the transmission line behavior, it is possible to study the evolution in time of the device response minimizing parasitic elements, in terms of parasitic resistance and impedance mismatch. In figure 5.5 it is possible to see the interface of the LabView program implemented to control all the TLP feature.

From the panel, it is possible to set the start, step, and stop voltage pulse, at which time percentage of the pulse make the average and how large is the averaging zone, which is the parasitic resistance that will be subtracted from the measurements, and which is the actuation factor of the voltage probe or the multiplication factor of the current probe. Regarding the leakage measurement, it is possible to set at which voltage measure it and the maximum applicable current, said the compliance level. This TLP implementation is based on a high impedance voltage probe and an ac current probe. Other TLP implementations extracts current values from voltage knowing the characteristic impedance of the transmission line. In this way it is possible to obtain more accurate I-V measurement and reduce the series resistance to less than $0.6\ \Omega$. This fact is very important for the measurement of resistance of low impedance devices like diodes. Some attenuators are used to reduce either noise or unwanted reflections. Changing the polarity of the high voltage supply, it is possible to make negative pulses. In figure 5.6 it is possible to see some example of voltage waveforms. The first step is made by the measurement of only the incident pulse, while starting from the second step, incident and reflected pulses are overlapped, and the measured voltage is the real voltage across the DUT.

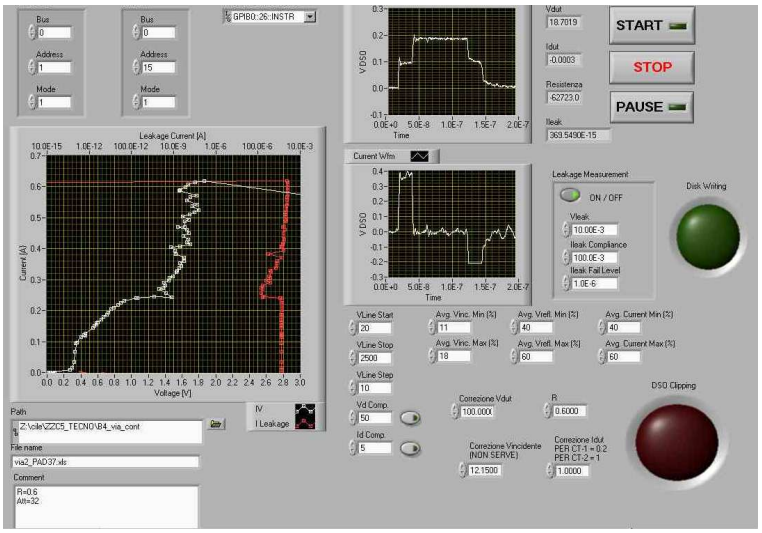

Fig. 5.5: LabView interface of the Transmission Line Pulser implemented.

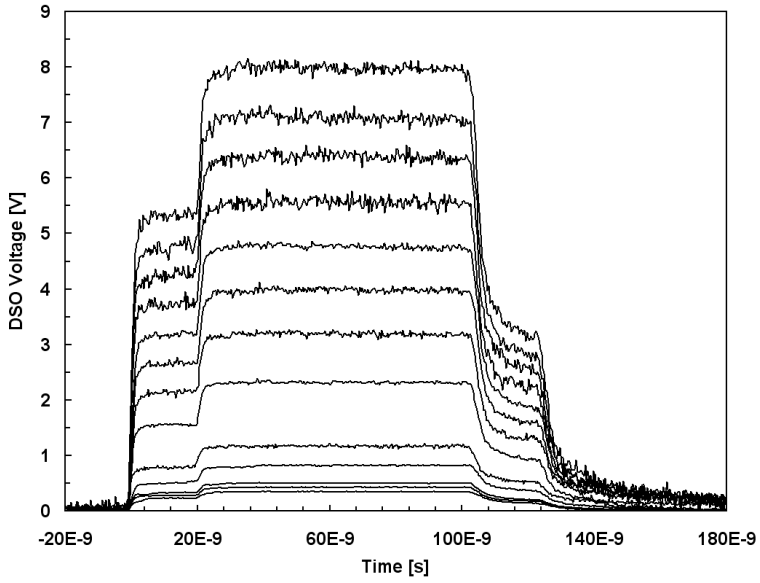

Fig. 5.6: Voltage waveforms of pulses with a pre-charge line voltage of 40 V *to* 1000 V*. In this case the voltage probe exhibit a 100x attenuation factor.*

Finally, the last step is due to only the reflected pulse. Typically, the averaging zone is chosen at the end of the overlapping area, but this could bring to measurement inconsistencies with some devices, as will be presented in this chapter for RF-MEMS switches. The rise time of the implemented TLP is lower than 1 ns, and it is possible to make some hundreds voltage pulses and current pulses higher than 50 A.

5.2 EOS/ESD sensitivity analysis

To test the ESD robustness of ohmic RF-MEMS switches, several devices have been submitted to TLP stress. The chosen ESD configurations of main interest for these devices are [43]:

- TLP between RF ground and Actuation pad (i)
- TLP between RF-IN and RF-OUT (ii)
- TLP between RF-IN/OUT and Actuation pad (iii).

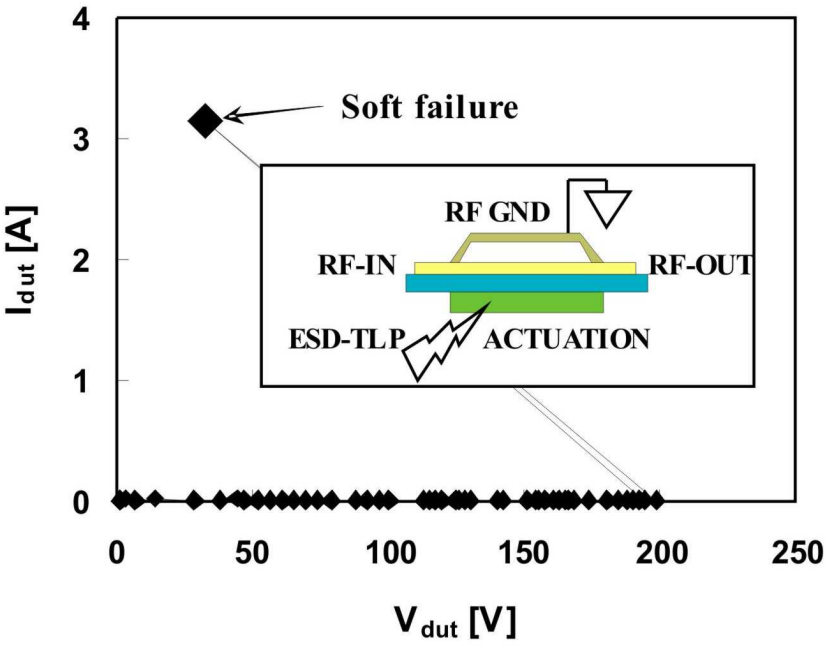

Fig. 5.7: Typical I-V plot of a RF-MEMS switch submitted to TLP stress between the actuation pad and the RF ground (open circuit). The device exhibits a normal behavior up to 200 V *where a breakdown occur and the device impedance rapidly changes to a short circuit configuration.*

The TLP stress between the actuation pad and the RF ground is of great interest due to the high electrical field between the actuation line and the thin oxide that separates it from the RF ground. The graph in figure 5.7 traces a typical I-V plot for a dielectric breakdown between the RF-ground and the actuation pad (open circuit). The device exhibits a normal behavior up to 200 V, where it is possible to see a rapid change of the device's impedance (from an open

to a short circuit). This is absolutely a very low voltage if compared with typical voltage levels of HBM stress.

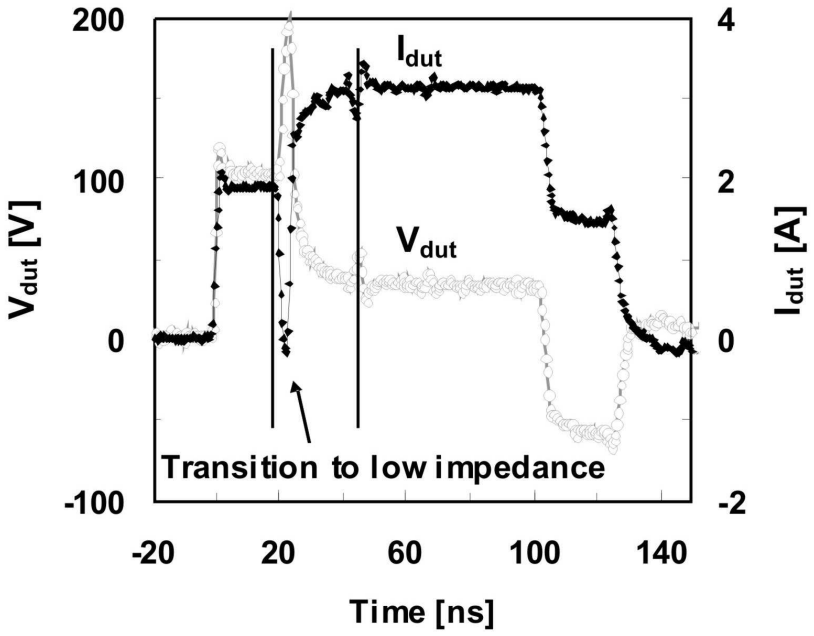

Fig. 5.8: Voltage and current waveforms of the TLP pulse during the soft-failure: the failure point is reached during the first nanoseconds of the TLP pulse.

In figure 5.8, voltage and current waveforms of the TLP pulse during the soft-failure point are depicted. It is important to note that the failure point is reached during the first nanoseconds of the TLP pulse. Comparing this situation with the measurement of standard semiconductor devices, after this condition has occurred, usually the device is destroyed, and typically a no more functionally working structure will be observed. This is not always true for MEMS switches. In fact, successive scattering parameters measurements show a still working device. Of course, the reiteration of the TLP discharge on the device lead to S-parameter degeneration and a complete destruction of the MEMS switch, but usually the DUT resists to some ESD phenomena.

Furthermore, in some cases, the TLP stress can improve the performance of the device, as shown in figure 5.9. In the graph it is possible to see the S_{21} evolution of two switches stressed with 1,000,000 cycling: the degradation rate of the TLP-stressed device is lower than the untreated one. Furthermore, the TLP stressed switch does not exhibit any non-actuation point during the cycling stress as a better contact condition is achieved after ESD events.

However, the TLP stress usually produces sensible damages to MEMS devices even if not fatal. The highlighted region of the picture in figure 5.10 shows the damage of the actuation line. In fact, during TLP testing, a spark is observed in that region, indicating metal wear-out mechanisms. This kind of damage is probably due to the breakdown of the Low Temperature Oxide (LTO) that is grown over the Ti-N metal line and, in this geometry, over via hole also. The "burnt zone" highlighted is where the Ti-N via contacts the poly-silicon way and only

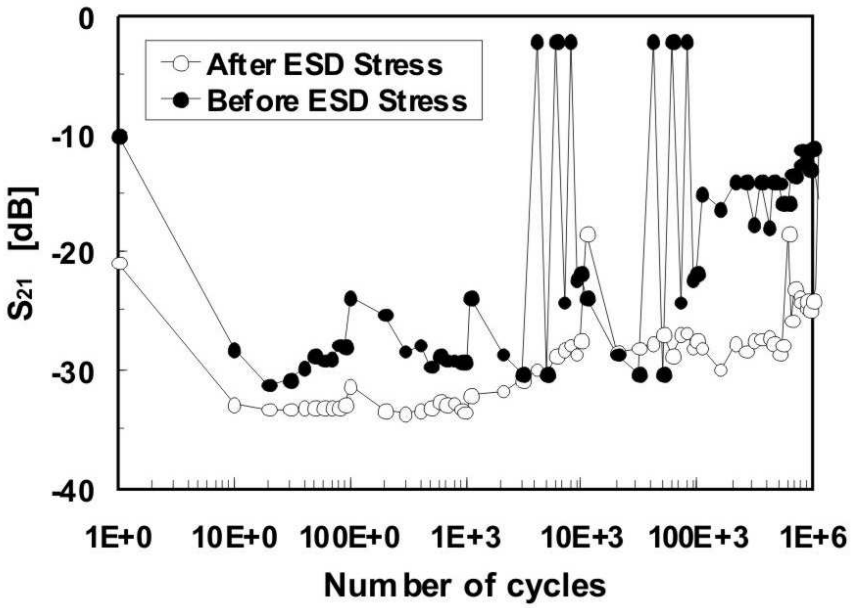

Fig. 5.9: S_{21} evolution of two switches stressed with 1,000,000 cycling: the degradation rate of the TLP-stressed device is lower than the untreated one.

where the LTO separates the actuation line from the ground of the switch. This configuration is probably the weaker of the actuation line, because, after the via, the poly-silicon way is also covered by the SiO_2 oxide, which exhibits a better hardness to TLP events. Probably, a different layout, with a larger distance between ground and actuation pad could improve the robustness to TLP stress. Therefore, should not be a surprise if the switch is still working after the first failure point, because only the LTO have been damage in this event.

If the TLP stress is reiterated, the complete destruction of the metal line will be observed. Obviously, in this case the actuation voltage can not anymore reach the poly-silicon fingers under the bridge and the switch will not be functional.

In figure 5.11, the typical I-V plot of a metal failure between the RF-IN and the RF-OUT (short circuit - case ii) is shown. In this configuration the hardness of the input to output transmission line under TLP stress is tested. As it is possible to see, in the first part of the I-V plot, the metal line exhibits a series resistance of approximately $2\ \Omega$ up to a current level of approximately $5\ \mathrm{A}$. This is a good robustness level, and it can be compared with an equivalent HBM robustness of approximately $7.5\ \mathrm{kV}$. Suddenly, without any anticipation as saturation or slope change, the metal line fails.

We have found two critical phenomena that explain the failure of the device. The first problem is the fusion of the metal line due to electro-migration [19], while the second one is the breaking of vias that connect the deposited gold with the Ti-N way. The effect of these fusions can be observed in figure 5.12, that exhibits the photo of fatal damages for such an ohmic switch in the interdigitated region of the input to output transmission line. Due to the high current during the TLP stress flowing through the fingers under the MEMS bridge, two fusion zones can be observed, and after this kind of damage the device never works again properly.

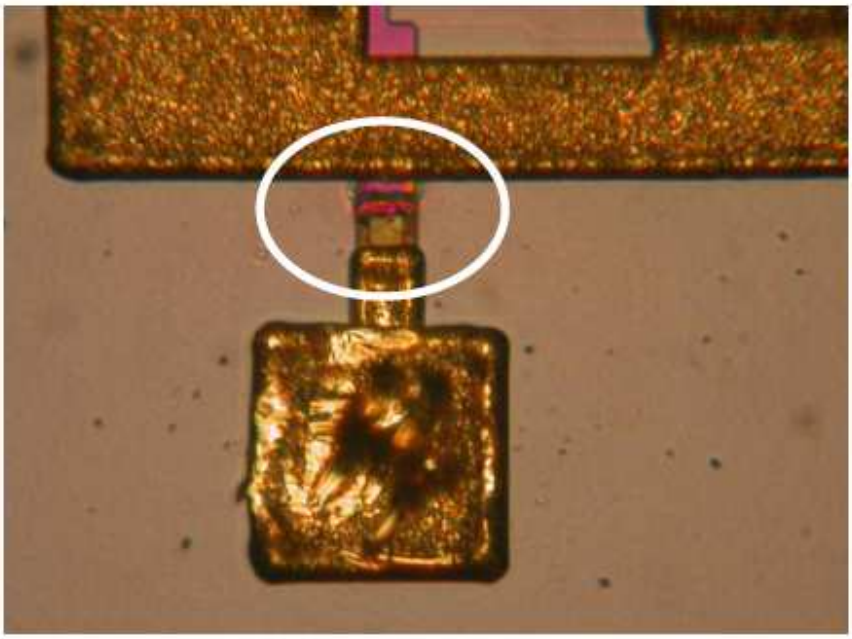

Fig. 5.10: Typical damage of an ohmic switch submitted to TLP stress between the actuation pad and the ground. The actuation line in the highlighted region appears burnt.

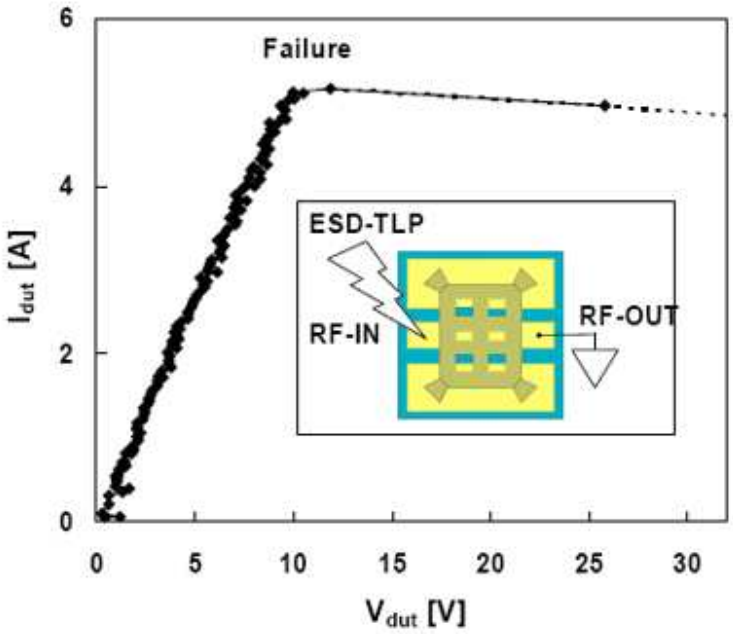

Fig. 5.11: TLP I-V characteristics a resistive shunt MEMS tested between the (electrically connected) RF-IN and RF-OUT pads (see the inset). After the Failure point an open circuit is observed.

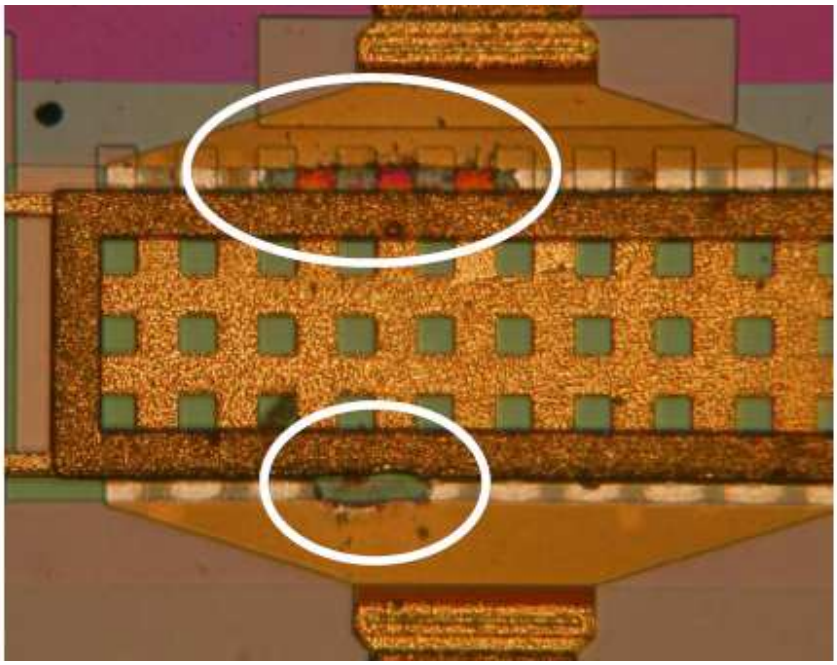

Fig. 5.12: TLP I-V characteristics a resistive shunt MEMS tested between the (electrically connected) RF-IN and RF-OUT pads (see the inset). After the Failure point an open circuit is observed.

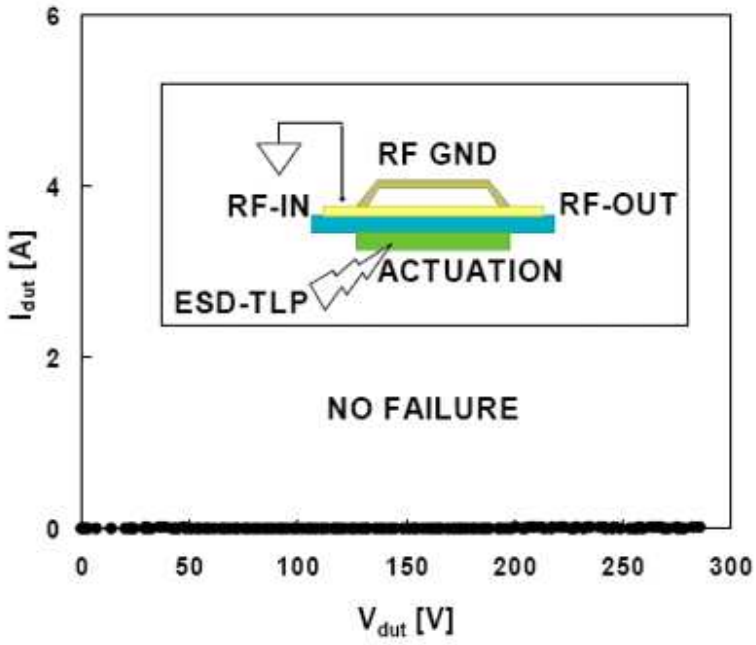

Fig. 5.13: TLP I-V characteristic of a resistive shunt MEMS tested between the (electrically NOT connected) actuation and RF-IN pads (see the insert). Dielectric breakdown is NOT observed in this configuration up to 280 V *TLP discharge.*

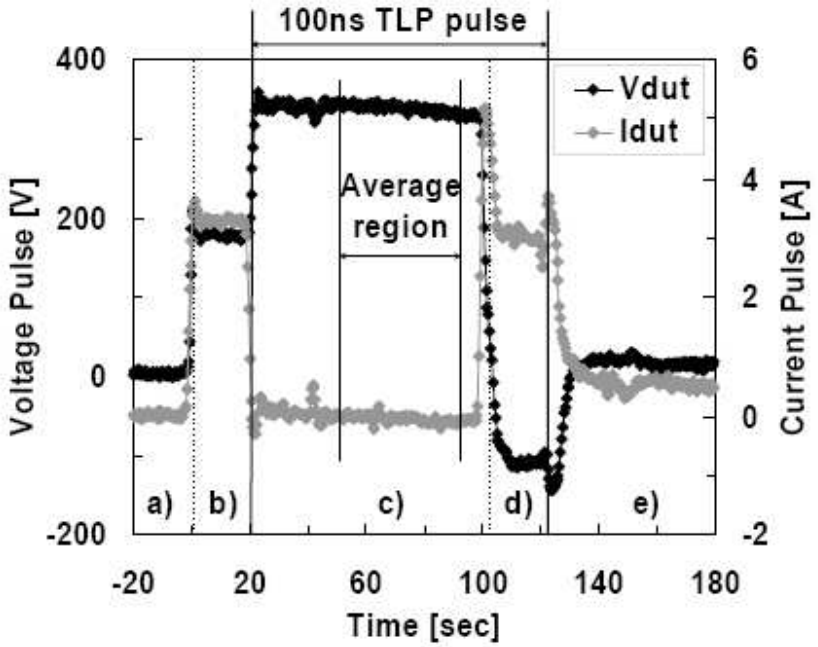

Fig. 5.14: Voltage and current TLP waveforms of a capacitive shunt switch aged with one million of cycles and stressed between the RF-IN and ground during the failure of the device.

Finally, regarding resistive switches, in figure 5.13 the I-V plot of a switch submitted to TLP stress between the RF-IN / OUT pad and the Actuation pad (case iii) is depicted. In this case it is very important to note that no failures have been observed during the stress and this should mean that the device is still alive. However, after this kind of stress, the device does not work anymore.

5.2.1 Device characterization after TLP pulses

In order to characterize the ohmic switches we have adopted the standard technique in which the points of the TLP I-V plot are typically extracted from an averaging of a limited zone of the voltage/current pulses as shown in figure 5.14 [44]. As soon as the adopted TLP is a TDR one, the device is stressed from 20 ns to 120 ns (100 ns pulse). A typical TLP system makes the measurement to build the I-V plot as an average of a limited region in the plateau of the pulse between 50 to 90 ns (zone c). As in this case, the failure region d) is not included in the averaging zone c). This makes the I-V plot (as shown in figure 5.13) not revealing the true behavior of the stressed device. Typically, as happens with classical devices, the successive leakage measurement gives the indication if the device is being degraded or destroyed. Regarding MEMS switches instead, the failure does not necessary occurs at the beginning of the TLP pulse and the averaging should not include the failure zone.

For this reason, the classical I-V curve does not always provide good information about the device life state and the leakage do not always helps to understand the device life state. In fact, during the measurements, it has been observed that leakage can change until to compliance level during the device-failure but this does not mean that the device is "dead" (figure 5.15).

As depicted in the figure, even if the leakage measurement exhibits a strong variation re-

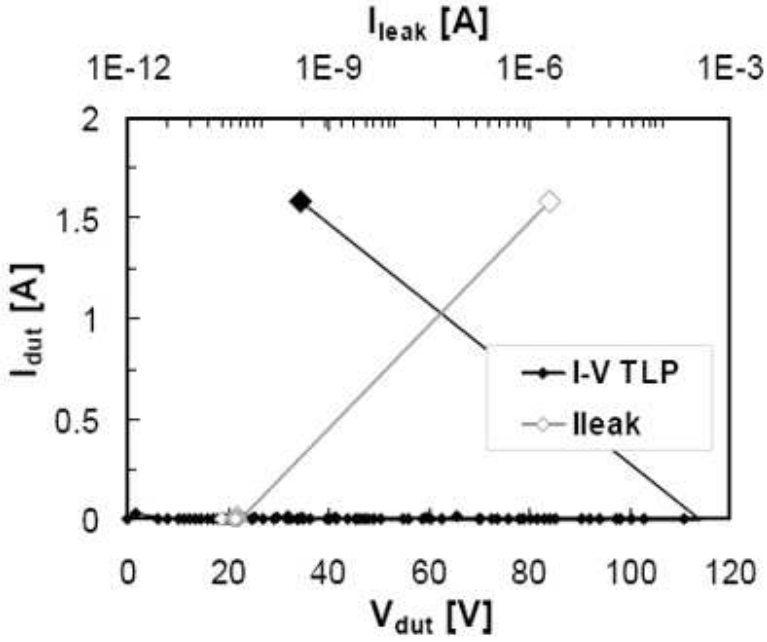

Fig. 5.15: TLP I-V plot and leakage behavior of a capacitive shunt switch submitted to TLP stress and still alive despite the change of the leakage current.

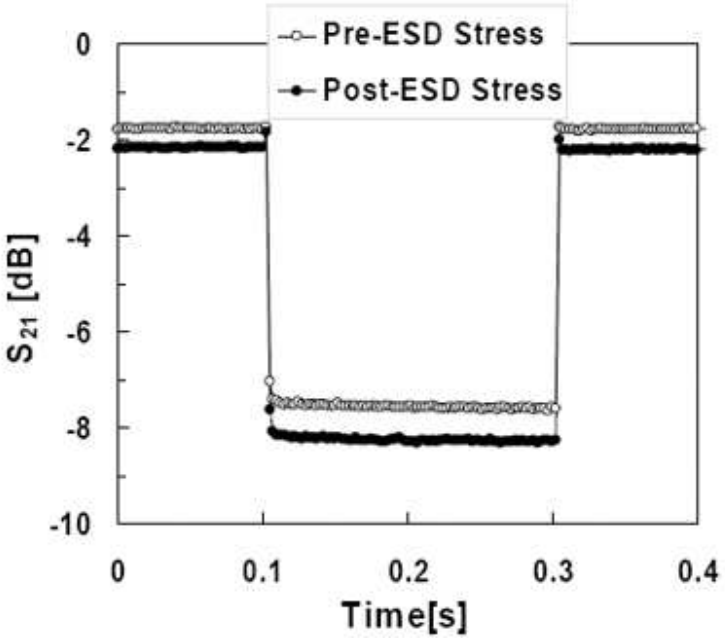

Fig. 5.16: Comparison between S_{21} Scattering parameter before and after the TLP stress reported in figure 5.15 in which the leakage measurement after the TLP pulse has reached the compliance value.

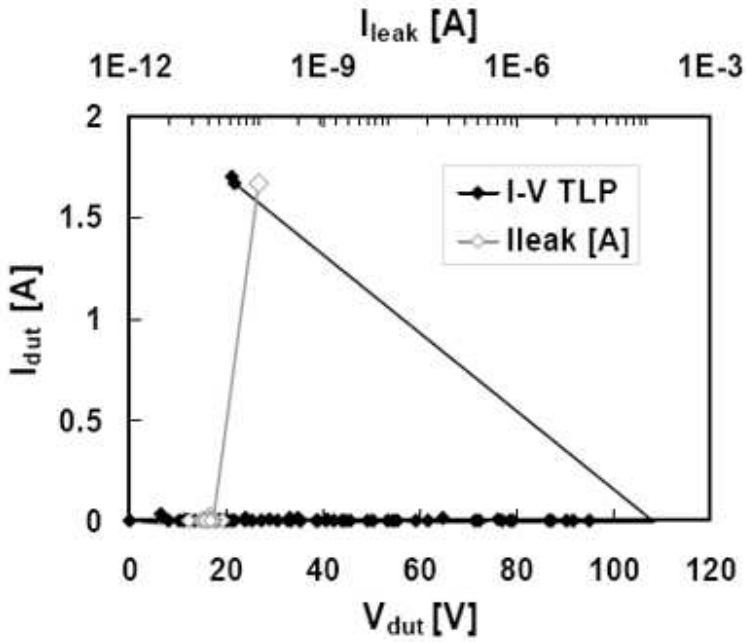

Fig. 5.17: TLP I-V plot and leakage behavior of a capacitive shunt switch submitted to TLP stress and destroyed by it. In order to characterize previous ohmic switches we have adopted the standard technique in which the points of the TLP I-V plot are typically extracted from an averaging of a limited zone of the voltage/current pulses as shown in figure 5.14 [44].

spect its initial value (the compliance limit of 2 μA was reached) the switch is still alive as confirmed by scattering parameters measurement depicted in figure 5.16. Furthermore, we observed that some time, during the device-failure, the leakage measurement remains approximately constant, as nothing happens, but after the stress the device is no more working. This is the case as shown in figure 5.17, where, despite the leakage measurement exhibits almost no variations, the device completely fails if actuated after the TLP stress, as it possible to see by the scattering parameters measurement shown in figure 5.18.

These situations mean that the classical approach used to evaluate the life state of a device under TLP stress can not be completely used, as it is, with MEMS switches. Similar results were found independently by Voldman and Hynoven on RF devices, circuits, and systems [45, 46]. For this reason a better analysis of pulses waveforms is required. In order to correctly characterize these kinds of devices, we have analyzed every pulse waveforms, and when a failure has occurred, we have built the final I-V plot joining the standard I-V plot (where the device does not exhibit any failure) with the evolution of the voltage and current of the device during the failure. In figure 5.19 it is possible to see this kind of curve, obtained from pulses shown in figure 5.14. The zones of this curve with a higher density of point (zones a-b-c-d-d'-e) represent the constant zones of the pulses. Pulses shown in figure 5.14 have also an important particularity. In fact, the failure has come some nanoseconds before that the incident pulse was totally separated from the reflected one (point d). For this reason, a careful elaboration must be provided in order to extract real voltage and current values (point d') and it is based on the evaluation of the voltage and current values reached during the incident pulse of the TLP stress.

After this elaboration the plot shown in figure 5.20 is obtained: in grey it is possible to

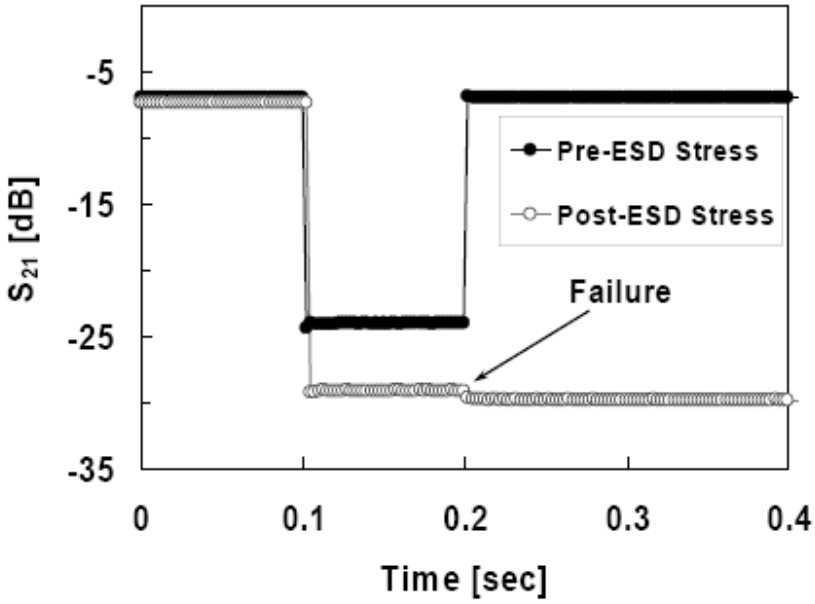

Fig. 5.18: S_{21} scattering parameter of the capacitive shunt switch TLP stressed shown figure 5.17.

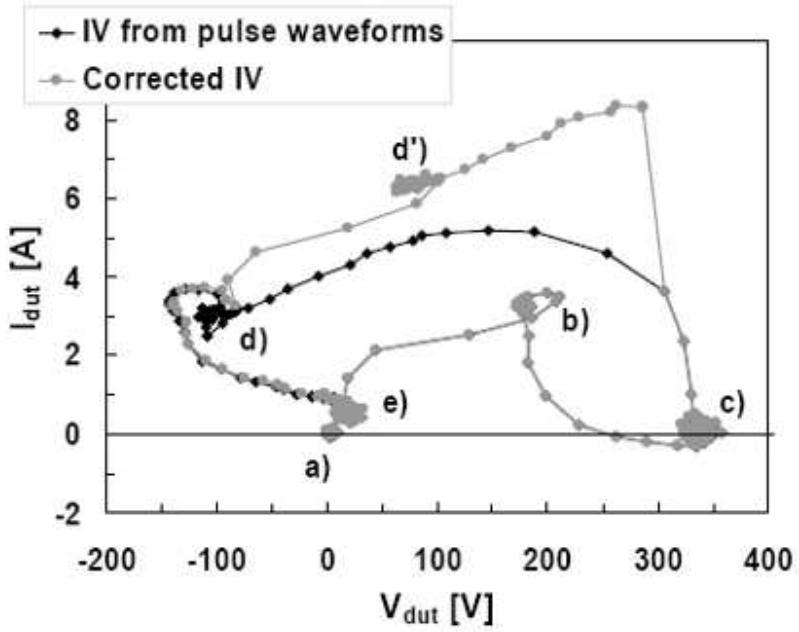

Fig. 5.19: I-V evolution of a capacitive shunt switch during the failure. Zones a) to e) are referred to figure 5.14.

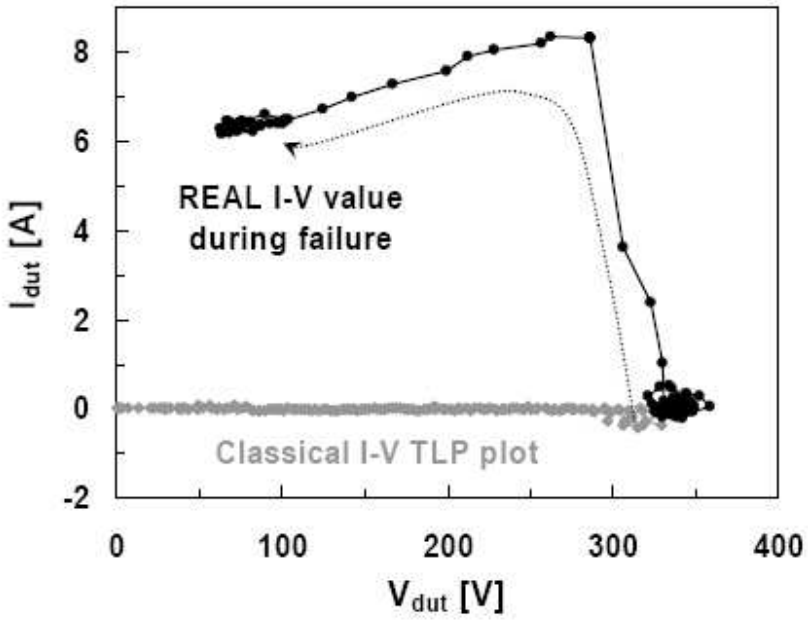

Fig. 5.20: Comparison between standard I-V plot (grey line) and real I-V evolution during the failure point of the capacitive shunt switch shown in figure 5.14.

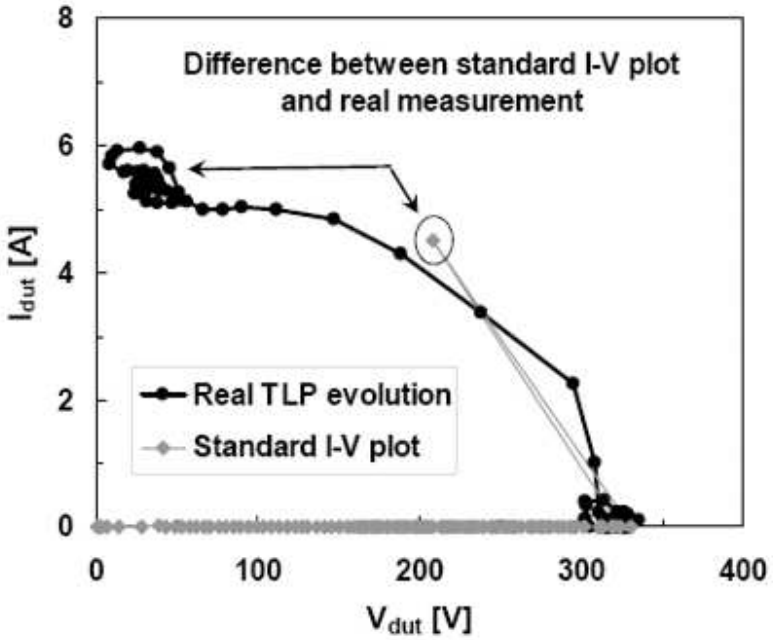

Fig. 5.21: Comparison between standard I-V plot (grey line) and real I-V evolution during the failure point of the capacitive shunt switch shown in figure 5.14.

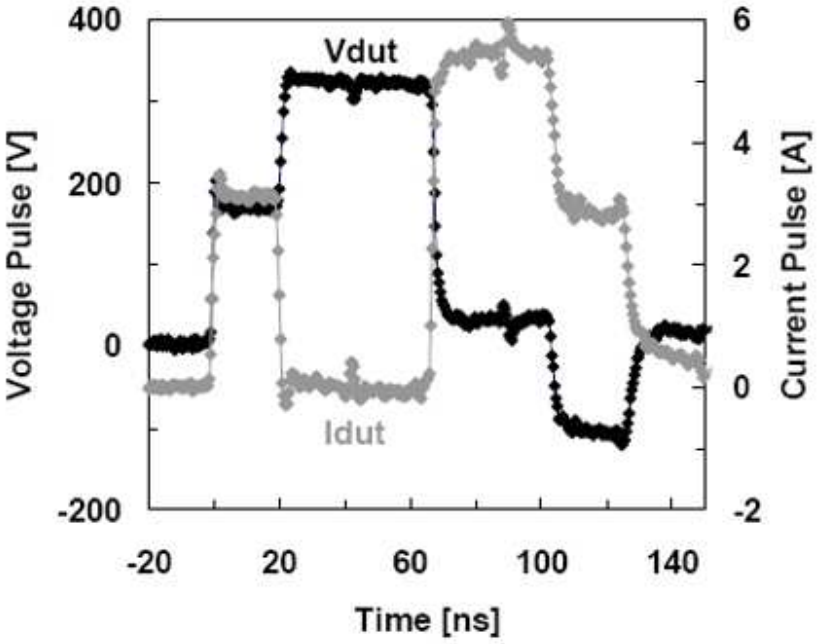

Fig. 5.22: Voltage and current pulses of the untreated device of figure 5.16. In this case the instability occurs 40 ns *after that the pulse has reached the maximum voltage (40% of pulse width).*

see the classic I-V trace, in black the one obtained with the new method. It is important to understand that this plot is not the complete I-V TLP evolution: the curve regards only the evolution during the failure region. Using this method it is possible to obtain the exact value of the voltage and the current passing through the device during the instability. The difference between the two traces is amazing: instead of an open circuit (300 V and approximately 0 A) we can observe a high passage of current (more than 6 A). In this case the power of such method of investigation needs no more words: without this seemed that nothing was happening to the switch.

In figure 5.21 it is shown the comparison between the classical I-V trace and the new method for an untreated capacitive switch submitted to ESD stress: also in this case we have different values for the voltage during the instability (10 V instead of 200 V) and for the current too (5.5 A instead of 4.8 A). As previously stated, the main issue of the classical method is that voltage and current values are extracted from the measured waveforms making an average in a well defined region. If this region is before the failure point or just before and after the failure region, extracted values are surely affected and they will be not real. As an example, in figure 5.22 the behavior of a capacitive shunt switch is reported during its failure. As depicted, the failure point occurs after 40 ns and if the averaging procedure was started before this point, the extracted voltage and current values would be incorrect.

A different way to plot the TLP I-V trace is required in order to obtain the real behavior of these devices, because classical I-V plot or leakage information are not sufficient to figure out if the device is still working properly or it is "dead". This new method to plot is based on the full analysis of the complete voltage and current waveforms, and not only on the averaging of a limited region. At the same time it is not enough to have complete information about the

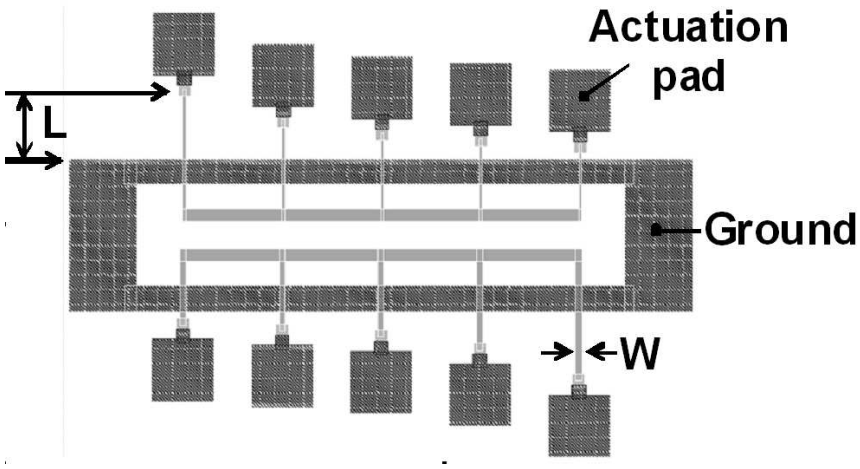

Fig. 5.23: Test structures used to study the EOS/ESD sensitivity between the actuation pad and ground.

life state of the device. In fact, there is nothing telling us if the device is still "alive" or "dead". Furthermore, scattering parameters measure must be inserted in the characterization chain to properly evaluate the device life state, as for other RF solid state devices.

5.3 HBM characterization

RF-MEMS switches under HBM regime have also been characterized, in order to study if any correlation between TLP tests and the Human Body Model exists for these devices. Preliminary results on the testing of the EOS/ESD sensitivity between the actuation pad and ground are here presented. Previous data [34] have shown that in this configuration TLP pulses of about 300 V are sufficient to destroy the device. HBM-like stresses on wafer level between actuation pad and ground have been applied to all the previously described topologies of RF-MEMS switches, starting at 50 V, with an increasing step of 50 V. We have obtained failure voltage levels between $300 - 350$ V, in good agreement with previously made TLP stresses. Like TLP tests, HBM stresses have brought to a complete destruction of the actuator polysilicon line, leading to a no more working device.

In order to better investigate where the dielectric breakdown occurs, the stress have been repeated using ad-hoc designed test structures (see figure 5.23). These are characterized by different distances (L) between the actuation pad and ground ($10, 20, 30, 50, 100$ μm, and two width (W) of the polysilicon lines ($5, 10$ μm). The aim was to understand if the breakdown occurs only at the crossing between the polysilicon line and the ground layer (separated by 100 nm of TEOS and 200 nm of LTO), or if the breakdown could be induced in air along the surface.

Using the on wafer HBM-like tester, the results depicted in figure 5.24 have been obtained. During the tests it has been used the measurement of the leakage current (at 40 V, nominal actuation voltage of the switches) as failure criterion. All tested structures present failure between 300 V to 350 V, without any significant dependence on L or W, as shown by the sudden increase from about 10 pA up to the set compliance current level (2 μA) of the leakage current.

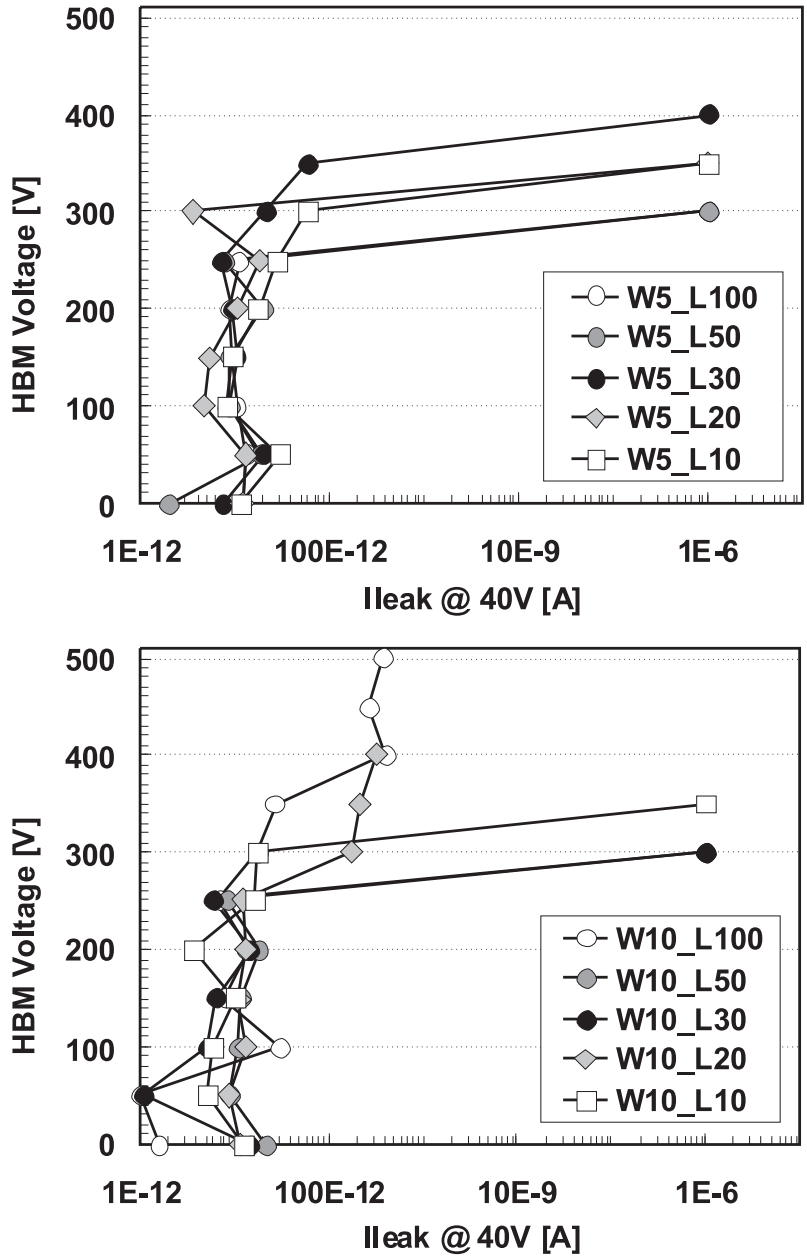

Fig. 5.24: Results of the HBM-like stress carried out on the test structures with polysilicon line width of $5\ \mu\mathrm{m}$ *(top), and* $10\ \mu\mathrm{m}$ *(bottom). The leakage current measured at* $40\ \mathrm{V}$ *was used as failure criterion.*

This leads to the result that the failure is due to the dielectric breakdown occurring in the cross between the polysilicon line and ground, and it is also confirmed by optical visible sparks in that zone. Devices W10_L100 and W10_L20, characterized by a lower increase of the leakage current than the other structures have shown the same sparks.

5.4 Electro mechanical simulations

The mechanical inertia of movable parts on RF-MEMS switches (not present in solid state devices) acts as a low pass filter to very fast transients (like ESD events) applied to the actuator pad. It has already been demonstrated the detrimental effects of strong ESD events on the reliability of RF-MEMS switches. However, it is interesting to investigate how the suspended membrane reacts to short electrical overstress, especially considering electro-statically actuated MEMS, which base their functioning on an electrostatic potential between the actuator electrodes and the suspended structure.

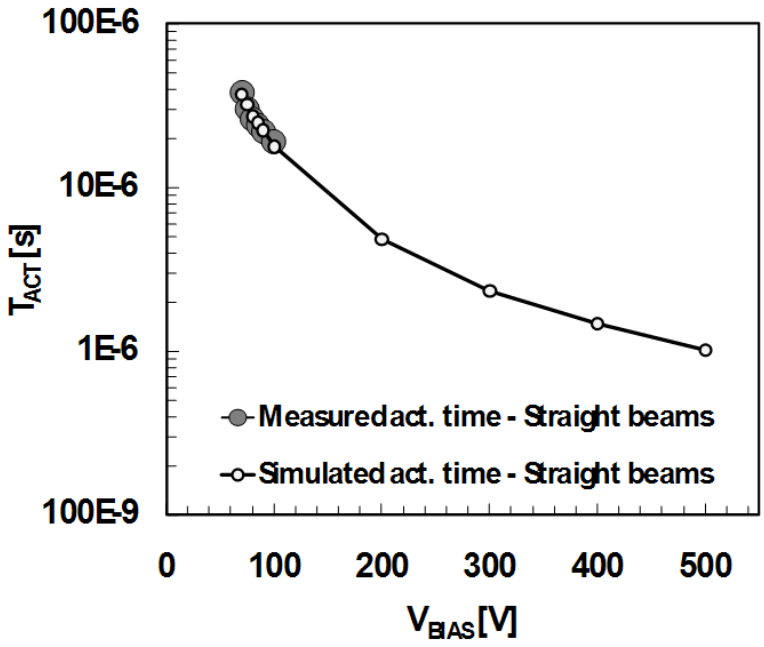

Fig. 5.25: Measured and simulated actuation time of studied RF-MEMS switches at increasing bias voltage.

In order to better understand if, despite its typical short duration, an ESD event applied to the actuation pad, can be energetic enough to bend or to fully actuate an RF-MEMS switch, a simulation of straight beams based devices has been performed with the electro-mechanical Finite Element Method (FEM).[1] As first step the actuation time at increasing bias voltages have been studied. Switches actuation times were measured biasing the devices with a rectangular shape voltage pulse (Hp 8114, 5 ns rise time), applying a 6 GHz, 0 dBm RF signal to the RF-IN pad, and connecting the RF-OUT pad to a Tektronix TDS 6804 (8 GHz analog bandwidth) DSO. The actuation time has been defined as the time the RF-OUT signals spends to reach the 90 % of its final value, starting from the rising of the bias voltage. Actuation time measurements for straight beams based switches are reported in figure 5.25. The developed model of the straight beams based switch well fit experimental measured actuation time, as shown in figure 5.25. Then, it has been performed an electro-mechanical simulations in order to evaluate the maximum displacement of the suspended membrane at increasing bias voltage, and at different

[1] Comsol Multiphysics ver. 3.3a, Transient Analysis

pulse length (in the range of typical ESD-like events), the results are shown in figure 5.26

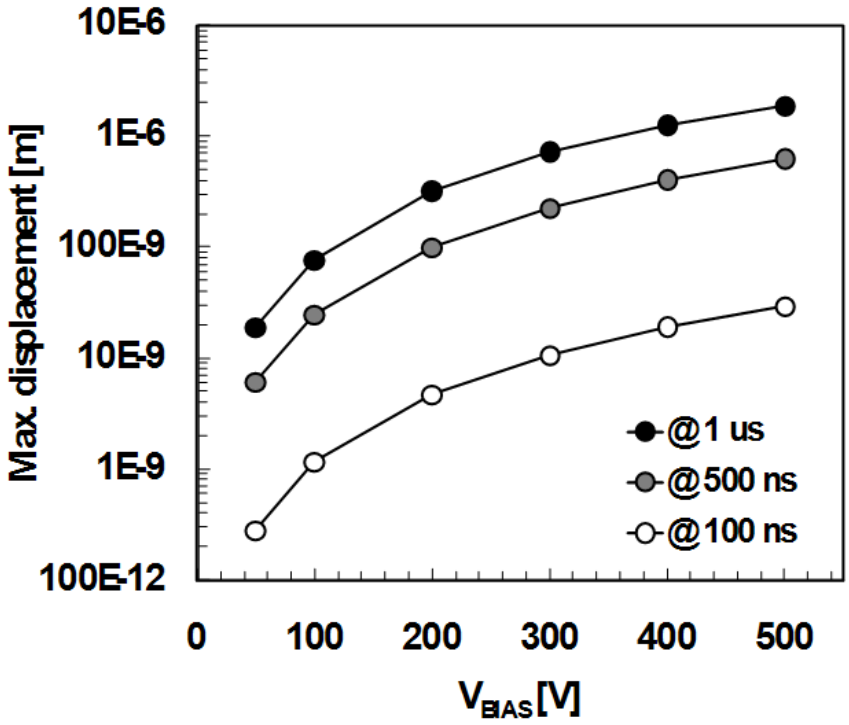

Fig. 5.26: Electro-mechanical simulations with the maximum displacement of the suspended membrane at increasing bias voltage, and at different pulse length. The lack of linearity in the gap displacement behavior is due to the nonlinearity of the equation that rules the beam actuation movement. In this case the curves are increasing for we are considering the differential displacement ($g_0 - g$) instead of the gap absolute value (g), with g varying between g_0 and 0.

It is interesting to note that simulation predicts that a 400 V, 100 ns long pulse, leads to a negligible maximum displacement of about 10 nm. Thinking that 400 V roughly corresponds to the maximum voltage applicable to the actuator pad before dielectric breakdown occurs between the polysilicon line and ground, the suspended membrane is virtually free from any movements during 100 ns long TLP tests. The membrane movement can be larger considering pulses in the range of the μs , like during HBM-like events. Simulations show that a 400 V, 1 μs long pulse leads to a maximum displacement of about 1 μm, that means one third of the RF-MEMS switches air gap. From this result we can argue that an ESD event can be energetic enough to bend the suspended membrane (even if it does not damage the switch), leading the device to assume an unwanted actuation with possible errors in the switch logic state.

5.5 EOS induced stiction

To investigate the effect of Electrical Overstress (EOS) on RF-MEMS switches, the DC characterization setup has been improved (S-parameters as a function of applied voltage) with the capability to measure the current drained by the actuator electrodes (I_{Act}). The comparison of S_{21} and I_{Act} measurements of a shunt, meander-based switch is reported in figure 5.27.

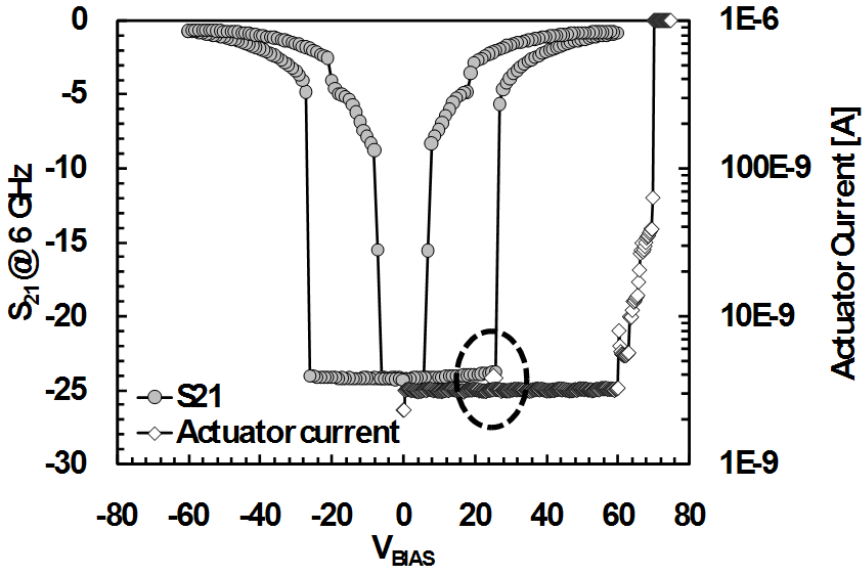

Fig. 5.27: Comparison of S_{21} and I_{Act} measurements of a shunt, meander-based switch. I_{Act} compliance limited to $1\ \mu\mathrm{A}$.

It is possible to note that I_{Act} can furnish a precise value of the actuation voltage (V_{Act} = 25.5 V, as highlighted by the dotted circle in figure 5.27), due to the transient increase of the capacitor displacement current, and the value is in perfect agreement with the S_{21} variation due to the actuation of the switch. It is interesting to note that I_{Act} starts to suddenly increase for $V_{Bias} > 60$ V, due to the breakdown of the oxide layer ($100\ \mathrm{nm}$ of TEOS and $200\ \mathrm{nm}$ of LTO) between the suspended membrane and the actuator line. The region affected by the dielectric breakdown is highlighted in figure 5.28.

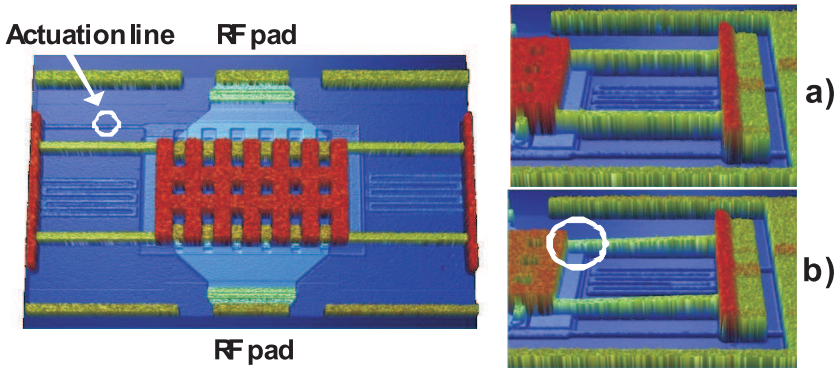

Fig. 5.28: Optical profilometer images of tested devices: un-actuated (a), and actuated (V_{Bias} = 60 V). The circle in (b) highlights the zone where the dielectric breakdown occurs.

It has been observed that if the actuator current is not limited (setting the compliance level of the Keithley 2612 to a maximum value of $1\ \mu\mathrm{A}$), this dielectric breakdown can lead to a permanent stiction of the suspended membrane. In figure 5.29 it is shown the evolution of S-parameters and actuator current during the test with no compliance set on I_{Act}.

At $V_{Bias} \approx 80$ V, I_{Act} increases up to about $2\ \mathrm{mA}$, and from that point the actuator assumes an ohmic behavior and the S_{21} parameter does not show any variation during the test. In this

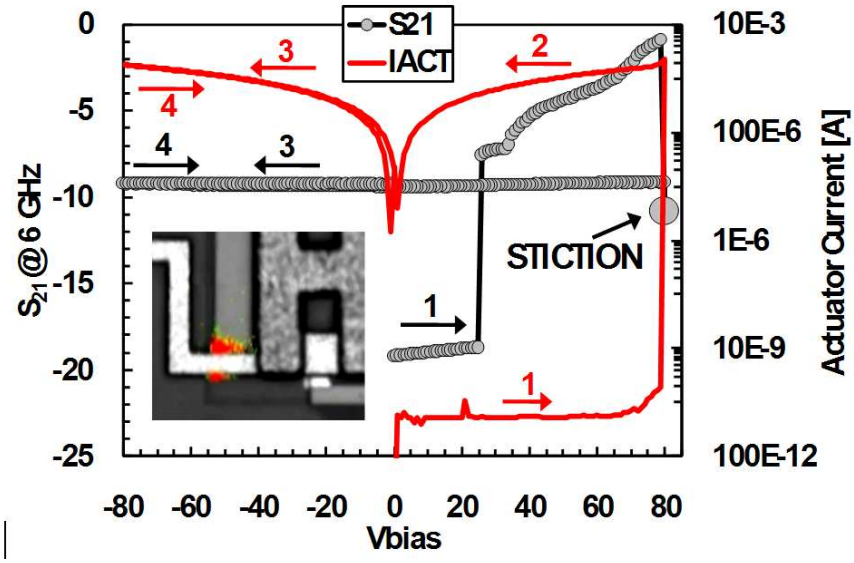

Fig. 5.29: Comparison of S_{21} and I_{Act} measurements with no current limit. The device remains stuck, in the point highlighted by the emission microscope image reported in the inset.

case the dielectric breakdown has lead the device to remain stuck and partially bended. The emission microscope (Hamamatsu PHEMOS-200) clearly indicates the point where the failure has occurred (inset of figure 5.29). Devices with different anchorage layout (without crossing with the actuation electrodes) have been tested, obtaining an highly increased robustness. The next step will be the study of the Time-to-Breakdown (TTBD) of such failure mode.

Chapter 6

RF-MEMS Radiation Sensitivity for Spatial Applications

Radio Frequency Micro-Electro-Mechanical Systems (RF-MEMS) have been proved to be interesting candidates to overcome the limits of actual state-of-art solid state devices. Small dimensions and light weight make such devices very appealing for spatial applications. However, their reliability is still an open issue due to the harsh space environment is considered, where radiation induced damage is one of the main causes of failure [33]. In particular, the behavior after exposure to ionizing radiation of devices having mechanical motion governed by electric fields across insulators has been seldom studied, mainly in MEMS sensors [47] or capacitor-like structures [48]. Just few authors have analyzed complete RF-MEMS devices [49]. It is well known that space is a harsh environment for standard micro and nano electronic components [50], but recent studies have indicated the possibility that also micro-mechanical structures can be hampered by radiation damages (see par. 2.2.3). Especially MEMS structure driven by electrical field, as RF-MEMS switches, would suffer the consequences of radiation damage mainly due to parasitic dielectric charging and substrate damages. In fact, these components use very often as dielectric silicon dioxide or silicon nitride which have an high charge trapping rate with a low charge mobility, therefore the injected charge can have a long life time before to anneal for thermal recombination. Moreover, the metal typically used to build the suspended membrane could be affected by a spring restoring force alteration due to the Young module changing induced by radiation and it would be also more vulnerable to creeping and fracture. The standard satellite radiation shielding has been proved to be a good solution to guarantee the electrical device lifetime during space missions (with some exceptions of course, see table 2.3), however, since the main application of MEMS devices would be on nano-satellites, it is difficult to prospect the possibility of a strong radiation shield on a few kilograms satellite.

6.1 Radiations

There are numerous system environments that can lead to significant radiation-induced degradation of electronic components, including space environments and the environment associated

with high-energy particle accelerators [32].

A major goal of the radiation effects community has been to provide devices that can function as intended in the harsh radiation environment of space. This has required the development of process and design techniques to fabricate radiation-hardened devices and the development of reliable, cost-effective hardness assurance test procedures. To qualify a device for use in a space system, one must rely on laboratory measurements typically at dose rates from 50 to 300 rad(SiO_2)/s in which the radiation exposure may take only minutes to hours to complete. These laboratory measurements must be correlated to a space environment in which the radiation exposure may take place over a period of many years.

To make these correlations, it is necessary to have a good understanding of the mechanisms that govern the radiation response of the devices to be used. This is especially true for systems employing commercial, non-radiation-hardened devices where the margin between system requirements and device capability may be much lower than for radiation hardened devices.

Thus, as commercial devices become increasingly more pervasive in space systems, the need for understanding radiation-response mechanisms becomes increasingly more important. Insight into the mechanisms for device radiation response has also enabled the fabrication of radiation-hardened devices. Understanding the basic mechanisms of radiation effects is therefore of practical importance to the system, design, and technology engineer.

6.1.1 Ionizing Radiation

Ionizing radiation generates electron-hole pairs in semiconductor materials. For MOS device degradation, the primary concern is electron-hole pair generation in oxides. Some fraction of the electrons and holes become trapped in the oxide and some fraction cause the release of hydrogen and induces interface traps at the Si/SiO_2 interface. In this section, the mechanisms by which ionizing radiation generates electron-hole pairs will be reviewed. The manner in which radiation interacts with solid material depends on the type, kinetic energy, mass, and charge state of the incoming particle and the mass, atomic number, and density of the target material.

Ionization of a target material occurs for photons, electrons, protons, and energetic heavy ions. Photon interactions are not a primary concern for satellites in the natural space environment. However, we include photon interactions in this discussion because of their importance in hardness assurance testing. Most laboratory sources, used to simulate total-dose space environments, emit either low-energy x rays or high-energy gamma rays.

Photon Effects

Photons interact with material through three different processes, namely the photoelectric (or fluorescent) effect, the Compton effect, and pair production [51]. These processes are illustrated in figure 6.1. For each of these processes, the primary result of the interaction is the creation of energetic secondary electrons.

Low-energy photons interact with material predominantly through the photoelectric effect. The photoelectric effect is illustrated in figure 6.1a. In this process, an incident photon excites an electron from an inner shell of a target atom to a high enough state to be emitted free of

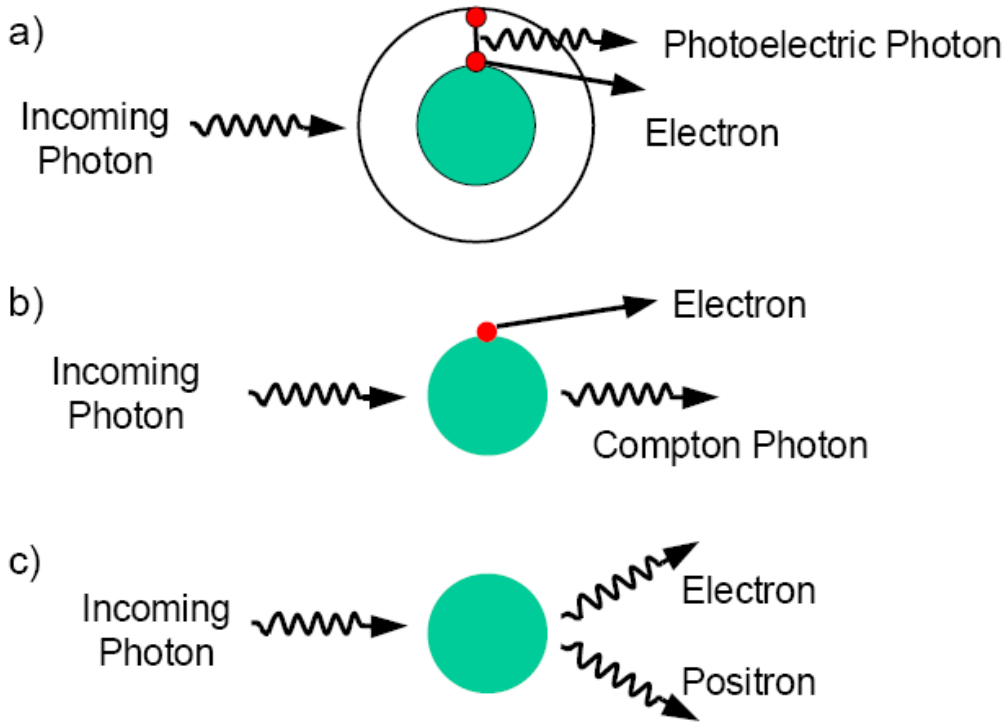

Fig. 6.1: Schematic drawing of three processes through which photons interact with material: a) photoelectric effect, b) Compton effect, and c) pair production.

the target atom. The incident photon is completely absorbed. Thus, the photoelectric effect creates a free electron (photoelectric electron) and an ionized atom. In addition, as the III-6 photoelectric electron is emitted, an electron in an outer orbit of the atom will fall into the spot vacated by the photoelectron causing a low-energy photon to be emitted. In general, the low energy photon does not have sufficient energy to create additional electron-hole pairs, but depending on the energy of the incident photon, the emitted electron can generate numerous additional hole-pairs. For higher-energy photons, Compton scattering will dominate over the photoelectric effect. Compton scattering is illustrated in figure 6.2b. In this process, as a photon collides with an atom, the photon transfers a fraction of its energy to an electron of the target atom, giving the electron sufficient energy to be emitted free of the target atom. For Compton scattering, a photon of lower energy is created which is free to interact with other target atoms. It can also create a free electron and an ionized atom. Pair production occurs only for very-high energy photons ($E > 3$ MeV). It is illustrated in figure 6.1c. In pair production, the incident photon collides with a target atom creating an electron-positron pair. A positron has the same properties as an electron (charge and mass), except that the charge is positive. The incident photon is completely annihilated in pair production.

The relative importance of the three processes as a function of photon energy and atomic mass of the target material is illustrated in figure 6.2 [52]. Shown in figure 6.2 are regions where each process dominates. The solid lines correspond to equal probabilities for the different interactions. The dashed line corresponds to the atomic mass of silicon ($Z = 14$). Thus for silicon, x rays emitted from a low-energy (typically $10\ \mathrm{keV}$) x-ray irradiator will inter-

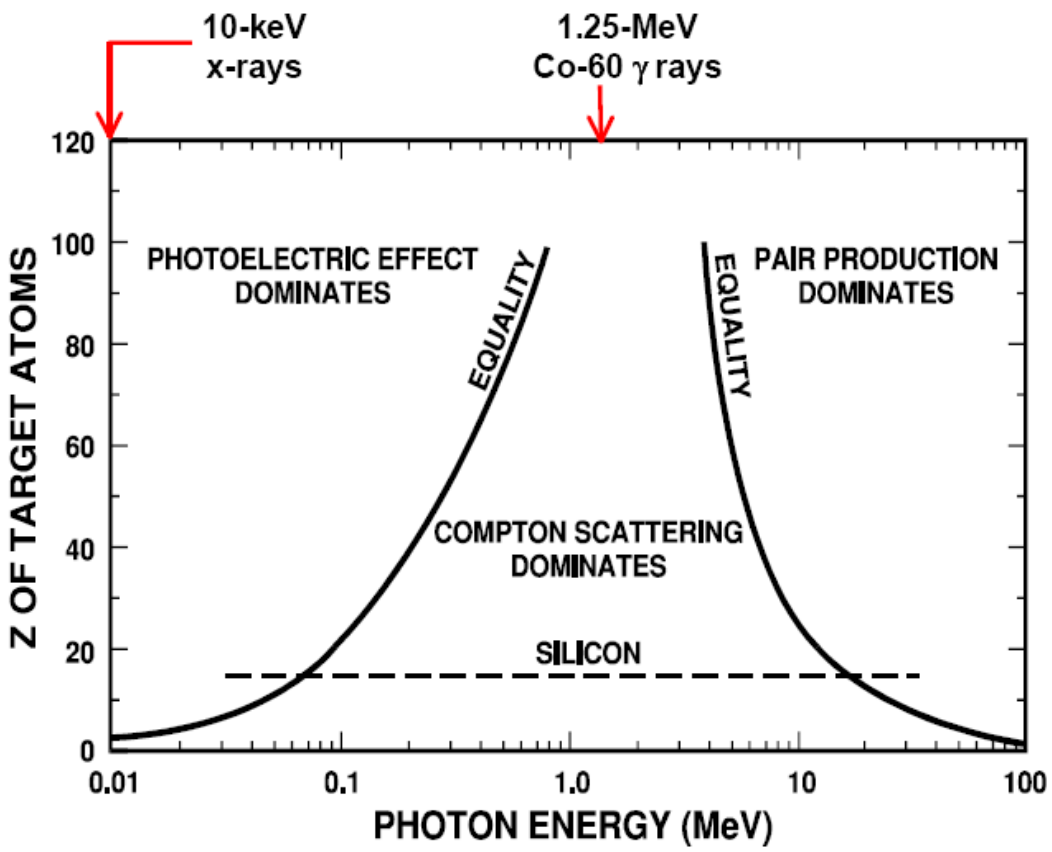

Fig. 6.2: Relative importance of the photoelectric effect, Compton scattering, and pair production as a function of photon energy.

act predominantly through the photoelectric effect, while high-energy gamma rays (typically 1.25 MeV) from a ^{60}Co source will interact predominantly through Compton scattering.

Electron-Hole Pair Generation

High-energy electrons (secondary electrons generated by photon interactions or electrons present in the environment) and protons can ionize atoms, generating electron-hole pairs. As long as the energies of the electrons and holes generated are higher than the minimum energy required to create an electron-hole pair, they can in turn generate additional electron-hole pairs. In this manner, a single, high-energy incident photon, electron, or proton can create thousands of electron-hole pairs.

The minimum energy required for creating an electron-hole pair, E_p, in silicon, silicon/dioxide and GaAs is given in table 6.1 [51, 53, 54]. Also given in table 6.1 are the densities [55] for the three materials and the initial charge pair density per rad deposited in the material, g_0 [51]. The latter quantity is obtained from the product of the material density and the deposited energy per rad divided by E_p [51]. A rad (radiation absorbed dose) is a unit often used to quantify the total absorbed ionizing dose in a material. It is a measure of the amount of energy deposited in a material and is equal to 100 ergs of energy deposited per gram of material (1 rad = 100

Material	E_p *[eV]*	*Density [g/*cm^3*]*	*Pair density generated per rad* g_0*[pairs/*cm^3*]*
GaAs	4.8	5.32	$7 * 10^{13}$
Silicon	3.6	2.328	$4 * 10^{13}$
Silicon Dioxide	17	2.2	$8.1 * 10^{12}$

Table 6.1: Minimum energy for creating electron-hole pairs, density, and pair density generated per rad for GaAs, silicon, and silicon dioxide.

erg/g = 6.24 x 10^{13} eV/g). The energy deposited in a device must be specified for the material of interest. Thus, for a MOS transistor, total dose is measured in units of rad (SiO_2) or rad(Si). Another unit often used is the Gray (Gy). The conversion factor from rad to Gy is 100 rad = 1 Gy.

6.1.2 Dose Enhancement

Another mechanism that affects the total number of electron-hole pairs generated in a material is dose enhancement. Dose enhancement arises when an incident particle travels through two adjacent materials with different atomic masses. Close to the interface of two materials, charge particle equilibrium is not maintained. Charge particle equilibrium is defined as the condition where the total energy carried out of a given mass element by electrons is equal to the energy carried into it by electrons [56].

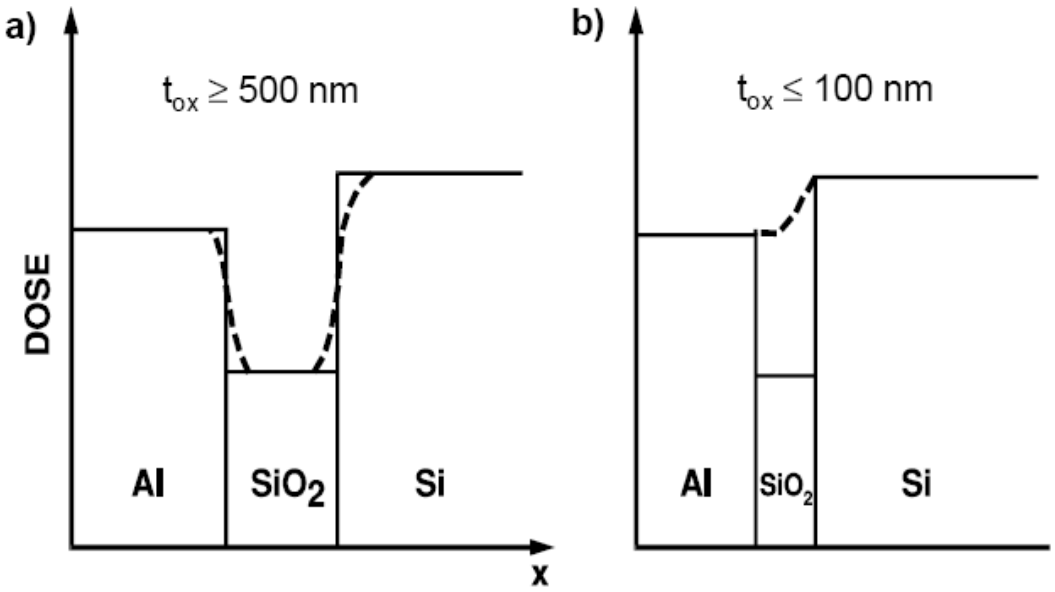

Fig. 6.3: Schematic diagram illustrating dose enhancement for a) a thick oxide (t_{ox} 500 nm) and b) a thin oxide (t_{ox} 100 nm). The solid lines indicate bulk equilibrium dose and the dashed lines indicate the actual dose profiles.

For two adjacent materials with different atomic masses, the number of electrons generated in the low-atomic mass material close to the interface will be higher than for the case where charge particle equilibrium is maintained (i.e., far away from the interface) as shown in figure

6.3. This effect is called dose enhancement. For thick oxides, see figure 6.3a, some dose enhancement in the SiO_2 occurs near the oxide interfaces (dashed lines), but for the majority of the oxide, the actual dose in the SiO_2 is close to its equilibrium dose (solid lines). For thin oxides, shown in figure 6.3b, the actual dose (dashed line) is considerably enhanced over the equilibrium dose. The criterion for thin or thick depends on the distance that secondary electrons will penetrate into the material. For $10\ \mathrm{keV}$ x rays in SiO_2, the average range of secondary electrons is approximately $500\ \mathrm{nm}$. This distance is considerably longer than the gate oxide thickness of modern IC technologies and in many cases it is comparable to the thickness of field oxide isolation and the thickness of SOI buried oxides. Thus, significant dose enhancement effects can occur in most of the oxide structures of present day IC technologies.

The amount of dose enhancement will depend on the mechanism by which an incident photon interacts with a material. It will be largest for low-energy photons ($\ll 1\ \mathrm{MeV}$) which interact through the photoelectric effect [57]. For low-energy photons the number of secondary electrons generated is proportional to Z^4. Thus, as the atomic mass increases, the number of secondary electrons greatly increases. For an MOS transistor with a polysilicon gate, the atomic mass of silicon is slightly above the atomic mass of silicon dioxide and the amount of dose enhancement is negligible for $1.25\ \mathrm{MeV}$ ^{60}Co gamma rays (which interact through Compton scattering). On the other hand, for low-energy $10\ \mathrm{keV}$ x rays (which interact through the photoelectric effect) the amount of dose enhancement can be relatively large (~ 1.7) [58, 59], i.e., the dose in the oxide layer is 1.7 times the dose measured in charge particle equilibrium. Higher dose enhancement factors will result for metal silicide gates with higher atomic masses (e.g., Tungsten and Tantalum) [57, 60], if the distance of the metal layer from the oxide interface is within the range of the penetration depth of secondary electrons. For those materials in which significant dose enhancement can occur, the number of electron-hole pairs generated by the incident radiation must be multiplied by a dose-enhancement factor to determine the total number of electron-hole pairs generated.

6.1.3 Laboratory Radiation Sources

Wide ranges of laboratory radiation sources are available to characterize the response of electronic devices. For total-dose effects, these sources range from very high-dose-rate sources for investigating the basic mechanisms of radiation effects to very low-dose-rate sources for simulating the total-dose response of electronic devices in the natural space environment. The most commonly used laboratory sources are moderate-dose-rate ^{60}Co and x-ray sources. ^{60}Co sources emit gamma rays with a nominal energy of $1.25\ \mathrm{MeV}$. These sources can have dose rates up to 400 rad(Si)/s. The present U. S. military standard test guideline MIL-STD-883D, Method 1019.5 specifies that laboratory acceptance testing must be performed at dose rates from 50 to 300 rad(Si)/s. Thus, ^{60}Co sources can normally meet these requirements. Another common type of laboratory source is the $10\ \mathrm{keV}$ x-ray source. Laboratory x-ray sources are available that can achieve dose rates from below 300 rad(Si)/s to above 3600 rad(Si)/s. These sources can be used to irradiate both unlidded packaged devices or devices on a wafer. The high dose rate of x-ray sources and the capability for testing at the wafer level allows for rapid feedback on radiation hardness during device fabrication [61]. Method 1019.5 does not allow

x-ray testing for radiation qualification. Two high-dose-rate sources that can be used to investigate the total-dose response of electronic devices at short times after a pulse of radiation are electron linear accelerators (LINACs) and proton cyclotrons. Electron LINACs are pulse type sources with pulse widths ranging from less than $20\ \mathrm{ns}$ to more than $10\ \mu\mathrm{s}$ with energies from $10\ \mathrm{MeV}$ to more than $40\ \mathrm{MeV}$. Dose rates greater than 10^{11} rad(Si)/s can be obtained from electron LINACs. Proton cyclotrons are quasi-continuous sources and can have dose rates as high as 1 Mrad(Si)/s with energies from around $20\ \mathrm{MeV}$ to greater than $200\ \mathrm{MeV}$. They can also be operated in low current modes suitable for characterizing proton-induced single-event effects. For simulating low-dose-rate total-dose effects, ^{60}Co and ^{137}Cs sources are available. ^{137}Cs sources emit gamma rays with a nominal energy of $0.66\ \mathrm{MeV}$. Dose rates below 0.01 rad(Si)/s can be obtained from ^{137}Cs radiation sources.

6.2 Radiation effects on MEMS switches

To test the RF-MEMS switches sensitivity to radiation stress, several kinds of devices (series and shunt configuration, with and without dimples, straight beams and meander based, see par. 1.3) have been submitted to $2\ \mathrm{MeV}$ of protons (AN2000 accelerator at INFN, Legnaro, Italy) and $10\ \mathrm{keV}$ x-rays (INFN, Legnaro, Italy) radiation. The radiation effects on the devices have been studied comparing the DC characterization of the fresh switch with the stressed one. Moreover, already cycling stressed device have been submitted to radiation with the aim to monitor possible contact degradation.

6.2.1 Protons stress

An excerpt of the complete characterization carried out after increasing doses of 1, 10, and 30 $\mathrm{Mrad}\ (SiO_2)$ protons stresses, and during the subsequent room temperature anneal is reported in figure 6.4 (shunt switch), whereas the evolutions of S-parameters and actuation voltage values are shown in figure 6.5 and figure 6.6, respectively.

After the first session of radiations ($1\ \mathrm{MeV}$) the switch exhibits only a slight degradation in the isolation value that passes from $-27\ \mathrm{dB}$ to $-26\ \mathrm{dB}$ and no variations in the actuation and release voltage. After the third session and a total dose of $30\ \mathrm{MeV}$, the S-Parameter degradation in the actuated state is more consistent (almost $5\ \mathrm{dB}$ worst than the untreated device) but still acceptable. The device heavy degradation begins the day after the stress and continues for the next six months leading to a loss in the RF performances of almost $15\ \mathrm{dB}$. The main result is the heavy degradation of the insertion losses, with a small variation of the actuation voltage (V_{Act}).

In principle, the damage induced by $2\ \mathrm{MeV}$ protons could be due to either displacement damage (lattice defects directly induced by proton-nucleus interactions), or to ionizing damage (protons generate columns of charges in the device that recombine and/or move generating the actual damage) [50]. In this case, the main damage seems to be the displacement of nucleons, since the loss of RF performances only in the actuated state is a typical lead of contact resistance increase. The eventual alteration of the gold crystal that constitute the MEMS membrane due to displacement damage would explain such resistance increase. Moreover, the degradation is

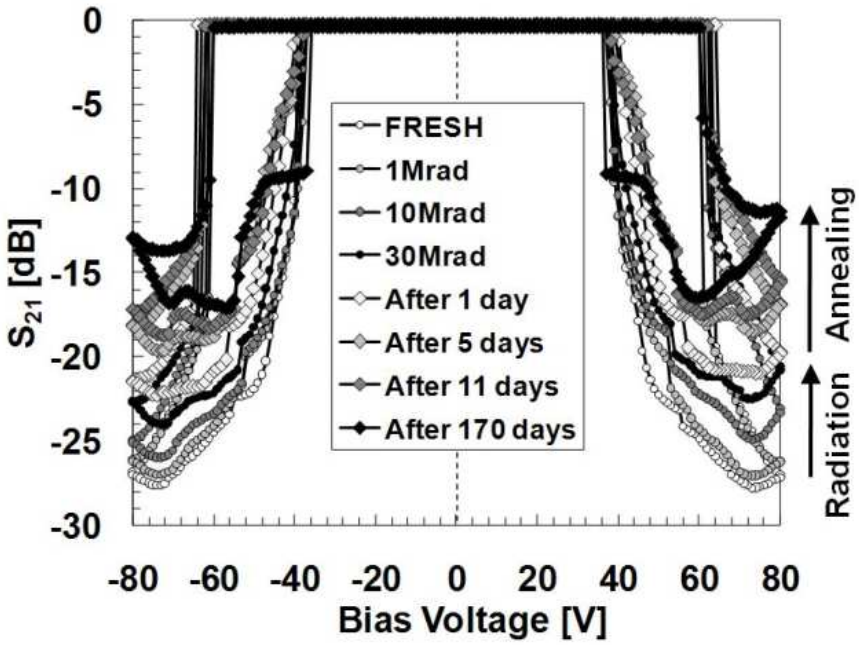

Fig. 6.4: Degradation of S_{21} (V_{Bias}) of a shunt switch (straight beams) during the protons radiation stress and the successive days of storage. f_{RF} = 6 GHz, P_{RF} = 0 dBm.

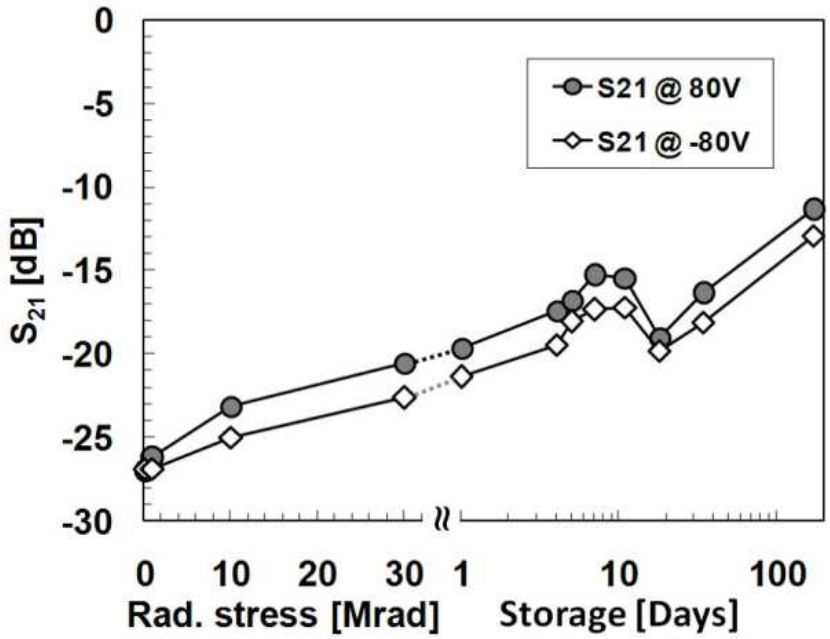

Fig. 6.5: Evolution of the S_{21} parameter at 80 V and −80 V extracted from curves of figure 6.4.

likely not due to an increase of the coplanar waveguides or substrate losses, because repeating the measurements applying RF signals from 10 kHz to 6 GHz leads to the same result (see figure 6.7). Furthermore, stressed devices have shown a faster degradation rate during cycling stresses if compared to the cycling stress of a fresh switch (see figure 6.8), and this lead us again to an altered metal-to-metal contact (increased series resistance).

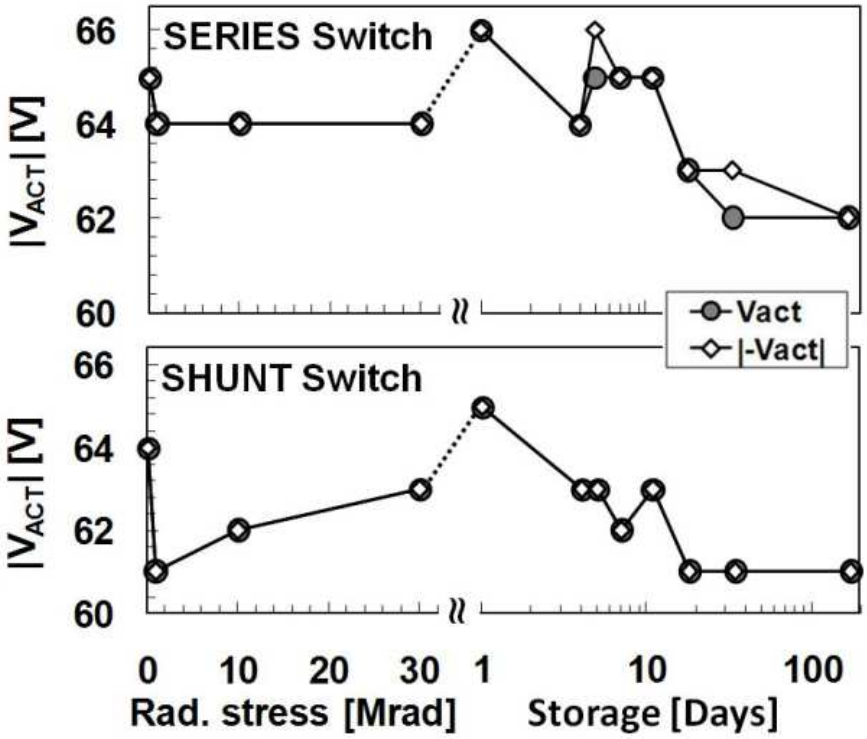

Fig. 6.6: Evolution of V_{Act} and $-V_{Act}$ for a series switch (up) and a shunt one (bottom, from figure 6.4) during the protons radiation stress and the successive days of storage.

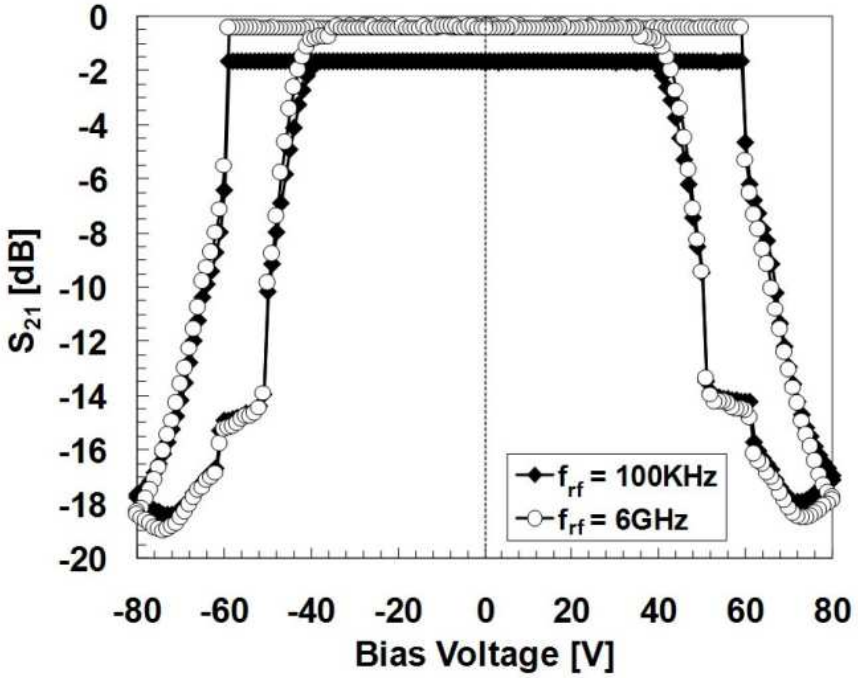

Fig. 6.7: Comparison of S_{21} (V_{Bias}) of a shunt switch measured applying an RF signal of 100 kHz*, and* 6 GHz*. P_{RF} =* 0 dB*. The curves are almost identical.*

6.2.2 Radiation damage simulation

To better understand the nature of the radiation damage, a simulation with the TRIM software has been performed. The parameters used are, except the radiation dose and kind of course, the

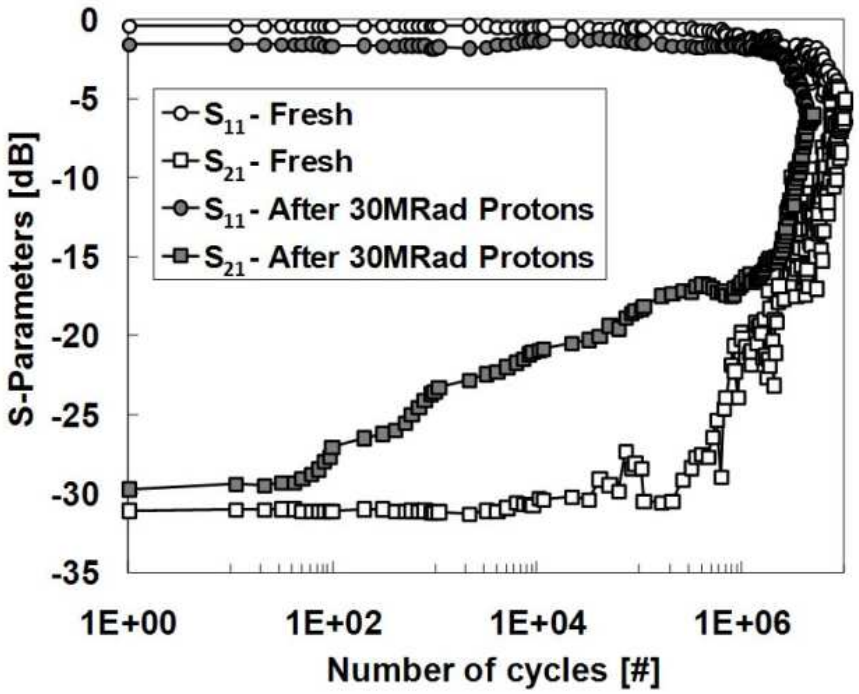

Fig. 6.8: Comparison of the cycling robustness of an untreated series switch with a $30\ \mathrm{Mrad}$ *protons stressed one.* V_{Bias} = $80\ \mathrm{V}$, f_{RF} = $6\ \mathrm{GHz}$, P_{RF} = $0\ \mathrm{dB}$

device different layers with the respective height (see figure 6.9 where a sketch of the MEMS process layers is reported).

Fig. 6.9: Schematic process description.

In figure 6.10 is reported the simulation output. We can summarize the main results as follow:

i) the range of $2\ \mathrm{MeV}$ protons is more than enough to cross all the device active area: this means that the switch MEMS part should not heavily suffer by radiation damage;

ii) the displacement damage is mainly located in the bulk of the silicon: a possible consequence of bulk damages could be RF performances losses in both actuated and unactuated state due to silicon crystalline properties alteration;

iii) however, displacement damage in the gold layer is much higher than in the surface silicon, due to the larger mass of the former: the MEMS structure would not be so rad-hard as expected and metal structure degradation could lead to unexpected increase of the resistance in the actuation state or to spring constant alteration due to localized variations in the bridge Young module.

The fluences used during the experiment (up to $1.7 * 10^{13}$ for the higher dose) are actually compatible with literature results on displacement damage in silicon devices [62].

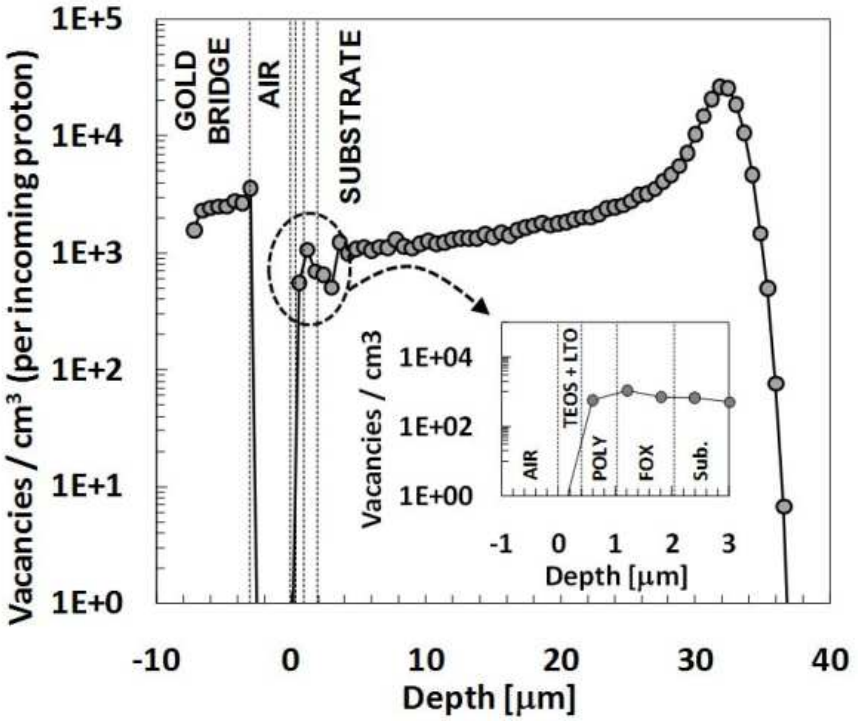

Fig. 6.10: TRIM Simulation of displacement damage for $2\ \mathrm{MeV}$ *protons in our devices. The inset highlights the vacancies/*cm^3 *just below the air-gap.*

6.2.3 X-ray stress

To shed a better light on what kind of damage is really impairing the device life-state, we moved to a radiation source where displacement damage is in first approximation negligible, such as $10\ \mathrm{keV}$ x-rays. 70 devices were tested with x-rays up to $1\ \mathrm{MeV}(SiO_2)$(see table 6.2).

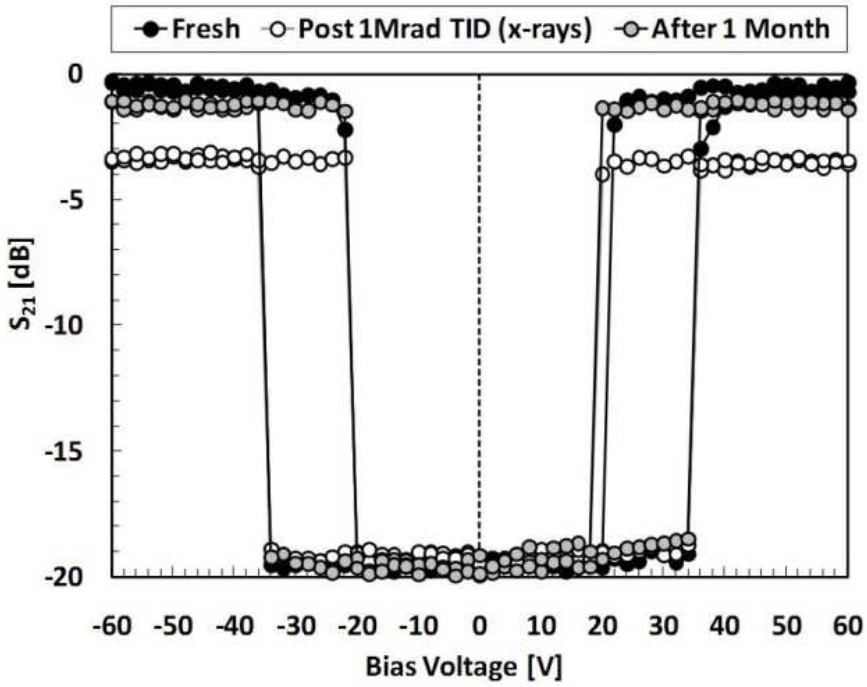

Fig. 6.11: Comparison of S_{21} (V_{Bias}) of a fresh shunt switch, after $1\ \mathrm{Mrad}$ x-rays stress, and after 1 month of storage (showing the recovery).

Meander Based Suspension		**Straight Beams Suspensions**	
Failure Mode	*Failure [%]*	*Failure Mode*	*Failure[%]*
Stiction	50	Stiction	6
S-Parameter Dagradation	42	S-Parameter Dagradation	24
Neglegible Variation	8	Neglegible Variation	66
Actuation Line Damage	0	Actuation Line Damage	4

Table 6.2: X-ray radiation stress induced failures. Number of tested devices: 30 meanders based, 40 straight beams.

Thirty of the stressed devices were meander based structures, a low k (spring constant) typology of switch. They have shown the heavier damages with an high rate of stiction condition after the stress (50%) or critical S-parameter degradation (42%). Only few devices (8%) have shown a behavior similar to the fresh state after the stress.

On the contrary, straight beams devices, characterized by a stronger spring constant, have reported less radiation damages with just few devices that have been found in stiction condition after the stress (6%) and a reasonable number that have shown a degradation in the S-parameter value (24%). The other stressed switches have shown no change in the DC characterization with the except of two devices that have had their actuation pad exploded during the post stress characterization probalbly for the isolator degradation that have generated a short circuit.

An interesting result is reported in figure 6.11 (series switch), in which the radiation stress has degraded the S-parameters (S_{21} in on state), with almost no changes in both V_{Act} and V_{Rel}, and showing a good recovery after 1 month. This more pronounced recovery found after x-rays irradiation, if compared to protons, suggests that displacement damage may actually play a role in the degradation of switches performance. On the other side, recombination kinetics is not

the same after irradiation with x-rays and protons (especially at relatively low energies such as those used here [50]), and phenomena purely linked to ionization damage cannot be excluded.

Conclusions

Reliability is a critical issue for MEMS to mature as a mainstream technology. As MEMS devices are employed in many configurations where voluminous components are still in use, it is imperative that the reliability and lifetime expectations are met or exceeded for the success of RF-MEMS in future RF applications. In order for RF-MEMS to be integrated with mainstream CMOS foundry technologies globally, they must achieve acceptable reliability objectives.

In this work the reliability of RF-MEMS switches has been deeply investigated obtaining important information on the optimized biasing conditions (actuation voltages and duty cycle), on the characterization procedures and cycling. Also the problem of long term actuation condition of work has been suggested. Furthermore, it has been underlined the necessity of adequate design rules in order to reach reasonable robustness of these devices against Electrical Overstress and Electrostatic Discharge events and a preliminary study on radiation effects has been carried out.

It has been also demonstrated that traditional electrical measurements and cycling stresses are not sufficient to fully characterize RF-MEMS switches. The suspensions shape (spring constant) impacts on the electrical parameters (pull-in, pull-out) of RF-MEMS switches has been investigated, and how the cycling reliability is influenced by the suspended membrane geometry and bias voltage.

The release phase of ohmic RF-MEMS switches submitted to long time of continuous polarization has also been characterized, founding that meander suspensions, characterized by lower spring constant than straight beams ones, can heavily impact on the release time, and then on the reliability of such devices. A complete analysis of unexpected bounces presence in the release phase has also been carried out, showing how the layout type and membrane thickness can impact on the transient behavior during the un-actuation of RF-MEMS switches submitted to a pulsed actuation.

The sensitivity to EOS/ESD phenomena of ohmic RF-MEMS switches have been deeply investigated, considering both not actuated, partially bended, and fully actuated membrane. In fact, completely different scenario appear considering the three topologies. Previous data and failure criteria investigation have been confirmed [34], whereas it has found that the RF-switch robustness could be strictly dependent by the suspension shape, by the type of contact between the suspended membrane and the transmission line (flat, with dimples or winglets), and also by the value of the actuation voltage. Preliminary HBM results have also been presented, and data show a good correlation of the range of breakdown voltage between TLP and HBM tests.

Electro-mechanical simulations have been carried out in order to investigate how the suspended membrane reacts to short events, finding that in the range of $100\ \mathrm{ns}$ long events a

negligible displacement is achieved, whereas in the range of μs events it is relatively easy to induce large displacement before the switch failure occurs. Moreover, it has been found that a new stiction mechanism can be induced by the dielectric breakdown occurring at the crossing between the suspensions and the actuator electrodes, exposing RF-MEMS switches to another problem related to their weakness to EOS/ESD events if not properly designed.

The sensitivity to radiation damage of several devices, with different layouts and configurations (shunt and series) has been evaluated finding that the main effect of the radiation has been the degradation of the S-parameters when actuated, with negligible changes in the actuation voltage. This degradation after 1 month can be recovered (x-ray stress), suggesting the presence of some charge entrapment or redistribution that masks the complete actuation of the structure, or can deteriorate, suggesting displacement damage due to protons-nucleons interaction. The very interesting result is that the TID induced degradation is very similar to the degradation caused by low voltage cycling, indicating that the radiation could be studied as a new accelerating factor for long term stresses.

From a design point of view, the straight beams devices have shown a better cycling stress and DC characterization and seems to be less prone to stiction phenomena during long term actuation stress. Also the radiation stress is less traumatic for straight beams switches suggesting that a strong spring constant is suitable to produce a reliable device.

To conclude, we can argue that the tested RF MEMS switches have shown several reliability issues, as expected from a quite novel technology, but they are still of great interest for the market application. Further tests, to fulfill the space application requirements, would also involve the temperature stress, as the climatic chamber storage, and temperature cycling, to reproduce the climatic behavior of a satellite (from -50° C to $+125^\circ$ C for storage periods). These kind of stresses would be of extreme importance for RF MEMS switch characterization because of the presence of metallic membrane that can be very sensible to buckling effects [63]. In fact, the deformation of the membrane, due to high temperature, could negatively affect the switch mechanical behavior, leading to, in the best case, an RF performances degradation or, in the worst case, to a no more working switch. Moreover, from a process point of view, high temperature would increase the diffusion of the Chrome, used to attach the Gold layer with the TiN alloy, into the Gold, leading to an increase of the Gold stiffness [64]. Of course the storage temperature are quite low compared to the ones used for a standard annealing (typically around 300° C), nevertheless its effect should be verified. Also the implications of a cold environment should be taken into account, since low temperatures tend to increase the stiffness of the metallic part with a consequential increase in the spring restoring force. Such an alteration would eventually evolve in an higher actuation voltage that could degenerate into a no more bendable membrane. From another point of view, the temperature increase would be welcome for the helping in the recombination process of the charges trapped into the MEMS dielectric with a consequential reduction in the screening and stiction phenomena [65].

Publications

During the doctoral studies, the following articles have been published:

i) A. Tazzoli, A. Gnudi, R. Gaddi, V. Peretti, E. Zanoni, G. Meneghesso, "Resistive RF-MEMS Switches Characterization and Reliability" HETECH 2005-14th International Workshop on Heterostructure Technology.

ii) A. Tazzoli, V. Peretti, R. Gaddi, A. Gnudi, E. Zanoni, G. Meneghesso, "Reliability issues in RF-MEMS switches submitted to cycling and ESD test", Proc. of IRPS 2006, 2006 IEEE International Reliability Physics Symposium - San Jose, California, March 26-30, 2006.

iii) V. Peretti, A. Tazzoli, E. Zanoni, G. Meneghesso, R. Gaddi, A. Gnudi, "Reliability issues of RF-MEMS switches",Electronic Group Meeting, 2006, Napoli, Italy. - Best Poster Award

iv) A. Tazzoli, V. Peretti, E. Zanoni, G. Meneghesso, "Transmission Line Pulse (TLP) Testing of Radio Frequency (RF) Micro-machined Micro-electromechanical Systems (MEMS) Switches", Proc. of 28th Electrical Overstress/Electrostatic Discharge Symposium Proc., EOS/ESD 2006, pp. 295-303, Westin La Paloma Tucson, Arizona, USA September 10-15, 2006. - BEST STUDENT PAPER Award

v) A. Tazzoli, V. Peretti, D. Bozzato, E. Zanoni, G. Meneghesso, "Characterization Issues and ESD Sensitivity of RF-MEMS Switches", Joint Workshop On MEMS Reliability, ESREF 2006, Wuppertal, Germany, Oct. 2, 2006.

vi) A. Tazzoli, V. Peretti, G. Meneghesso, "Long Term Actuation Issues of Ohmic RF-MEMS Switches", HeTech 2007, 16th European Workshop on Heterostructure Technology, Fréjus, September 2-5, 2007, Mo 1.4.

vii) A. Tazzoli, V. Peretti, G. Meneghesso, "Characterization Issues and Charge Trapping Effects on RF-MEMS switches", HeTech 2007, 16th European Workshop on Heterostructure Technology, Fréjus, September 2-5, 2007, Tu 2.5.

viii) A. Tazzoli, V. Peretti, G. Meneghesso, "Electrostatic Discharge and Cycling effects on Ohmic and capacitive RF-MEMS Switches", IEEE Transactions on Device and Materials Reliability, Vol. 7, No. 3, September 2007, pp. 429-437.

ix) A. Tazzoli, V. Peretti, G. Cellere, G. Meneghesso, "RF-MEMS Switches Reliability for Long Term Spatial Applications", 6th ESA Round Table on Micro and Nano Technologies for Space Applications,2007.

x) A. Tazzoli, V. Peretti, E. Autizi, G. Meneghesso, " Suspension Shape Impact on the Reliability of RF-MEMS Redundancy Switches", Proc. of IRPS 2008, 2008 IEEE International Reliability Physics Symposium.

xi) A. Tazzoli, E. Autizi, V. Peretti, G. Meneghesso,"Stiction Induced by Dielectric Breakdown on rf-MEMS Switches", Memswave 2008, poster session.

xii) A. Tazzoli, V. Peretti, E. Autizi, G. Meneghesso "EOS/ESD Sensitivity of Functional rf-MEMS",30th EOS/ESD Symposium, September 2008.

xiii) A. Tazzoli, G. Cellere, E. Autizi, V. Peretti, A. Paccagnella, G. Meneghesso, "Radiation Sensitivity of Ohmic RF-MEMS Switches for Spatial Applications", IEEE MEMS 2009.

Bibliography

[1] G. Rebeiz. RF MEMS in Full CMOS Radio SOC. *Proceedings of the 2005 MTT-S International Microwave Symposium*, pages 36–56,192–201, June 2005.

[2] R. Plana. What's Hot in RF Components and Systems. *Microwave Journal*, February 2006.

[3] G. Rebeiz. RF MEMS theory, design, and technology. *Wiley-Interscience*, pages 36–56,192–201, 2003.

[4] D. Peroulis, S. P. Pacheco, K. Sarabandi, and L. P. B. Katehi. Electromechanical considerations in developing low-voltage rf mems switches. *IEEE Transation on Microwave Theory and Techniques*, 51:258–270, 2003.

[5] F. Giacomozzi et al. Electromechanical Aspects in the Optimization of the Transmission Characteristics of Series Ohmic RF-Switches. *Proceedings of the 5th MEMSWAVE Workshop*, pages C25–C28, June 2004.

[6] R. Gaddi et. al. Interdigitated Low-loss Ohmic RF-MEMS Switches. *NSTI Nanotech 2004*, 2:327–330, March 2004.

[7] P. Blondy, A. Crunteanu, C. Champeaux, A. Catherinot, P. Tristant, O. Vendier, J. Cazaux, and L. Marchand. Dielectric Less Capacitive MEMS Switches. *IEEE MTT-S International Microwave Symposium Digest*, 2:573–576, June 2004.

[8] G. Colombo. Manuale dell'ingegnere. *Hoepli*, page 674, 1958.

[9] A. Ocera, P. Farinelli, P. Mezzanotte, and R.Sorrentino. A novel MEMS reconfigurable hairpin line filter on silicon substrate. *Proceedings of the 36th European Microwave Conference*, 2006.

[10] A. Ocera, P. Farinelli, F. Cherubini, P. Mezzanotte, R.Sorrentino, B. Margesin, and F. Giacomozzi. A MEMS Reconfigurable Power Divider on High Resistivity Silicon Substrate. *Proceedings of IEEE MTT-S Intl. Digest*, 2007.

[11] J. Maciel. Recent Reliability Results in RF MEMS. *Proceedings of the 2005 IEEE MTT-S Int. Microwave Symposium*, June 2005.

[12] J. L. Zunino III et al. Micro-electromechanical Systems (MEMS) Reliability Assessment Program for Department of Defense Activities. *Proceeding of the 2005 NSTI Nanotechnology Conference and Trade Show (Nanotech)*, 3:463–466, May 2005.

[13] J. De Natale and R. Mihailovic. RF MEMS Reliability. *The 12th International Conference on Solid State Sensors, Actuators and Microsystem*, June 2003.

[14] S. Melle et al. Reliability behaviour of RF MEMS. *Semiconductor Conference*, 1, October 2003.

[15] X. Yuan, S. Cherepko, J. Hwang J, C. L. Goldsmith, C. Nordqusit, and C. Dyck. Initial Observation and Analysis of Dielectric-Charging Effect on RF MEMS Capacitive Switches. *IEEE MTT-S International Microwave Symposium Digest*, 3:1943–1946, June 2004.

[16] S. Melle et al. Investigation of dielectric degradation of microwave capacitive microswitches. *17th IEEE International Conference on Micro Electro Mechanical Systems*, pages 141–144, January 2004.

[17] X. Rottenberg et al. Distributed dielectric charging and its impact on RF MEMS device. *34th European Microwave Conference*, 2004.

[18] B. Stark. MEMS Reliability Assurance Guidelines for Space Applications. *Jet Propulsion Laboratory*, 1999.

[19] B.Pillans et al. RF power handling of capacitive RF MEMS device. *Microwave Symposium Digest*, 1:329–332, December 2002.

[20] B. Ducarouge et al. Power capabilities of RF MEMS. *24th International Conference on Microelectronics (MIEL)*, pages 65–70, May 2004.

[21] B. D. Jensen, H. Kuangwei, L. Chow, K. Saitou, J. S. Volakis, and K. Kurabayashi. Asperity heating for repair of metal contact RF MEMS switches. *IEEE MTT-S International Microwave Symposium Digest*, 3:1939–1942, June 2004.

[22] B. D. Jensen, L. W. Chow, R. F. Webbink, K. Saitou, J. L. Volakis, and K. Kurabayashi. Force dependence of RF MEMS switch contact heating. *17th IEEE International Conference on Micro Electro Mechanical Systems*, pages 137–140, January 2004.

[23] G.B.Brook E.A.Brandes. Smithells Metals Reference Book. *Butterworth-Heinemann*, pages 1194–1198, 1992.

[24] D.Dubuc et al. Methodology to assess the reliability behaviour of RF-MEMS. *Gallium Arsenide applications symposium*, October 2004.

[25] C.Goldsmith. Lifetime characterization of capacitive RF-MEMS switches. *IEEE MTT-S Digest*, 2001.

[26] Y.Oya et al. A reliable and compact polymer-based package for capacitive RF-MEMS switches. *IEDM Technical Digest. IEEE International*, pages 31–34, December 2004.

[27] C. L. Goldsmith and D. I. Forehand. Temperature Variation of Actuation Voltage in Capacitive MEMS Switches. *IEEE Microwave and Wireless Components Letters*, 15, October 2005.

[28] B. Schauwecker, J. Mehner, K. Strohm, H. Haspeklo, and J.-F. Luy. Investigations of RF shunt airbridges among different environmental conditions. *Sens. Act. A*, 114:49–58, 2004.

[29] B.Pillans et al. RF MEMS reliability at Raytheon. *Proc. IEEE Int. Microwave Symp.Workshop WFF: Reliability Testing Reliability Enhancement RF MEMS Switches*, June 2004.

[30] C. Goldsmith et al. High-Cycle Life Testing of RF MEMS Switches. *IEEE/MTT-S*, pages 1805–1808, June 2007.

[31] Campbell et al. Orbital Debris Hazard Assessment Methodologies for Satellite Constellations. *Adv. Astron. Sci.*, 105:639–652, 2000.

[32] P. Dressendorfer, J. Mazur, J. Schwank, T. Waetherford, and C. Poivey. Radiation Effects - From Particles to Payloads. *Short course Notebook at 2002 IEEE NSREC*, July 2002.

[33] H. C. Koons, J. E. Mazur, R. S. Selesnick, J. B. Blake, J. F. Fennell, J. L. Roeder, and P. C. Anderson. The impact of the space environment on space systems. *Aerospace Technical Report TR-99(1670)-1*, 1999.

[34] A. Tazzoli, V. Peretti, E. Zanoni, and G. Meneghesso. Transmission Line Pulse (TLP) Testing of Radio Frequency (RF) Micro-machined Micro-electromechanical Systems (MEMS) Switches. *Proc. of 28th Electrical Overstress/Electrostatic Discharge Symposium*, pages 295–303, September 2006.

[35] A. Tazzoli, V. Peretti, R. Gaddi, A. Gnudi, E. Zanoni, and G. Meneghesso. Reliability issues in RF-MEMS switches submitted to cycling and ESD test. *Proc. of IRPS 2006, 2006 IEEE International Reliability Physics Symposium*, March 2006.

[36] W. M van Spengen et al. Experimental characterization of stiction due to charging in RF MEMS. *Proceedings of IEDM*, 114:901–904, December 2002.

[37] A. Tazzoli, V. Peretti, E. Autizi, and G. Meneghesso. Suspensions Shape Impact on the Reliability of RF-MEMS Redundancy Switches. *Proc. of IRPS 2008, 2008 IEEE International Reliability Physics Symposium*, 2008.

[38] B. D. Jensen et al. Effect of Nanoscale Heating on Electrical Transport in RF MEMS Switch Contacts. *Journal of Microelectromechanical Systems*, 14:935–947, October 2005.

[39] J. A. Walraven et al. Human Body Model, Machine Model, and Charged Device Model ESD Testing of Surface Micromachined Microelectromechanical Systems (MEMS). *Proceedings of the Electrical Overstress/ Electrostatic Discharge (EOS/ESD) Symposium*, pages 238–248, 2001.

[40] J. Ruan et al. Electrostatic discharge failure analysis of capacitive RF MEMS switches. *icroelectronics Reliability*, 47, 2007.

[41] W. D. Greason. Effect of Charge Injection due to ESD on the Operation of MEMS. *IEEE Trans.*, pages 2188–2193, 2007.

[42] A. Tazzoli et al. Electrostatic Discharge and Cycling Effects on Ohmic and Capacitive RF-MEMS Switches. *IEEE Trans. on Device and Materials Reliability*, 7:429–437, september 2007.

[43] A. Tazzoli, V. Peretti, R. Gaddi, A. Gnudi, E. Zanoni, and G. Meneghesso. Reliability Issues in RF-MEMS Switches Submitted to Cycling and ESD test. *Proceedings of the IEEE International Reliability Physics Symposium (IRPS)*, pages 410–415, 2006.

[44] A. Amerasekera and C. Duvvury. ESD in Silicon Integrated Circuits. *John Wiley and Sons*, pages 47–57, 2002.

[45] S. Voldman, B. Ronan, S. Ames, A. Van Laecke, J. Rascoe, L. Lanzerotti, and D. Sheridan. Test Methods, Test Techniques and Failure Criteria for Evaluation of ESD Degradation of Analog and Radio Frequency (RF) Technology. *Proceedings of the Electrical Overstress / Electrostatic Discharge (EOS/ESD) Symposium*, pages 92–100, 2002.

[46] S. Hyvonen, S. Joshi, and E. Rosenbaum. Combined TLP/RF Testing System for Detection of ESD Failures in RF Circuits. *Proceedings of the Electrical Overstress / Electrostatic Discharge (EOS/ESD) Symposium*, pages 346–353, 2003.

[47] A. R. Knudsen et al. The effects of radiation on MEMS accelerometers. *IEEE Trans. Nucl. Sci.*, 43, 1996.

[48] M. Exarchos et al. Charging of Radiation Induced Defects in RF MEMS Dielectric Films. *Proceedings of the 17th European Symposium of Electronic Device, Failure Physics and Analysis*, 46:1695–1699, 2006.

[49] S. S. McClure et al. Radiation Effects in Micro-Electro-Mechanical Systems (MEMS): RF Relays. *IEEE Trans. Nucl. Sci. 2002*, 49, October 2003.

[50] T.P.Ma and P.V. Dressendorfer. Ionizing radiation effects in MOS devices and circuits. *Wiley*, 1989.

[51] F. B. McLean and T. R. Oldham. Basic Mechanisms of Radiation Effects in Electronic Materials and Devices. *Harry Diamond Laboratories Technical Report*, HDL-TR-2129, September 1987.

[52] Evans. The Atomic Nucleus. *McGraw-Hill*, 1955.

[53] J. R. Srour. Basic Mechanisms of Radiation Effects on Electronic Materials, Devices, and Integrated Circuits. *Defense Nuclear Agency technical report*, DNA-TR-82-20, August 1982.

[54] J. Srour. Basic Mechanisms of Radiation Effects on Electronic Materials, Devices, and Integrated Circuits. *IEEE Nuclear and Space Radiation Effects Conference Short Course*, July 1983.

[55] S. M. Sze. Physics of Semiconductor Devices. *Wiley*, 1981.

[56] K. G. Kerris. Ionizing Radiation Effects in MOS Devices and Circuits. *John Wiley*, 1989.

[57] D. M. Fleetwood, P. S. Winokur, R. W. Beegle, P. V. Dressendorfer, and B. L. Draper. Accounting for Dose-Enhancement Effects with CMOS Transistors. *IEEE Trans. Nucl. Sci.*, 32:4369–4375, 1985.

[58] T. R. Oldham and J. M. McGarrity. Comparison of ^{60}Co Response in MOS Capacitors. *IEEE Trans. Nucl. Sci.*, 30:4377–4381, December 1983.

[59] C. M. Dozier and D. B. Brown. The use of Low Energy X-Rays for Device Testing . A Comparison with Co-60 Radiation. *IEEE Trans. Nucl. Sci.*, 30, December 1983.

[60] J. M. Benedetto, Jr. H. E. Boesch, and T. R. Oldham. Dielectric Less Capacitive MEMS Switches. *IEEE Trans. Nucl. Sci.*, 34:1540–1543, December 1987.

[61] M. R. Shaneyfelt, K. L. Hughes, J. R. Schwank, F. W. Sexton, D. M. Fleetwood, and P. S. Winokur. Wafer-Level Radiation Testing for Hardness Assurance. *IEEE Trans. Nucl. Sci.*, 38:1598–1605, 1991.

[62] S. Messenger et al. Non-ionizing energy loss (NIEL) for heavy ions. *IEEE Trans. on Nucl. Sci.*, pages 1595–1602, 1999.

[63] Y. Zhu and H.D. Espinosa. Effect of temperature on capacitive RF MEMS switch performance,a coupled-field analysis. *J. Micromech. Microeng. 14*, pages 1270–1279, 2004.

[64] P. Farinelli et al. RF-MEMS SPDT Switch on Silicon Substrate for Space Applications. *Topical Meeting on Silicon Monolithic Integrated Circuits in RF Systems*, pages 151–154, 2004.

[65] F.B. McLean, H.E. Boesch Jr., and T.R. Oldham. Electron-Hole Generation, Transport, and Trapping in SiO2. *Ionizing Radiation Effects in MOS devices and Circuits, J. Wiley and Sons*, 1989.